Investigation and Application of Voussoir Beam Theory for the Stability Evaluation of Underground Excavations

by

Chaoshi Hu

A thesis submitted in partial fulfillment of the requirements for the degree of

Doctor of Philosophy

Mining Engineering

Department of Civil and Environmental Engineering
University of Alberta

Abstract

Voussoir beam theory, also named as arching action, has been widely accepted and applied in design and construction of both surface and underground structures. This investigation focused on its underground applications with moderately jointed rock, such as underground mining and tunneling.

There are discrepancies between the voussoir beam models built by different researchers, for example, the shape and depth of the induced stress at abutment and midspan and the beam shortening equation. In this investigation, the behavior of voussoir beam under transverse loading was investigated through physical, numerical and theoretical modeling. It was found that the stress distributions at the midspan and abutment are different both in shape and depth through the photogrammetric analysis in physical investigation. And the stress distribution is changing as the loading changes. Using the physical tests as calibration and validation, the finite element code, *Phase*^{2} *8.0*, was selected to further the investigation. Systematically numerical modeling was performed to cover the voussoir beams with common ratios of span/thickness encountered in the field. The characteristics of voussoir beam behavior were obtained.

An analytical model was built based on a general form of stress distribution at the abutment and midspan with different depths of stress distribution. Based on the findings from physical and numerical investigations, an iteration procedure was proposed to determine the stability and deflection of voussoir beams under transverse loading.

The voussoir beam model developed was applied to analyze the mechanical behavior of stress riser of segmental precast concrete liner. The stress distribution at the stress riser of segmental

liner cannot be derived from existing closed form solution. There is always the uncertainty about the compressive failure of the segment liner especially when hair cracks happened at stress risers. Through modelling one piece of segment liner as a voussoir beam, the stress distribution and deflection at stress riser were obtained. It shows the stress riser is free from compressive failure for the target project. This is verified in the field by safely removing the temporary “reinforcing” measures. Voussoir beam theory is a suitable analytical method for the design of segmental tunnel liners.

Acknowledgements

I would like to express my gratitude to my supervisors, Dr. Derek Apel, Dr. Les Jozef Sudak and Dr. Jozef Szymanski. Without the support and continuous encouragement from my three supervisors, I cannot complete this research! I would like to specifically mention Dr. Szymanski, who passed away last year. I'm so grateful to have you as my supervisor.

Thanks to the committee members of my candidacy and final defense for your precious time.

I also like to thank Dr. Wei Victor Liu for your continually support. It is so grateful to have a good buddy like you.

Thank you to the graduate students in the Department of Civil and Environmental Engineering, University of Alberta.

I would like to express the deep gratitude to China Scholarship Council for the financial support.

Finally, I wish to thank my wife, Jiayu Chen, for your great support. Your joyfulness and optimism positively impact me especially when I was struggling on this research. I like to thank my parents, parents-in-law, my son Ray, for the joy you bring in every day.

Table of Contents

List of Tables

List of Figures

List of Symbols

A_A – area of the stress block at the abutment

A_M – area of the stress block at the midspan

e_A – eccentricity of the lateral thrust at the abutment

e_M – eccentricity of the lateral thrust at the Midspan

E_{abut} – modulus of elasticity of the abutment

E_{beamt} – modulus of elasticity of the rock beam

$\underline{e_r}$ – basis vector in the radial direction

$\underline{e_\theta}$ – basis vector in the tangential direction

$F_r,\ F_\theta$ – body force

k_1 – constant for the stress block equation at the abutment

k_2 – constant for the stress block equation at the midspan

L – approximate arch length

L_{exact} – exact arch length

ΔL_{arch} – incremental shortening of the arch

ΔL_{abut} – deformation of the abutment

n – ratio of the depth of stress induced at the abutment to beam thickness

N – ratio of the depth of stress induced at the midspan to beam thickness (i.e. $N = \lambda n$)

$R.E.$ – relative error

(r, θ) – polar coordinates

s – span of the Voussoir Beam

t – thickness of the Voussoir Beam, thickness of tunnel liner

T_A – lateral thrust generated at the abutment

T_M – lateral thrust generated at the midspan

T – total thrust

u_r – displacement in the radial direction

u_θ – displacement in the tangential direction

W – weight of the rock beam

(x, y) – rectangular coordinates

x_A – distance from the point of zero stress to the resulting line of action of the lateral thrust at the abutment

$\overline{x_A}$ – centroidal distance of the stress block at the abutment

x_M – distance from the point of zero stress to the resulting line of action of the lateral thrust at the midspan

$\overline{x_M}$ – centroidal distance of the stress block at the midspan

y^* – horizontal distance to where the internal uniformly distributed load is acting

z– distance between the line of action of the thrust at the abutment and that at the midspan (i.e. moment arm)

β –constant for the stress block equation

ε_r, ε_θ – radial and tangential strains in polar coordinates

$\varepsilon_{r\theta}$ – shear strain in polar coordinates

γ– unit weight of the rock

φ– Airy Stress Function

υ – Poisson's Ratio

ϑ_s– Poisson's ratio of soil around tunnel liner

ϑ_l– Poisson's ratio of tunnel liner

σ_1 – major principal stress

σ_3 – minor principal stress

σ_A – maximum compressive stress generated at the abutment

σ_c – uniaxial compressive stress of the intact rock

σ_M – maximum compressive stress generated at the midspan

σ_u – internal uniformly distributed stress acting across the whole depth of the beam

σ_r, σ_θ – radial and tangential normal stresses in polar coordinates

$\sigma_{r\theta}$ – shear stress in polar coordinates

$\sigma_{r\theta}$ – average stress acting along the entire arch line

ω– ratio of the abutment to midspan stresses

φ' – effective friction angle

k_o – coefficient of earth pressure at rest

D – outside diameter of tunnel

R – Radius of tunnel

H_o – Depth of ground at tunnel spring line

P_v – vertical ground pressure

P_h – horizontal ground pressure

F – flexibility ratio

C – compressibility ratio

σ_r – radial soil pressure on tunnel liner

u_r – radial displacement of tunnel liner

v_θ – tangential displacement of tunnel liner

P_θ – axial force in tunnel liner

V_θ– shear force in tunnel liner

M_θ– moment in tunnel liner

1 Introduction

It is not uncommon for a stratified rock mass to host an ore deposit. An ore body in a sedimentary setting frequently conforms to the surrounding rock, which has been stratified by bedding planes or other related depositional features. Excavations in stratified rock are therefore usually performed according to a cross-sectional geometry so that the roof and floor coincide with the bedding planes. This stratification structure can be the dominant factor controlling the roof stability in large civil excavations and in underground mining stopes (Betournay, 1987; Miller & Choquet, 1988).

Historically, the mechanical behaviors of stratified strata encountered in underground openings have been simplified as simple beam, cantilever, or slab. Design rules have likewise been developed on the basis of concepts from solid mechanics, such as elastic beam theories and plate theories. Elastic beam theories assume that the rock above the excavation acts as a beam or series of beams containing no cracks and loaded by self-weight. Thus the roof span is designed so that the allowable stress is not exceeded in these beams. In the field, those simplifications were found to be unable to explain the strength measured or calculated in stable underground openings. The analyses are over-simplified. Furthermore, the stable roof observed is too broken and cracked transversely to act as a simple beam. As a result, the voussoir beam theory was developed and adopted for the structural analysis of stratified strata. Stratified and jointed rock as these appear in the field is shown is Figure 1-1.

Figure 1-1 Stratified and jointed rock in the field (Y. H. Hatzor, 2012)

1.1 Concepts of the Voussoir Beam

The roofs of mine excavations in fractured rock stand up over span lengths well in excess of what might be expected from the analysis of a continuous beam. The strength of such undermined strata is derived from "arching action." The term "arching action" does not solely imply the formation of an arch- or dome-shaped opening. The term also refers to the process by which failed rocks may become self-supporting by the formation of a compression zone above an opening, which transfers vertical load to the adjacent abutments. This process is analogous to the voussoir arch commonly used in civil engineering projects.

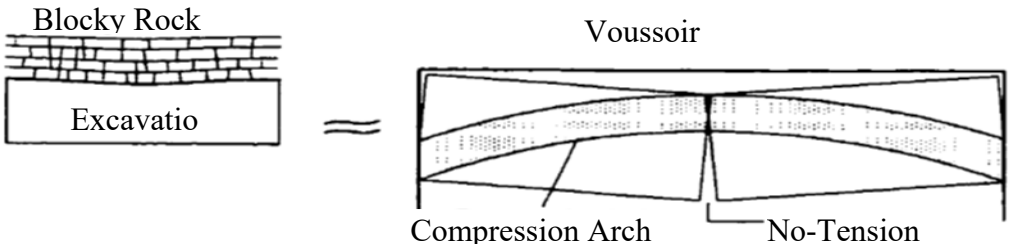

Figure 1-2 Voussoir beam analogy (M. S. Diederichs, 2000)

Figure 1-2 shows an underground excavation in stratified rock that is moderately jointed. As the beam deflects, these cracks open up, inducing lateral and frictional forces at the contact areas

between the blocks and abutments. The areas that are in contact with adjacent edges are under increasing compressive strain and hence high compressive stress occurs in these zones.

Voussoir beam theory recognizes that in a confined situation the ultimate strength of a beam is greater than its elastic strength and that pre-existing fractures impede the beam from sustaining tensile stresses. The stability of the fractured rock beam is maintained entirely by compression and shear resistance; hence the strength of the linear arch does not depend on the flexural strength of the rock.

1.2 Application of Voussoir Beam Theory

Some applications of voussoir beam theory are as follows:

a) Voussoir beam theory can be used to design stable roofs in excavations in moderately jointed strata.

b) Voussoir beam theory can be used to determine the strength of the segmental concrete liner that is widely used in mechanized tunneling, i.e. tunneling by Tunnel Boring Machine (TBM).

c) The general theory for voussoir beams can be extended to bedded footwall slopes. Currently, the potential modes of failure in bedded footwall slopes of Canadian western coal mines include linear slab failure and Euler buckling failure. However, Euler buckling is very sensitive to the buckling length and thickness of the buckling slab, making it necessary to design to very high safety factors (e.g., S.F. of 5 or 6). A more realistic buckling analysis can therefore be developed by considering the buckling strata as a voussoir beam.

d) For extracting pillar coal in old shallow mines with stratified roofs, voussoir beam theory can be used to determine the cutting sequence of pillars and the size of remnants (van der Merwe, 2009).

e) Using knowledge of voussoir beam strength and failure mechanism, monitoring data from real excavations can be analyzed with respect to the ongoing failure mechanisms in the roof, and conclusions can be drawn concerning imminent failure or stabilization.

1.3 Current Knowledge of Voussoir Beam Theory

Voussoir beam theory is generally attributed to Evans who first performed systematic research on the mechanical behavior of voussoir beams (Evans, 1941). Extensive investigation has since been performed using different methods. The following review of the voussoir beam theory literature is organized according to the three research approaches employed: analytical investigation, experimental investigation, and numerical investigation.

1.3.1 Analytical Investigations

In classical beam analysis (Euler beam or Timoshenko beam), a closed-form solution can be obtained for the shear and axial stress distribution, as well as for the amount of deflection. It is assumed that the beam is fixed at the ends and is therefore statically determinate. However, the voussoir beam is statically indeterminate as the beam is free to displace at abutments or at the midspan. The analytical solution can be arrived at either using the iteration method or by reducing unknown parameters by deriving new formulas from experiment results.

1.3.1.1 Iteration method

Evans (Evans, 1941) built the voussoir beam model to analyze underground roof stability, as shown in Figure 1-3 (note that only half of the model is presented due to its symmetry). An undermined beam with span (s) and thickness (t) is subjected only to the load of its own weight (w). The vertical load was transferred as the horizontal thrust (T) to the abutment through the arch in the beam. Evans proposed that both the stress distributions at the abutments and midspan have the same triangular shape (or linear distribution) and the same depth (nt) over the abutment and midspan, respectively.

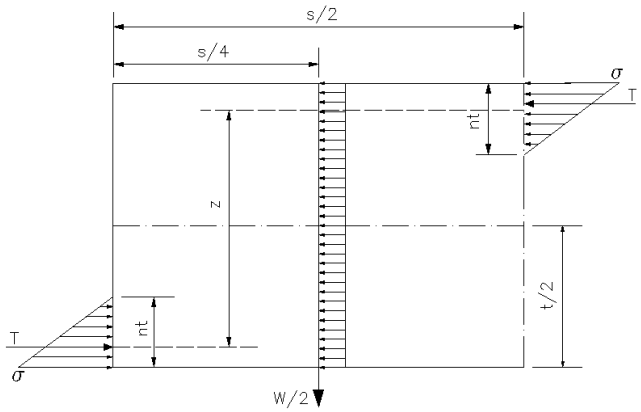

n – ratio of the depth of stress distribution to beam thickness; W – weight of the beam

σ – maximum stress at the abutments and midspan;

T – lateral thrust generated at the abutments and midspan

z – distance between the action line of the thrust at the abutment and that at the midspan (i.e., moment arm)

Figure 1-3 Voussoir Model proposed by Evans (Evans, 1941)

Because Evans made an error in the analysis of the total resistance moment, the analysis as a whole is incorrect as well. Nevertheless, the triangular shape of stress distribution that he proposed has been accepted until now. He also proposed that 0.5 is the proper value for *n*.

In order to calculate the elastic shortening of the arch under compression, Evans assumed a section of the beam over which equal stress was distributed. The position of the section is in the middle of the half-beam (i.e., s/4 from the abutment), as shown in Figure 1-3. Although the analysis contains a statics error, the approach is inspiring for the determination of arch shortening. The design procedure proposed by Evans was later modified by Beer and Meek (Beer & Meek, 1982). Subsequently, Sofianos (Sofianos, 1996) and then Diederichs and Kaiser (M. Diederichs & Kaiser, 1999b) noted some limitations in a simplified version of Beer and Meek's method and proposed alternative ways of addressing the static indeterminacy of roof-bed analysis. To be concise, only the revisions proposed by Diederichs and Kaiser and Sofianos, respectively, are described in this review.

Diederichs and Kaiser (M. Diederichs & Kaiser, 1999b) proposed an algorithm to test the stability of a voussoir beam against snap-through and crushing (see Figure 1-4) based on the assumption that there will be the same linear stress at the abutment and midspan. This procedure is accepted by Brady and Brown (Brady & Brown, 2004), which proposed that the distribution of horizontal stress at the center of the arch is parabolic and presented a new formula to determine the deflection of the arch.

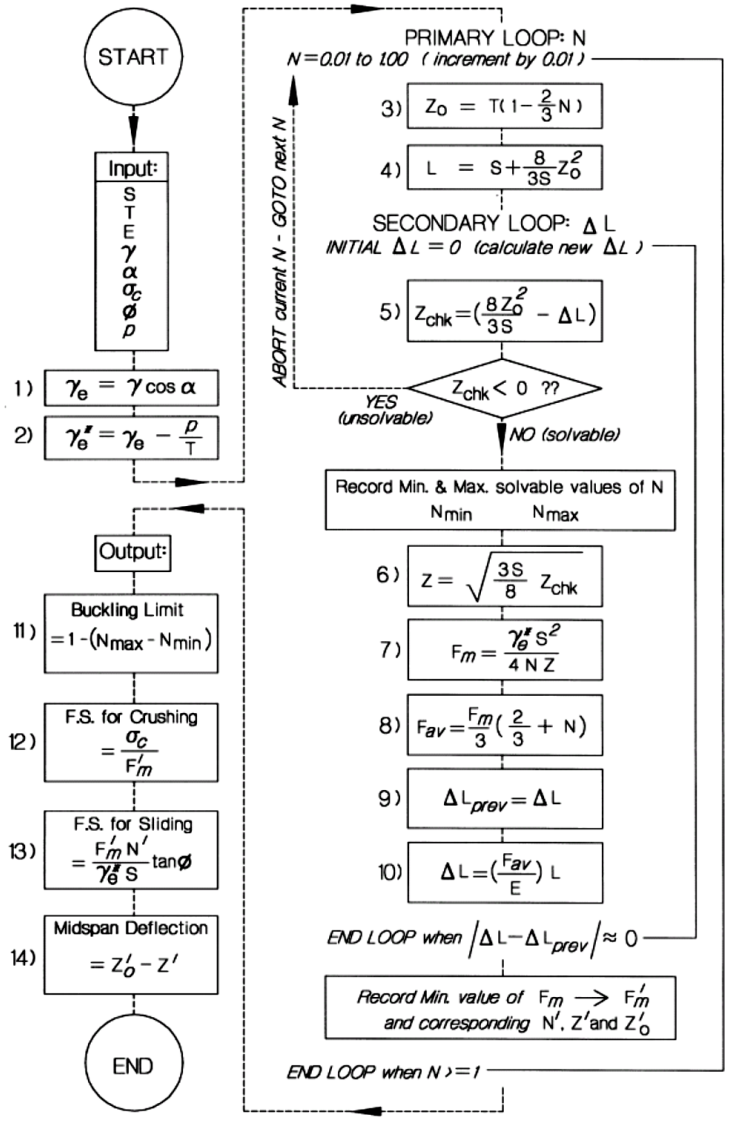

Figure 1-4 Flowchart for the determination of stability and deflection of a voussoir beam (M. Diederichs & Kaiser, 1999b)

1.3.1.2 Reducing unknown parameters method

Based on Evans's model, Sofianos (Sofianos, 1996) reduced the unknown parameters of static indeterminacy in the voussoir model by deriving formulas of the parameters from the numerical analysis results obtained by Wright (see Table 1-2). The formulas of the parameters (n_{av}, r and λ) are derived (see the non-rectangular box in Figure 1-5). The stress at the abutment is the same as at the midspan in Evans's model; however, it was found that they are different from each other according to Wright's results. Instead, Sofianos treated the stress at the abutment and midspan with the same thickness, $n_{av}t$, which is the arithmetic mean of the stress depth at the abutment (nt) and at the midspan (Nt). In order to calculate the shortening of the arch under elastic compression, Sofianos assumed that an equivalent thickness of the arch is χt and that the equivalent compression stress acting in the arch is σ_m. Ultimately, the formulas of extreme strain (ε_x) and deflection (δ) were derived in terms of the geometry, loading, and mechanical parameters of the beam, as shown in Figure 1-5. The relations for buckling, crushing, and the slip at the abutment are established (see Figure 1-5).

It should be noted that the analytical procedures of Sofianos and Diederichs and Kaiser assume different conceptual voussoir roof models. As a result, the analyses of static stability and beam deflection differ considerably between them. A discussion on the differences between the two models is provided by Sofianos (Sofianos, 1999) and Diederichs and Kaiser (M. Diederichs & Kaiser, 1999a).

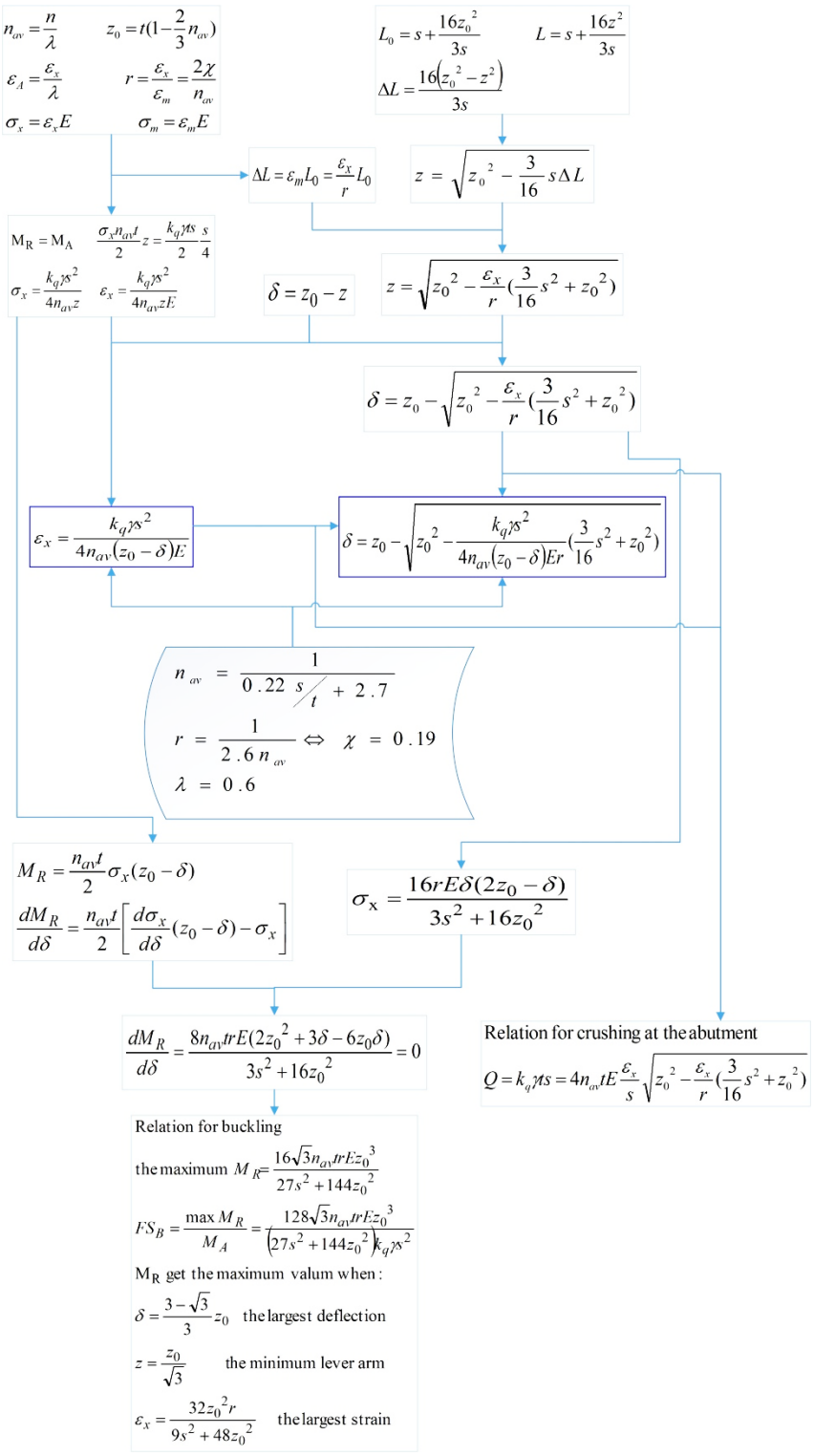

n_{av} is the intermediate value of the ratios of the depth of stress induced at the abutment and at the midspan to beam thickness; λ is the ratio of n to n_{av}; r is the ratio of the extreme strain (ε_x) to the equivalent strain (ε_m); χ is ratio of the depth of equivalent stress (σ_m) to the thickness of the beam (t); z_0 is the lever arm of voussoir beam with zero deflection; FS_B is the factor of safety for buckling.

Figure 1-5 Flowchart of Sofianos's analytical procedure (Sofianos, 1996)

Sofianos (Sofianos & Kapenis, 1998) validate the above-mentioned formulas with a distinct element code: UDEC. The numerical model consists of three blocks. The center block is the only deformable one that simulates half of the voussoir beam, the left rigid block simulates the abutment, and the right rigid block imposes the boundary conditions at the midspan. The contacts between the half-voussoir beam and the two rigid blocks are treated as discontinuities. In the left discontinuity, which represents the abutment of the beam, only lateral separation is permitted. In the right discontinuity, which represents the midspan of the beam, both vertical slip and lateral separation are permitted.

Sofianos found that the stress depth ratio (n_{av}) decreased not only with the span/depth ratio (s/t), according to the formula in Figure 1-5, but also with the normalized loading (described by $\frac{k_q \gamma s}{E}$). The formula developed is shown in Equation 1-1. The formula for the ratio (λ) of the depth of equivalent triangular stress at the abutment (*nt*) to that of the beam ($n_{av}t$) is refined as shown in Equation 1-2. As was the case with Wright's results (Wright, 1974), Sofianos noticed that the strain distribution at the abutments and midspan was not linear and that the maximum strain at the abutments is greater than it is at the midspan. The stress distribution at the abutment is shown in Figure 1-6. Stress at the abutment is affected by the variance of thickness (*t*) being in a higher order than the variance of Young's modulus. A formula for the maximum strain at the abutment is presented based on the nonlinear stress distribution (see Equation 1-3).

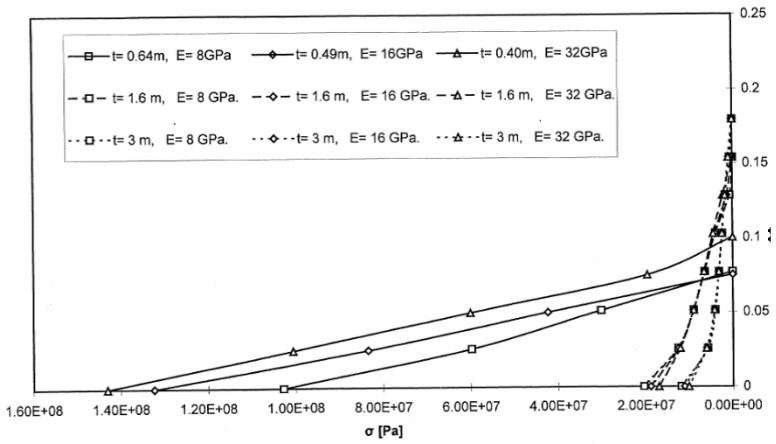

t is the beam thickness and E is the Young's modulus of the beam

Figure 1-6 Stress distribution at the abutment of a voussoir beam with a 20m span (Sofianos & Kapenis, 1998)

$$n_{av} = \begin{cases} 0.11 & for\ buckling \\ 0.3 - 0.14\frac{s}{t}\sqrt[3]{\frac{k_q \gamma s}{E}} & for\ crushing \end{cases} \quad \text{Equation 1-1}$$

$$\lambda = 0.6 + 0.004\frac{s}{t} \quad \text{Equation 1-2}$$

$$\ln \varepsilon_A = -3.8 + 1.5 \ln \frac{s}{t} - 0.06 \left(\ln \frac{k_q \gamma s}{E}\right)^2 \quad \text{Equation 1-3}$$

A third method, besides the two methods discussed above, was developed through Bakun-Mazor's (Bakun-Mazor, Hatzor, & Dershowitz, 2009) analysis of the voussoir beam under a non-linear stress distribution (see Figure 1-7). He proposed a method to determine the shape and depth of the stress distribution at the abutment and midspan by finding the minimum of maximum stress. That is, the maximum stress (σ_A and σ_M) will get the minimum value for the given shape and depth of stress distribution. The use of this method has been discontinued in order to analyze the failure mechanism of voussoir beams.

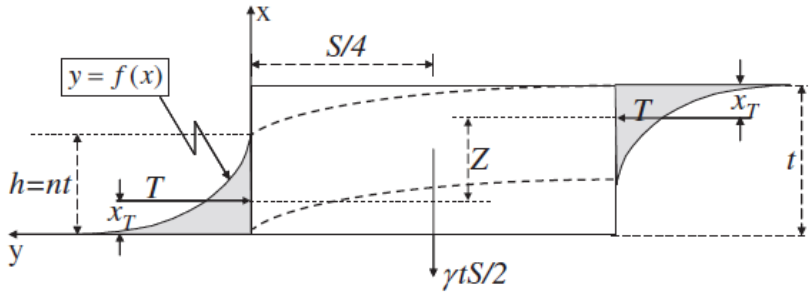

Figure 1-7 Bakun's model (Bakun-Mazor & Dershowitz 2009)

1.3.2 Experimental Investigations

Evans (Evans, 1941) built a steel frame to test the mechanical behavior of the voussoir beam (Figure 1-8). The steel frame consisted of two rods (ø7.62cm, 655.32cm long) with screwed ends, and two endplates built of U-shaped steel channels. A constraining force was applied through a knife-edge push-rod by tightening the nuts, which concentrated the force. The constraining force was measured by a bell crank installed at one end. The beam was formed by putting common building bricks end-to-end or face-to-face at an inclined angle. The experiments justified the aspect of voussoir beam theory that the undermined strata derive their capacity for self-support from voussoir beam action, not from simple bending.

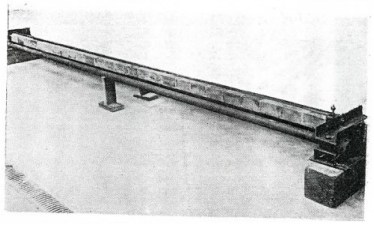

Figure 1-8 The Experimental Apparatus built by Evans (Evans, 1941)

Because Evans did not investigate the voussoir beams in the form of two blocks, which was the form analyzed in theoretical model, the experiments cannot be taken as a verification of or comparison to the theoretical analysis. Likewise, since the horizontal thrust was applied by a

knife-edge rod, the location of the thrust was predetermined, but not the response of the voussoir beam to the transverse loading. Finally, the full failure process for the beams was also not investigated as no loading system was used.

Wright (Wright, 1974) performed physical experiments to verify the formulas that he derived from numerical analysis results. The beam models consisted of limestone blocks or brick blocks similar to Evans's experiments. The testing frame is shown in Figure 1-9. The abutments are 2 limestone blocks 10-cm thick (*J* in Figure 1-9). The cracks at the abutments always opened first and farther than the crack at the midspan, and the beam behaved as if it had cracks at the abutments and at the center only. The testing results fit well with computer models. All the experiments are summarized in Table 1-1.

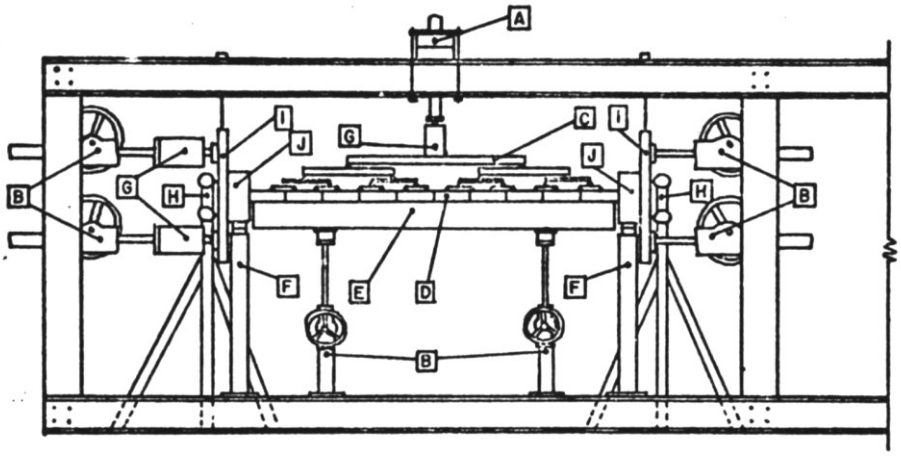

A hydraulic jack; B worm gear jack; C typical distributed load; D model; E retractable support;
F fixed abutment supports; G load cells; H separately supported dial gauges;
I thrust plates; J limestone abutment blocks

Figure 1-9 The Testing Apparatus built by Wright (Wright, 1974)

In Wright's experimental investigation, the stress distributions at the midspan and abutments are unable to be checked. There are several differences between the numerical model and physical model. The numerical models have rigid abutments, but the physical models have limestone abutments. Computer models were self-loaded, but the physical models were loaded from above.

The computer models have only three cracks at the abutments and midspan; physical models consisted of many blocks and have more than three cracks.

Table 1-1 Summary of Wright's experiments (Wright, 1974)

NO.	Material	Span m	Depth m	Span/ Depth	E Gpa	Constraining force kN/m	Failure information
1	limestone	0.9557	0.1524	6.271	36.17	0	Sliding at abutments
2	limestone	0.9557	0.1524	6.271	36.17	41.89	No information for failure type; *T* verses *Q* fit well with the formula curve.
3	limestone	1.8471	0.1524	12.12	36.17	0	
4	limestone	1.8471	0.1524	12.12	36.17	38.38	
5	limestone	3.7582	0.1524	24.66	36.17	0	
6	limestone	3.7582	0.1524	24.66	36.17	37.57	
7	brick	1.9397	0.05715	33.94	5.515	0	Failed by buckling; *T* - *Q* and δ – *Q* curves fit well with the formula; Buckling danger point is at $\delta/t=0.14$; The maximum load is at $\delta/t=0.3$.
8	brick	1.9162	0.05715	33.53	5.515	20.48	
9	brick	1.9397	0.05715	33.94	5.515	29.47	
10	brick	0.9729	0.05715	17.02	5.515	0	Crushing at the abutments; *T* - *Q* and δ – *Q* curves fit well with the formula; The compressive strength calculated by the formula from the maximum load tested fit the compressive strength tested.
11	brick	0.9729	0.05715	17.02	5.515	26.55	
12	brick	0.9729	0.05715	17.02	5.515	37.33	
13	limestone	0.9144	0.0254	36	36.17	unknown	Buckling at δ/t=0.21; *T* - *Q* and δ – *Q* curves fit well with the formula;
14	limestone	0.4572	0.0254	18	36.17	unknown	Crushing both at midspan and abutment; *T* - *Q* and δ – *Q* curves fit well with the formula; Calculated maximum stress is 80% larger than the tested strength
15	limestone	0.8954	0.0508	17.63	36.17	unknown	Crushing both at the top midspan and abutment; *T* verses *Q* fits well with the formula curve; Calculated maximum stress is 80% larger than the tested strength Calculated deflection is higher than the experimental value

Sterling (Sterling, 1977) designed a constraining beam testing apparatus (Figure 1-10), which consists mainly of two steel-end plates and four threaded rods. A servo-controlled load

application was enabled to test the full failure process of the beam. Three types of loading conditions were used during the tests: one-point, two-point, and four-point loading. The horizontal thrust was measured by strain gauges attached on the horizontal rods; the beam deflection was acquired or converted from the LVDT (Linear Variable Differential Transformer) reading, which shows the convergence of the testing machine platens. The experimental parameters investigated included the material properties of beam, beam size, initial end conditions, loading conditions, support conditions and stiffness of lateral support, creep or relaxation, and multiple layers. The relations between load/deflection, lateral thrust/vertical load, eccentricity/vertical load, and crack diagram were presented. Nevertheless, the beam samples tested were intact beams, not voussoir beams. The stress distribution at the end was also not investigated. Finally, the eccentricity of the lateral thrust, which was determined by resolution of the upper and lower bar loads, are not reliable.

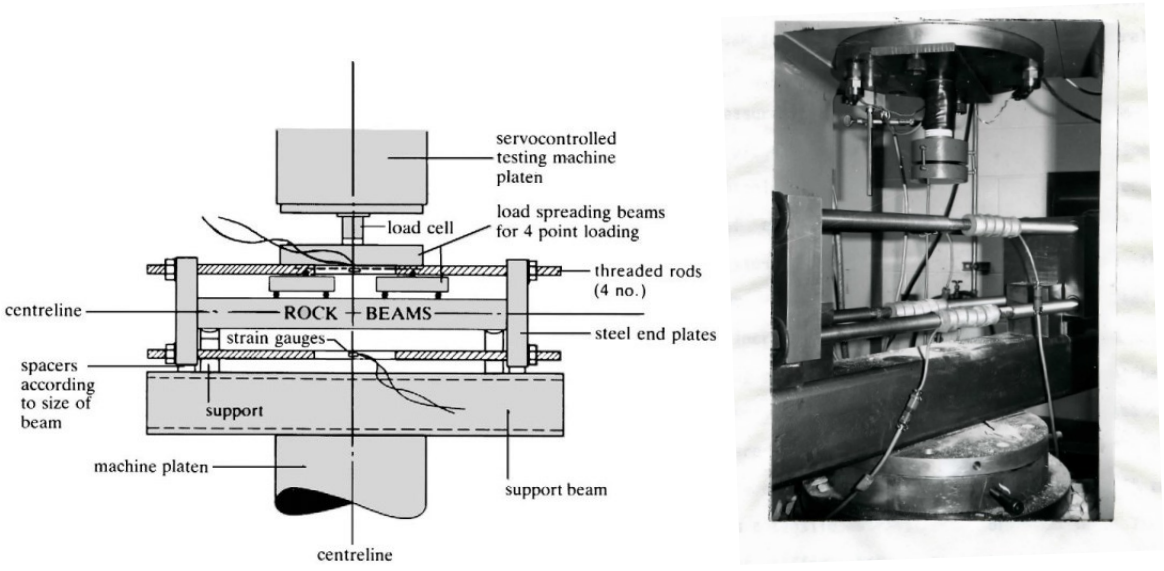

Figure 1-10 Testing Apparatus built by Sterling (Sterling, 1977)

Ahmed (Ahmed, 1990; Stimpson & Ahmed, 1992) built a similar apparatus to Sterling's with one modification by applying strain gauges on the front and back surfaces of the rock beam (Figure 1-11). The strain gauges can indicate the failure mechanism of the rock beam.

This experimental work on thick beams reveals a progressive fracture phenomenon in which failure occurs by shearing along a diagonal crack. Clearly, this is a different failure mechanism than the rotational or crushing failures that occur in thin beams. There must be a transition area between buckling, crushing, and sliding failure mechanisms.

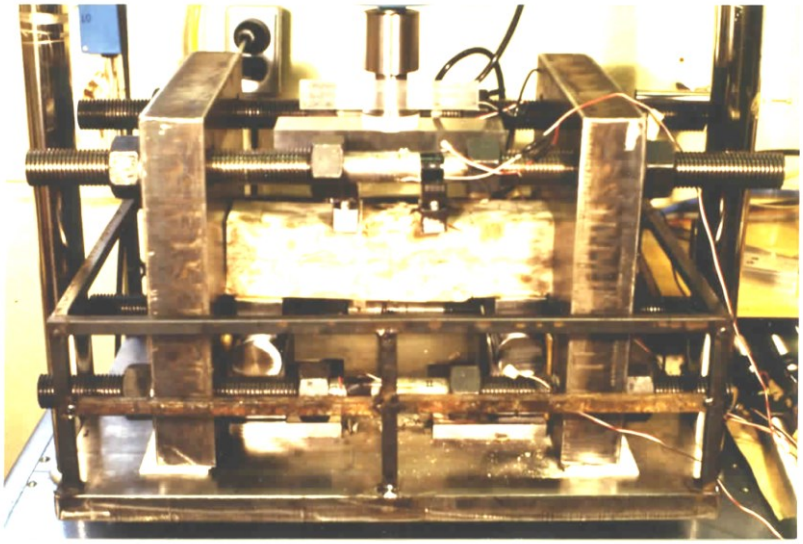

Figure 1-11 The testing frame built by Ahmed (Ahmed, 1990)

Given the limitation of the size of the rock beam surfaces, only one strain gauge can be applied. The stress distribution at the beam ends and the crack near the midspan cannot be measured, and the accuracy of the stress eccentricity at the ends is doubtful as it is calculated by the force measured at the restraining bars.

Mottahed (Mottahed & Ran, 1995) performed both physical and finite element testing. The physical tests involved voussoir beams cut from two types of Durox bricks made of lightweight

concrete. Because the lightweight concrete has low values for Young's modulus and compressive strength, the model beams failed at low transverse loads. This meant that the horizontal movement of both abutments was negligible; the abutments were therefore assumed to be rigid. This assumption, under which the tests were conducted, is valid; however, in reality, some small abutment movement occurs. Under the experimental conditions, almost all of the modelled voussoir beams failed by crushing at the high stress areas located at the ends and at the midspan. While Mottahed does not identify where crushing first occurred, the author believes that crushing occurred first at the abutments. This is because, as the beam deflects, the compressive stresses that are generated are being concentrated more at the ends than at the center. Consequently, the maximum stress generated at the ends is greater than that at the center.

Talesnick (Talesnick, 2007; Talesnick, Bar Ya'acov, & Cruitoro, 2007) studied the behavior of voussoir beams comprised of 6 plaster blocks using a centrifuge. Voussoir beam models of two different geometries were investigated. While both have the same length and width, one has half the thickness of the other. Displacements at the ends of each block were monitored by 12 LVDTs, and three pairs of strain gauges were used to measure the strain developed at the top, middle, and bottom of one of the blocks. Thrust was monitored by a load cell at the end. The model was subjected to accelerations of up to 90g. It was found that small rotation and displacement of the block near the abutment were required in order to set up a stable linear arch. Based on the two models tested, the thrust developed is independent of beam thickness. The depth of the strain distribution ranges from the whole thickness of the beam near the abutment to half of the beam thickness near the midspan.

Yang (Yang & Shang, 2007) modelled the voussoir beam using plaster blocks. The schematic of his frame is shown in Figure 1-13. Stress sensor 1 in Figure 1-13 was used to monitor the

horizontal thrust during the test, and the initial constraining stress was applied by tightening the nut and measured using stress sensor 2. The span/depth ratio and the initial constraining stress was found to affect the behavior of the moment arm and the horizontal stress in the voussoir beam. The stress distribution was not investigated.

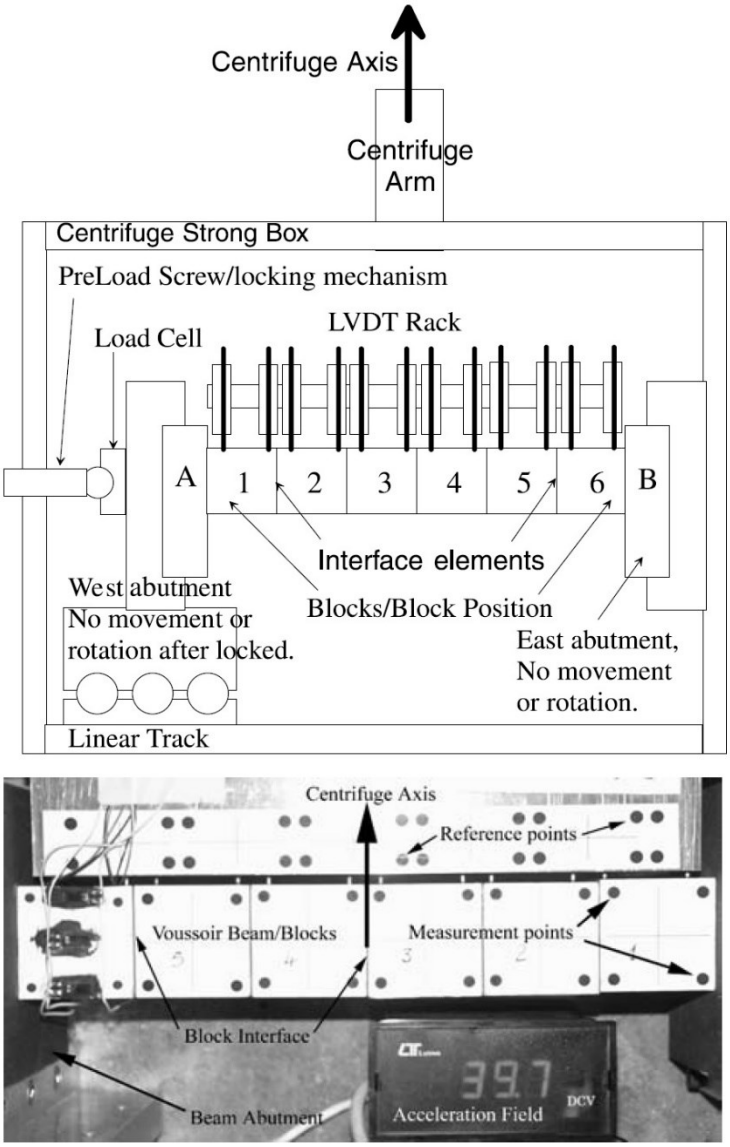

Figure 1-12 Schematic representation (top) and image of Talesnick's setup (bottom) (Talesnick, 2007; Talesnick et al., 2007)

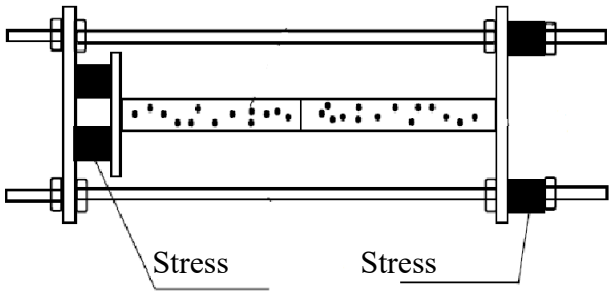

Figure 1-13 Schematic diagram of Yang's frame (Yang & Shang, 2007)

1.3.3 Numerical Investigations

Wright (Wright, 1974) did not think that an analytical approach was adequate to solve the voussoir model: "An analytical solution to the forces and stresses acting in a cracked beam was attempted but could not be solved without some prior simplifying assumptions which, it was felt, were more apt to be wrong than right." Instead, his investigation procedure was to first model the behavior of voussoir beams with a finite element method. The formulas expressing the relationship between the parameters were then derived from the numerical analysis results (see Table 1-2). Moreover, the formulas were checked using the physical experiments.

In the numerical model, the beams were self-loaded with rigid abutments (i.e., with fixed nodal points along the abutments). The points on the center line were allowed to move horizontally, but not vertically. Due to the limitations of the finite-element method, no separation or opening is allowed at discontinuities (which are found at the abutment and midspan of the voussoir beam in this model) (Jing & Hudson, 2002). The cracks were modeled by thin-column elements, while the closed cracks had the same modulus as the rest of the beam, and open cracks had a much lower modulus. For each model, several computer runs were performed to adjust the cracks to the "correct lengths" in order to properly model the behavior of discontinuities.

From the simulation results, the formulas of the moment arm at zero initial constraining stress (z_0 in Equation 1-4), the horizontal thrust (T in Equation 1-5) and the deflection at the centre (δ in Equation 1-6) were derived for a given span (s) and depth (t), initial constraining force (P), Young's modulus (E), and the transverse load (Q) of the beam.

For the stress at the abutments and midspan, Wright's results indicate that the assumption used in Evans's approach of $n = 0.5$ and the extent of the compression zones (nt) being the same at the abutments and midspan is incorrect. The depth of the stress distribution at the abutment (nt) is about half as much as it is at the midspan (Nt), which is also less than $0.5t$. As a result, the maximum stress at the abutment (σ_A) is much larger than the maximum stress at the midspan (σ_M). Wright's results also indicate that the shape of the stress distributions acting at the abutments and midspan are not triangular. However, the stress distributions appear to approach a triangular shape in beams with a high span to depth ratio (s/t). In Wright's follow-up analysis, a workable assumption for engineering design is that the same triangular stress can be distributed over the abutments and the midspan. This provides the formula for the maximum stress in the beam (σ_{max} in Equation 1-7).

$$z_0 = 0.44\frac{t^2}{s} + 0.91t \qquad \text{Equation 1-4}$$

$$T = \frac{Pt}{4z} + \sqrt{\frac{P^2(8t^2 - 4zt + t^2)}{8z^2} + \frac{Qs(Qs - 4Pt)}{64z^2}} \qquad \text{Equation 1-5}$$

$$\delta = \frac{Ps^2}{16Et^2} + 1.2z\left(\frac{s}{t}\right)^{1.78}\sqrt{\frac{T-P}{tE}\left(\frac{T-P}{tE} - \frac{0.23P\left(s/t\right)^{0.22}}{zE}\right)} \qquad \text{Equation 1-6}$$

$$\sigma_{max} = \frac{2T}{3\overline{x_A}} \qquad \text{Equation 1-7}$$

Wright introduced an iteration procedure (Figure 1-14) to determine the maximum stress in the voussoir beam.

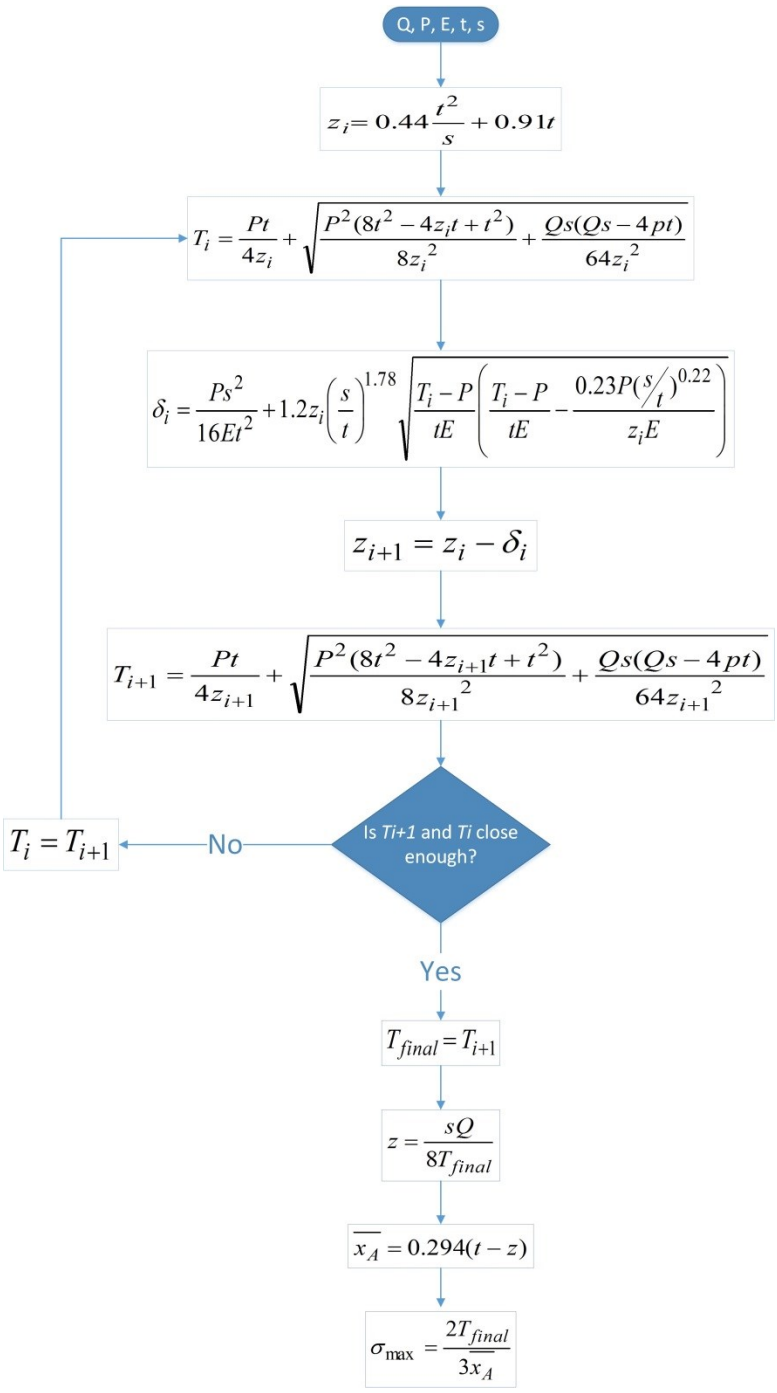

Figure 1-14 Iteration flowchart introduced by Wright to determine the maximum stress (Wright, 1974)

In addition to considering instances with cracks only at the abutments and midspan, Wright examined the effects of having multiple transverse cracks. Based on this, it was determined that

the cracked beam causing maximum stress concentration is typically cracked at the abutment and midspan only.

Table 1-2 Finite elements analysis by Wright (Wright, 1974)

No.	Span/Depth (s/t)	Initial constraining load (P/tE)	Transverse Load (Q/tE)	Thrust (T/tE)	Deflection (δ/t)	Moment Arm (z/t)	Centroidal distance at the abutment ($\overline{x_A}/_t$)
1	4	0	3.829E-07	2.374E-07	2.800E-06	0.8066	0.0542
2	4	0	6.927E-07	4.293E-07	5.100E-06	0.8066	0.0535
3	4	0	6.9269E-06	4.2925E-06	5.160E-05	0.8069	0.0535
4	4	0	2.608E-05	1.624E-05	1.910E-04	0.8028	0.0600
5	4	0	4.717E-05	2.923E-05	3.510E-04	0.8069	0.0578
6	4	1.667E-04	1.647E-04	1.748E-04	5.910E-04	0.4712	0.2024
7	4	1.667E-04	2.608E-04	2.074E-04	1.162E-03	0.6288	0.1301
8	6	0	5.744E-07	5.190E-07	1.190E-05	0.8300	0.0528
9	6	0	5.744E-06	5.211E-06	1.190E-04	0.8268	0.0551
10	6	0	1.039E-05	9.443E-06	2.160E-04	0.8253	0.0550
11	6	0	3.912E-05	3.555E-05	1.830E-04	0.8252	0.0550
12	6	0	7.077E-05	6.430E-05	1.471E-03	0.8253	0.0536
13	6	1.111E-04	7.076E-05	1.146E-04	6.430E-04	0.4630	0.2066
14	6	1.111E-04	1.039E-04	1.281E-04	1.145E-03	0.6086	0.1365
15	12	0	1.488E-06	1.949E-06	1.590E-04	0.8841	0.0371
16	12	0	1.149E-05	1.939E-05	1.583E-03	0.8886	0.0373
17	12	0	1.415E-05	2.402E-05	1.950E-03	0.8835	0.0371
18	12	0	1.415E-05	2.592E-05	2.189E-03	0.8190	0.0573
19	12	0	1.415E-05	2.608E-05	2.180E-03	0.8140	0.0584
20	12	0	7.823E-05	1.339E-04	1.108E-02	0.8764	0.0364
21	12	0	1.415E-04	2.441E-04	2.052E-02	0.8694	0.0414
22	12	5.555E-05	4.941E-05	9.467E-05	4.830E-03	0.7829	0.0631
23	12	5.555E-05	7.823E-05	1.418E-04	8.869E-03	0.8278	0.0493
24	12	5.555E-05	1.415E-04	2.477E-04	1.740E-02	0.8571	0.0443
25	24	0	2.298E-06	7.511E-06	2.333E-03	0.9177	0.0311
26	24	0	1.565E-05	5.263E-05	1.648E-02	0.8919	0.0282
27	24	0	2.298E-05	7.762E-05	2.462E-02	0.8881	0.0280
28	24	2.777E-05	9.883E-06	3.852E-05	6.214E-03	0.7697	0.0590
29	24	2.777E-05	1.565E-05	5.642E-05	1.215E-02	0.8278	0.0418
30	24	2.777E-05	4.156E-05	1.452E-04	4.186E-02	0.8587	0.0305

In Wright's numerical model, the "correct lengths" of the cracks at the midspan and abutments were determined by the researcher's knowledge and experience. Notably, the numerical analysis results were highly determined by the length of cracks. The finite-element method may not be suitable for modeling the voussoir beam. The slide failure at the abutment was prevented by the fixed abutments in the model. The deflections at the center of the beam in the results were also questionable as the center line had been fixed in a vertical direction in the model. These limitations in the numerical model made it an inadequate representation of the voussoir beam in reality.

Passaris et al. (Mottahed, Passaris, & Ran, 1993; Passaris, Ran, & Mottahed, 1993) performed a finite-element analysis of the voussoir beam, proving that the stress distribution at the abutment and midspan is linear and the depth of stress distribution at the midspan is twice what it is at the abutment. Ran et al. (Ran, Passaris, & Mottahed, 1994) used the finite-element method to examine the shear failure mode. Mottahed and Ran (Mottahed & Ran, 1995) performed both physical and finite element testing. The finite-element approach considered triangular stress distributions acting at the midspan and abutments and the depth of these distributions were assumed to be equal on both sides. The results showed that a linear analysis of the structure is inappropriate for describing the beam behavior. Based on these conclusions, equations were derived for the thrust, lever arm, centroid location, and crushing strength using non-linear analysis.

Nomikos et al. (Nomikos, Sofianos, & Tsoutrelis, 2002) investigated the voussoir beam with multiple joints with the distinct element code, UDEC. The numerical results indicate that the beam deflection increases and the maximum strain at the abutment decreases with the increase in joint frequency and compliance.

Hatzor and Benary (Y. Hatzor & Benary, 1998) investigated the roof failure of an ancient water reservoir in stratified and jointed chalk using Discontinuous Deformation Analysis (DDA). According to the voussoir beam analysis procedure proposed by Beer (Beer & Meek, 1982; Brady & Brown, 1993), this case should have been safe against both sliding and crushing failure. By contrast, DDA predicted the shear failure of this case successfully. Hatzor concluded that Beer's analysis (which he describes as "the classical voussoir theory") failed to assess the stability of the voussoir beam by not considering the joint spacing and joint friction.

Similar to Hator's research, Bakun-Mazor (Bakun-Mazor et al., 2009) examined the roof stability of a free-standing quarry in stratified and jointed rock using an integrated approach of geologically based Discrete Fracture Network (geoDFN) with Discontinuous Deformation Analysis (DDA). According to the iteration method for voussoir beam analysis proposed by Diederichs and Kaiser (M. Diederichs & Kaiser, 1999c), the roof should fail by buckling; however, this is not what happened in the field in this case. Bakun-Mazor proposed that the current voussoir beam theory does not captured the arching mechanism in the stratified and jointed rock mass.

Calibrated to Talesnick's physical modeling results (Talesnick et al., 2007), Tsesarsky (Tsesarsky & Talesnick, 2007) modeled the multi-jointed voussoir beam with FLAC (Fast Lagrangian Analysis of Continua). Tsesarsky found the thickness of the compressive arch varies from 0.8t (where t is the thickness of the beam) at the abutment to 1t at the ¼ of the span, and has a value of 0.5t at midspan. This result was modified in his later research (Tsesarsky, 2012). The thickness of the compressive arch ranges from 0.3t to 0.4t at the abutment and is inversely proportional to beam stiffness. The thickness of the compressive arch ranges from 0.4t to 0.5t at the mid-span.

1.3.4 Discussion

Based on the above literature review, a number of questions emerge with respect to assumptions about the stress distribution size and shape that lead to incompatibilities between results obtained by different investigators. All the analyses, except for Sterling's, assume triangular-shaped stress distributions of equal size acting at the abutment and midspan. Sterling dealt with six different stress distribution shapes, of which the rectangular-shaped stress block, which had equal depth at the abutment and midspan, gave the best fit to his experimental data. Nevertheless, Wright's results indicate that Sterling's finding in this case was incorrect. His results indicated that the induced lateral stresses, developed at the abutments and midspan, increase in a non-linear manner and that the depths over which they act are not equal.

In reality, the stress distribution along the boundary is not necessarily linear, and experimental studies are necessary to determine its exact geometry (Tsesarsky & Talesnick, 2007). Based on the review of the experimental investigations, no test results were able to give the stress distributions at the abutments and midspan as either the beam tested was an intact beam or the instruments used were limited.

Two discontinuum numerical codes, UDEC and DDA, were employed to model the voussoir beams. However, the UDEC did not account for the crack developing inside the voussoir blocks, and the DDA is unable to give stress distributions at the edge of blocks. A new numerical code is needed to model the behavior of voussoir beams and to simulate all four failure modes of voussoir beams (shear sliding, buckling/snap through, crushing and cracking).

1.4 Research Objectives

The objectives of this research are:

a) To determine the arching mechanism that happened within the single-layer voussoir beam with joints at the center and abutment only;
b) To develop the ultimate load analysis procedure to determine stability and deflection of the voussoir beams.
c) To extend the procedure in order to analyze the segmental concrete liners which are widely used in mechanized tunneling.

1.5 Methodology

Physical modeling, numerical modeling, analytical investigation, and a case study will be used to investigate the arching mechanism occurred in stratified and jointed rock and to develop the overall roof design procedure for the excavations in a stratified rock mass.

The proposed research will start with physical modeling and numerical modeling in order to systematically investigate the behavior of voussoir beams under transverse loading. The theoretical analysis of voussoir beam with joints at the abutment and midspan only will inform the general design procedure for voussoir beams based on previous findings. The design procedure will be applied to determine the segmental concrete liner used in a City of Edmonton tunnel.

1.5.1 Physical Modeling

The experiments will be performed to test the behavior of a voussoir beam of a single layer with only three joints against transverse loading. The test results will be used to both verify and refine the theoretical analysis and to calibrate the numerical model. A digital image correlation system will be used for strain measurement. The stress distribution can be obtained from strain measured.

1.5.2 Numerical Modeling

Numerical modeling will be performed as a complementary research method to investigate the behavior of the voussoir beam. The effect of some factors upon the stability of the voussoir beam is not easy to model physically; numerical experiments will therefore be performed instead.

As discussed in the numerical investigation, a numerical method that can effectively capture the joints' behavior and allow significant displacement along the joints would be the ideal code for numerical modeling. *Phase*^{2} of Rocscience is selected for the numerical modeling.

1.5.3 Analytical Investigation

The analysis will be based on a general form of stress distribution at the abutment and midspan with different depths of stress distributions. This form is under elastic buckling (i.e., no crushing), with the beam being free of any lateral stress. In order to resolve incompatibilities, a more generalized non-linear analytical analysis will be carried out that assumes the stress distributions at the abutment and midspan are described by a power function of the form, as shown in Equation 1-8.

$$\sigma(x) = \beta x^k \qquad \text{Equation 1-8}$$

where k is a positive constant and where these stress distributions are of different depth.

1.5.4 Case Study

Segmental concrete liners are widely used in mechanical tunneling. In the City of Edmonton, the 4-piece segment liners are used for TBM (tunnel boring machine) tunneling; however, there is always uncertainty about the joints strength of segmental liners. From this investigation, the voussoir beam theory will be applied to determine the stress and deflection of the stress riser (one type of joints) of segmental liner used by the City of Edmonton. Voussoir beam theory will provide an analytical method for the design of segmental tunnel liners.

1.6 Thesis Outline

Chapter 1 introduces the research topic of voussoir beam theory. The items included are a brief introduction, the application, literature review, research objectives, and research methodology.

Chapter 2 covers the selection and characterization of the synthetic rock. Appropriate materials need to be selected for the physical investigation of natural rock behavior. Two kinds of material were selected. Characterization tests were performed to obtain the mechanical properties of the selected material.

Chapter 3 describes the physical investigation of the voussoir models. Voussoir beam models under transverse loading were tested. The application of the Vic-3d correlation system enables the direct measurement of the displacement on the surface of voussoir beam during the test.

Chapter 4 covers the numerical investigation of the voussoir models. *Phase2* was selected to model the behavior of voussoir beams. Numerical models were calibrated by the physical tests first. Voussoir beams of common range of span/depth ratios were modeled.

Chapter 5 describes the theoretical modeling of the voussoir beams. A theoretical model was established based on a generic form of stress distribution. The results from the physical and numerical modeling were used to make the theoretical model solvable.

Chapter 6 covers the application of the theoretical model to determine the mechanical behavior of stress riser of the precast segmental concrete liner. This chapter is based on the concrete liners used in City of Edmonton tunneling. Voussoir beam theory was firstly applied to analyze the performance of concrete liners.

Chapter 7 describes the conclusions, major contributions and recommendations for future research.

References

Ahmed, M. (1990). A study of possible failure mechanisms for mining-induced seismicity in saskatchewan (Ph.D.). Available from ProQuest Dissertations & Theses (PQDT). (303854413).

Bakun-Mazor, D., Hatzor, Y. H., & Dershowitz, W. S. (2009). Modeling mechanical layering effects on stability of underground openings in jointed sedimentary rocks. International Journal of Rock Mechanics and Mining Sciences, 46(2), 262-271. doi:10.1016/j.ijrmms.2008.04.001

Beer, G., & Meek, J. L. (1982). DESIGN CURVES FOR ROOFS AND HANGING-WALLS IN BEDDED ROCK BASED ON VOUSSOIR BEAM AND PLATE SOLUTIONS. Transactions of the Institution of Mining and Metallurgy Section a-Mining Industry, 91(JAN), A18-A22.

Betournay, M. (1987). A design philosophy for surface crown pillars of hard rock mines. Cim Bulletin, 80(903), 45-61.

Brady, B. H. G., & Brown, E. T. (1993). Rock mechanics: For underground mining / B.H.G. brady, E.T. brown London; New York: Chapman & Hall, 1993; 2nd ed.

Brady, B. H. G., & Brown, E. T. (2004). Rock mechanics: For underground mining Kluwer Academic Publishers.

Diederichs, M. S. (2000). Instability of hard rockmasses: The role of tensile damage and relaxation (Ph.D.). Available from ProQuest Dissertations & Theses Full Text. (304676346).

Diederichs, M., & Kaiser, P. (1999a). Authors' reply to discussion by A.L. sofianos regarding diederichs M.S. and raiser P.K. stability of large excavations in laminated hard rock masses: The voussoir analogue revisited. international journal of rock mechanics & mining sciences. 1999; 36: 97-117. International Journal of Rock Mechanics and Mining Sciences, 36(7), 995-997. doi:10.1016/S0148-9062(99)00058-3

Diederichs, M., & Kaiser, P. (1999b). Stability of large excavations in laminated hard rock masses: The voussoir analogue revisited. International Journal of Rock Mechanics and Mining Sciences, 36(1), 97-117. doi:10.1016/S0148-9062(98)00180-6

Diederichs, M., & Kaiser, P. (1999c). Tensile strength and abutment relaxation as failure control mechanisms in underground excavations. International Journal of Rock Mechanics and Mining Sciences, 36(1), 69-96. doi:10.1016/S0148-9062(98)00179-X

Evans, W. H. (1941). The strength of undermined strata. Trans. Inst. of Mining and Metallurgy, 50, 475-500.

Hatzor, Y., & Benary, R. (1998). The stability of a laminated voussoir beam: Back analysis of a historic roof collapse using DDA. International Journal of Rock Mechanics and Mining Sciences, 35(2), 165-181. doi:10.1016/S0148-9062(97)00309-4

Hatzor, Y. H. (2012). Risk assessment of collapse in shallow caverns using numerical modeling of block interactions with DDA: Suggested approach and case studies. International Top-Level Forum on Engineering Science and Technology Development Strategy — Safe Construction and Risk Management of Major Underground Engineering, Wuhan China.

Jing, L., & Hudson, J. (2002). Numerical methods in rock mechanics. International Journal of Rock Mechanics and Mining Sciences, 39(4), 409-427. doi:10.1016/S1365-1609#02#00065-5

Miller, F., & Choquet, P. (1988). Analysis of the failure mechanism of a layered roof in long hole stopes at mines gaspe. Cim Bulletin, 81(911), 88-88.

Mottahed, P., Passaris, E., & Ran, J. (1993). Strength of the jointed roof of an underground mine opening in stratified rock. Cim Bulletin, 86(972), 37-44.

Mottahed, P., & Ran, J. (1995). DESIGN OF THE JOINTED ROOF IN STRATIFIED ROCK BASED ON THE VOUSSOIR BEAM MECHANISM. Cim Bulletin, 88(994), 56-62.

Nomikos, P., Sofianos, A., & Tsoutrelis, C. (2002). Structural response of vertically multi-jointed roof rock beams. International Journal of Rock Mechanics and Mining Sciences, 39(1), 79-94. doi:10.1016/S1365-1609(02)00019-9

Passaris, E., Ran, J., & Mottahed, P. (1993). Stability of the jointed roof in stratified rock. International Journal of Rock Mechanics and Mining Sciences & Geomechanics Abstracts, 30(7), 857-860. doi:10.1016/0148-9062(93)90036-D

Ran, J., Passaris, E., & Mottahed, P. (1994). Shear sliding failure of the jointed roof in laminated rock mass. Rock Mechanics and Rock Engineering, 27(4), 235-251. doi:10.1007/BF01020201

Sofianos, A. (1996). Analysis and design of an underground hard rock voussoir beam roof. International Journal of Rock Mechanics and Mining Sciences & Geomechanics Abstracts, 33(2), 153-166. doi:10.1016/0148-9062(95)00052-6

Sofianos, A. (1999). Discussion of the paper by M.S. diederichs and P.K. kaiser "stability of large excavations in laminated hard rock masses: The voussoir analogue revisited", international journal of rock mechanics and mining sciences, 36, 97-117 (1999). International Journal of Rock Mechanics and Mining Sciences, 36(7), 991-993. doi:10.1016/S0148-9062(99)00057-1

Sofianos, A., & Kapenis, A. (1998). Numerical evaluation of the response in bending of an underground hard rock voussoir beam roof. International Journal of Rock Mechanics and Mining Sciences, 35(8), 1071-1086. doi:10.1016/S0148-9062(98)00166-1

Sterling, R. L. (1977). ROOF DESIGN FOR UNDERGROUND OPENINGS IN NEAR-SURFACE BEDDED ROCK FORMATIONS (Ph.D.). Available from ProQuest Dissertations & Theses (PQDT). (302852510).

Stimpson, B., & Ahmed, M. (1992). FAILURE OF A LINEAR VOUSSOIR ARCH - A LABORATORY AND NUMERICAL STUDY. Canadian Geotechnical Journal, 29(2), 188-194.

Talesnick, M. L. (2007). Determination of shear interface parameters between rock blocks for centrifuge modeling. Rock Mechanics and Rock Engineering, 40(4), 405-418. doi:10.1007/s00603-006-0118-3

Talesnick, M. L., Bar Ya'acov, N., & Cruitoro, A. (2007). Modeling of a multiply jointed voussoir beam in the centrifuge. Rock Mechanics and Rock Engineering, 40(4), 383-404. doi:10.1007/s00603-006-0104-9

Tsesarsky, M. (2012). Deformation mechanisms and stability analysis of undermined sedimentary rocks in the shallow subsurface. Engineering Geology, 133, 16-29. doi: 10.1016/j.enggeo.2012.02.007

Tsesarsky, M., & Talesnick, M. L. (2007). Mechanical response of a jointed rock beam - numerical study of centrifuge models. International Journal for Numerical and Analytical Methods in Geomechanics, 31(8), 977-1006. doi:10.1002/nag.568

van der Merwe, N. (2009). The challenges of mining old, shallow, small coal pillars. ISRM Newsletter no.8

Wright, F. D. (1974). Design of roof bolt patterns for jointed rock. (USBM Grant Final Report). College of Engineering, University of Kentucky, distributed by National Technical Information Service, Springfield, Va.

Yang, J., & Shang, Y. (2007). Experimental study on complete mechanical characteristics of voussoir beam in stratified rock. Yanshilixue Yu Gongcheng Xuebao/Chinese Journal of Rock Mechanics and Engineering, 26, 2852-2857.

2 Selection and Characterizing the Synthetic Rock

Two kinds of materials, concrete and plaster were selected for the physical modeling of voussoir beams. And a standard testing program was performed to characterize the two materials.

The characterizing tests performed are (1) Uniaxial Compression Test, (2) Splitting Tensile Strength Test and (3) Sliding Friction Test.

The results from the tests provided the basic material properties for physical modeling, and were used to calibrate the numerical model in Chapter 4 too.

2.1 Selection of Synthetic Rock Material

In order to model the voussoir beam behavior of natural hard rock or artificial hard material, the brittleness and heterogeneity are the two important characteristics required for the selected material. On the other hand, the strength of the selected material should be lower than the natural rock to minimize the size and capacity of laboratory facilities. Referenced to the previous research on rock behaviors (Cho, 2008; Cui, 2012), concrete and plaster are selected as experimental material.

The mixing proportion for the two materials is in Table 2-1. Type GU Portland cement was used for concrete samples. Plaster of Paris which is local supplied was used for the plaster samples. And both concrete and plaster samples used the same sand, the concrete sand. The result of sieve analysis for the sand is in Figure 2-1. To be exactly, the concrete used is mortar essentially because no rock chippings or gravel used.

Table 2-1 Mixing proportion for experimental samples

	Mixing Ratio by weight
Concrete	cement : water : sand = 2 : 1 : 6.24
Plaster	plaster : water : sand = 3 : 2 :2

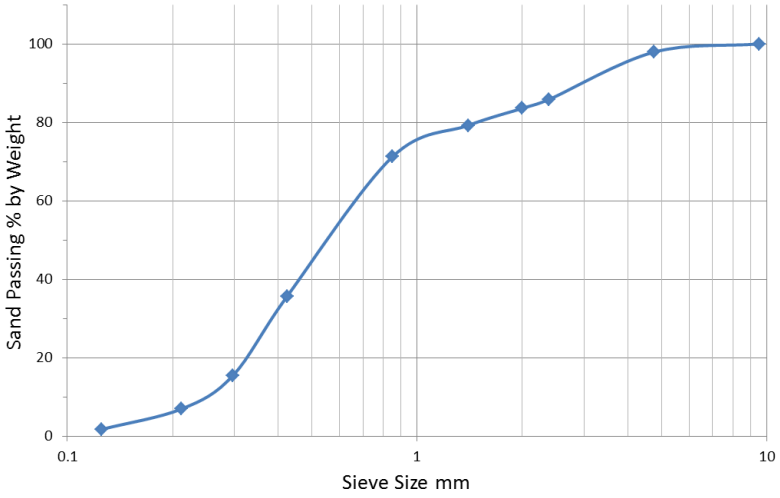

Figure 2-1 Sand Size Sieve Analysis

2.2 Specimen Preparation

Specimens in the shape of both cylinder and prism beam were casted. The cylinder specimens, which have a diameter of 50mm and length of 100mm, were used for uniaxial compression test and splitting tensile strength test. The prism beam specimens were used in sliding friction test and the voussoir beam modelling.

The making and curing procedure of concrete samples complied with ASTM C192 (ASTM, 2015a). All of the concrete specimens tested were after 28 days of curing.

The plaster specimens were removed from the molds several hours after casting. Then the specimens were put in laboratory for air dry. The water content in the specimen was monitored for 12 days after casting. The monitor result is shown in Figure 2-2. It is found that the water content in the specimen reaches an equilibrium level of 5.5 percent in weight at 7 days after casting. All the plaster specimens used in the followed tests were more than 12 days after casting.

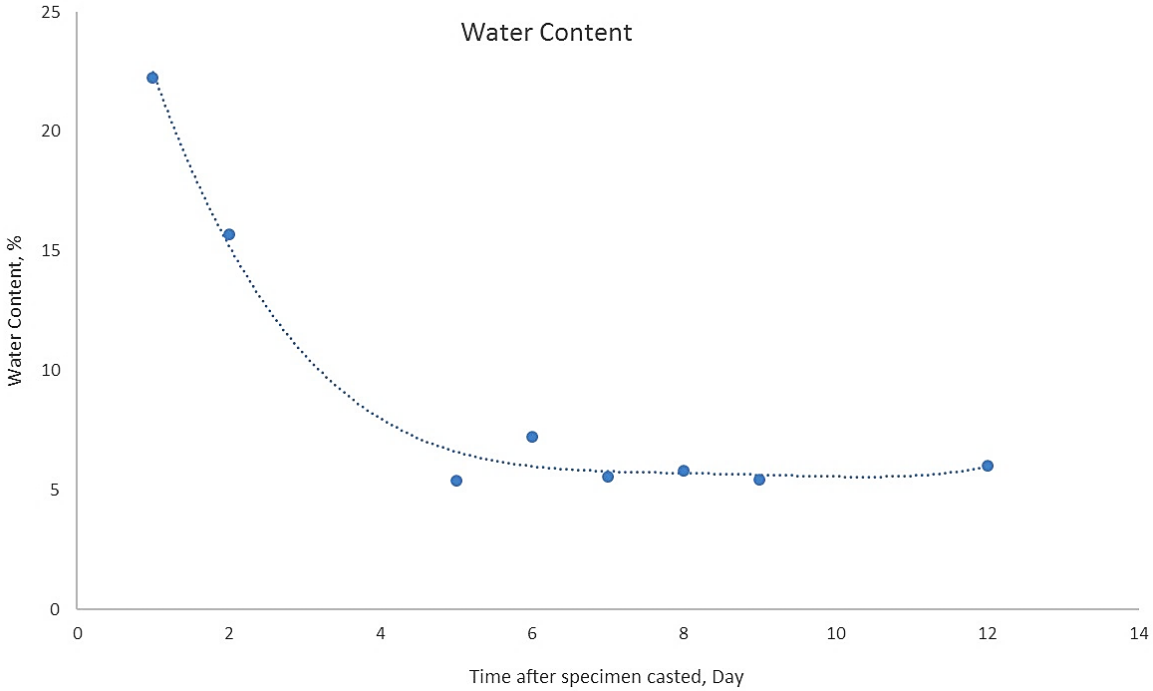

Figure 2-2 Water Content in Plaster Specimen under Air Dry

2.3 Uniaxial Compression Test

Uniaxial compression tests were performed according to ASTM C39 (ASTM, 2015b). The testing system is shown in Figure 2-3. The longitudinal strain was measured by three vertical LVDTs, and the transverse strain was measured by two horizontal LVDTs horizontally aligned and passing the center of the cylinder. The load was measured and recorded automatically by the loading frame. The rate of the loading frame is 0.005mm/s.

Figure 2-4 shows the typical failure shape of the concrete and plaster specimens. Both specimens have a larger than 45 degrees of fracture. Figure 2-5 shows the behavior of six concrete specimens in uniaxial compression testing. Figure 2-6 shows the relationship between the longitudinal strain and transverse strain for two concrete specimens. The transverse strain wasn't measured effectively for the other four concrete specimens. Figure 2-7 shows the behavior of four plaster specimens in uniaxial compression testing. Figure 2-8 shows the relationship between the longitudinal strain and transverse strain for two plaster specimens. The transverse strain wasn't measured effectively for the other two plaster specimens.

Figure 2-3 Uniaxial Compression Test System

Figure 2-4 Typical Failure Types in Uniaxial Compression Test; Plaster Sample left, Concrete Sample right

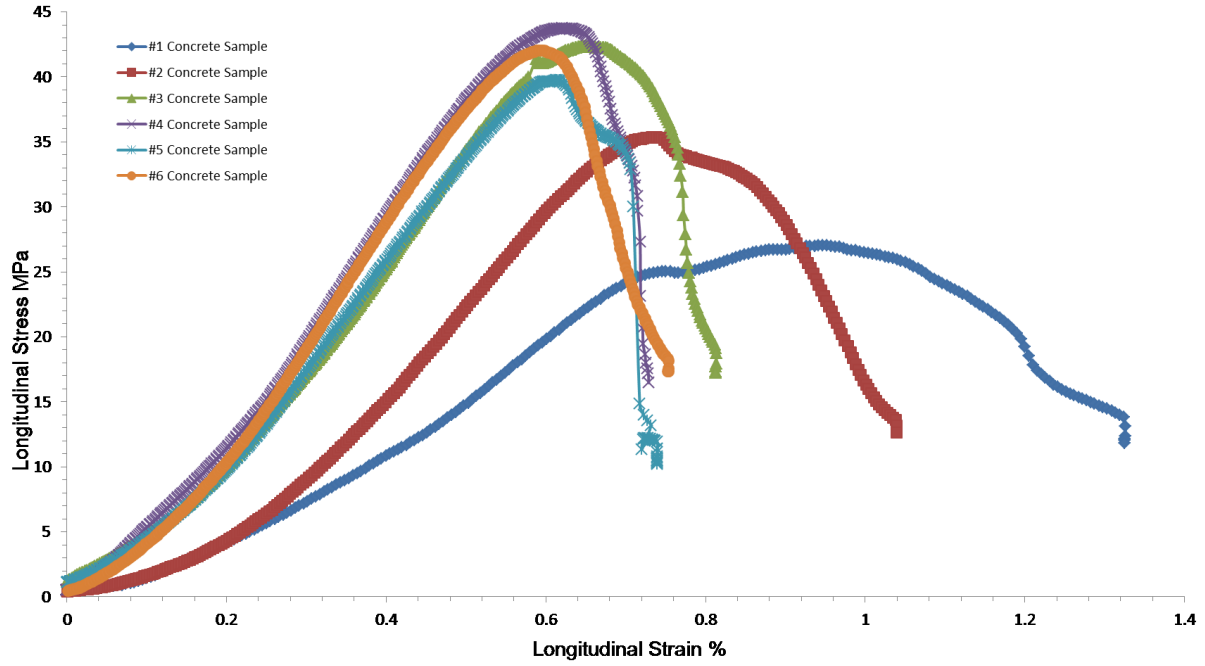

Figure 2-5 Uniaxial Compression Test results of concrete specimens

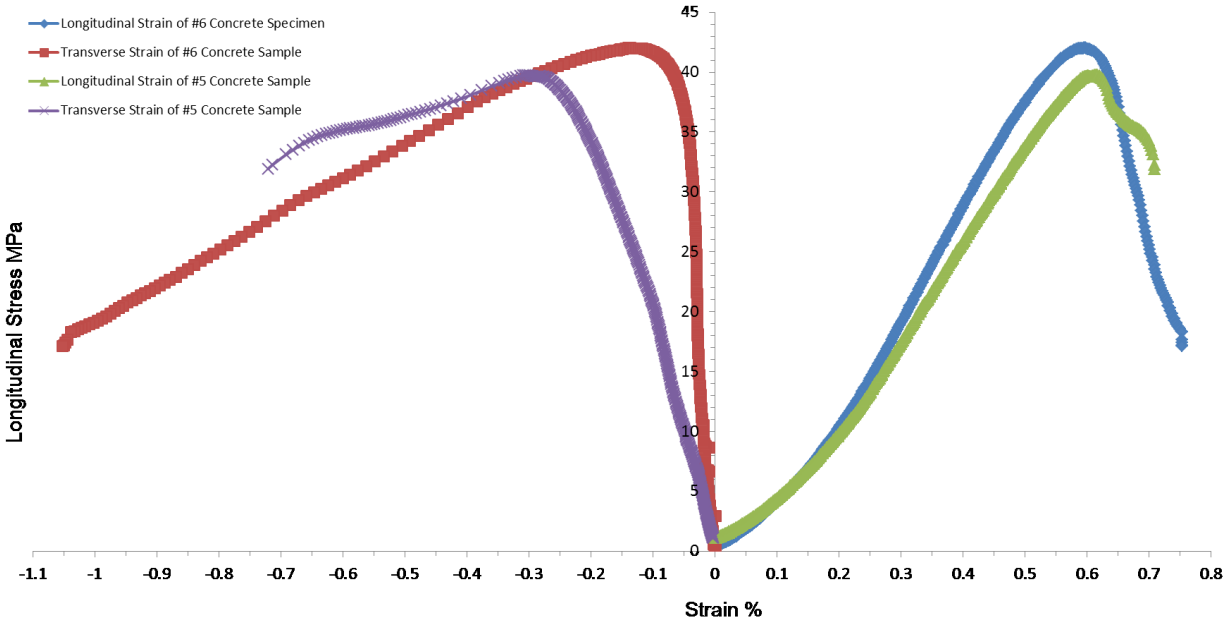

Figure 2-6 Comparison of longitudinal strain and transverse strain of 2 concrete specimens

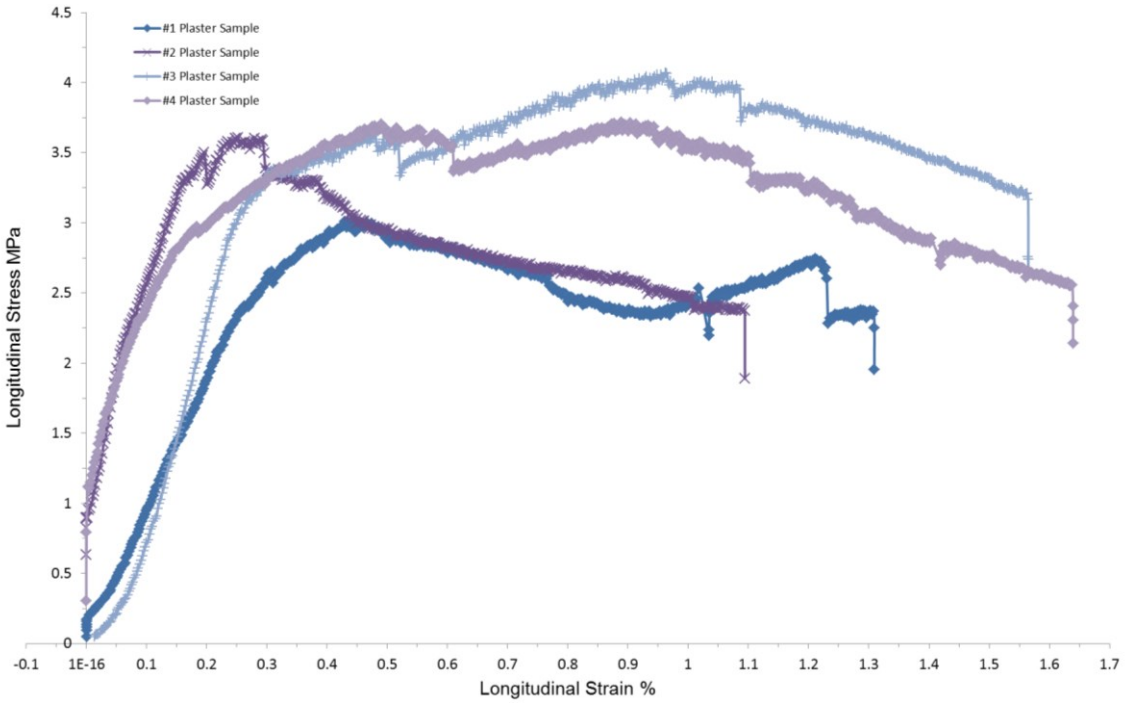

Figure 2-7 Uniaxial Compression Test results of plaster specimens

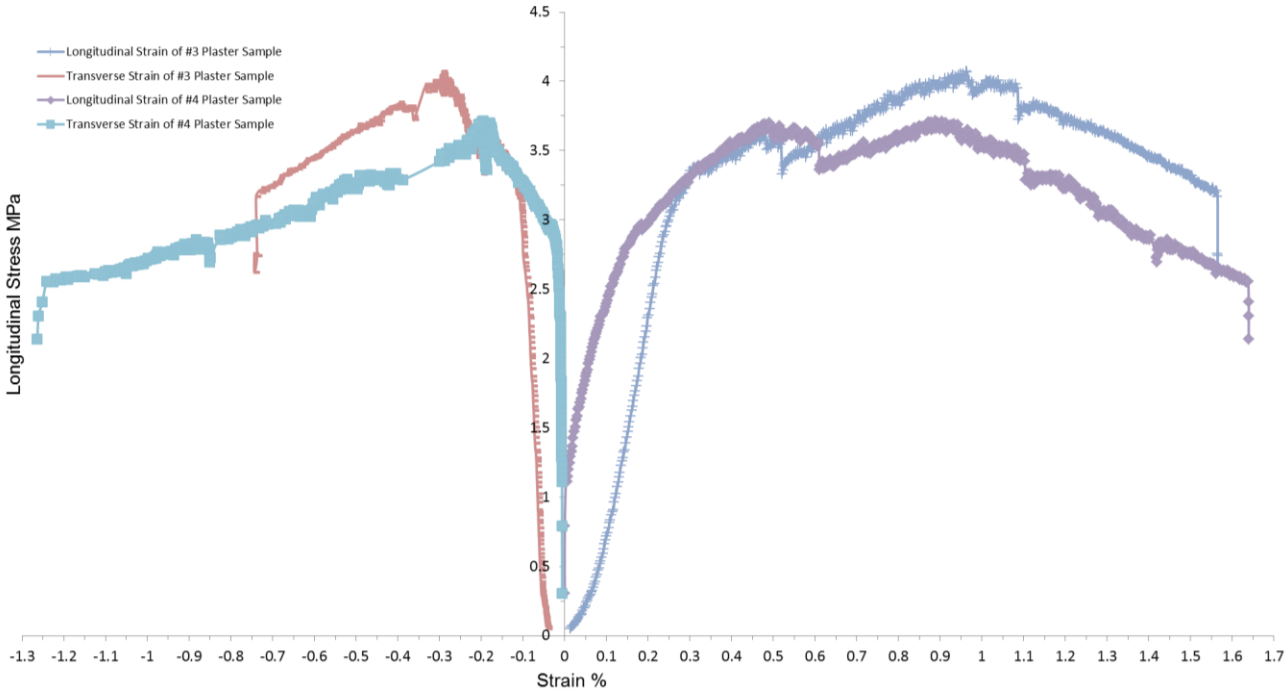

Figure 2-8 Comparison of longitudinal strain and transverse strain of 2 plaster specimens

2.4 Splitting Tensile Strength Test

Splitting tensile strength test was performed according to ASTM C496 (ASTM, 2011). The test frame is shown is Figure 2-9. Eight concrete specimens and three plaster specimens were tested for tensile strength. The typical failure of concrete specimens is shown in Figure 2-10. And the typical failure of plaster specimens is shown in Figure 2-11. The failure surface crossed the longitudinal axis of the specimen approximately. The testing result for concrete specimens is shown in Table 2-2. The testing result for plaster specimens is shown in Table 2-3. From the tests, the concrete has a tensile strength of 4.39 MPa, and the plaster specimen has a tensile strength of 0.94 MPa.

Figure 2-9 Testing frame with plaster sample for splitting tensile strength test

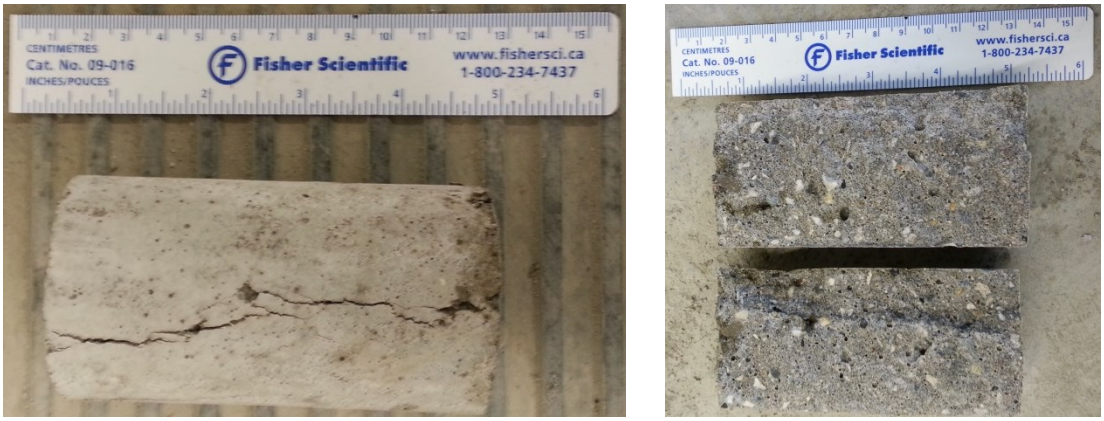

Figure 2-10 Typical failure shape of concrete sample in splitting tensile strength test

Figure 2-11 Typical failure shape of plaster sample in splitting tensile strength test

Table 2-2 Splitting Tensile Test Results for Concrete Specimens

Concrete sample	1	2	3	4	5	6	7	8
Length of sample, mm	104.77	104.31	102.48	105.36	106.62	106.42	104.31	104.48
Diameter of sample, mm	52.8	51.96	51.86	52.5	51.89	51.79	52.86	51.92
Maximum applied load, kN	33.4	31.8	37.4	39.5	39.4	40	41.1	38.9
Splitting tensile strength, MPa	3.85	3.74	4.48	4.55	4.54	4.62	4.74	4.57
Average Splitting tensile strength, MPa				4.39				
Standard Deviation of tensile strength				0.38				

Table 2-3 Splitting Tensile Test Results for Plaster Specimens

Plaster sample	1	2	3
Length of sample, mm	151.68	150.91	151.21
Diameter of sample, mm	76.75	76.78	77.54
Maximum applied load, kN	17.4	16.6	17.4
Splitting tensile strength, MPa	0.95	0.91	0.95
Average Splitting tensile strength, MPa		0.94	
Standard Deviation of Tensile Strength		0.02	

2.5 Sliding Friction Test

As the planar joints existing at the midspan and abutments of the voussoir beam model, it is necessary to investigate the behavior of the planar joint. Sliding friction tests on the planer continuous joint were carried out for concrete and plaster specimens. The testing system is shown in Figure 2-12. The system has load cell and LVDT in both shear and normal direction in order to measure shear force and displacement. The data were recorded by the data logger automatically. The samples were 50 mm by 50 mm and were put into the mold, see Figure 2-13. The normal load was applied on the top of the sample by loading weight when the normal stress was less than 500 kPa. Higher loads need to be applied via the cantilever arm at the bottom. Based on the available loading block, the plaster specimens were tested over normal stress ranging from 200 kPa to 800 kPa, and concrete specimens were tested over 250 kPa to 1 MPa.

The relationship between shear displacement and shear stress for concrete specimen is shown in Figure 2-14. The relationship between shear displacement and shear stress for plaster specimen is shown in Figure 2-15. From the previous relationship, the sliding shear behavior of the joints was found, as shown in Figure 2-16. It is found that the joint friction angle for concrete is 30.6 degrees and 36.7 degrees for plaster joint, as summarized in Table 2-4.

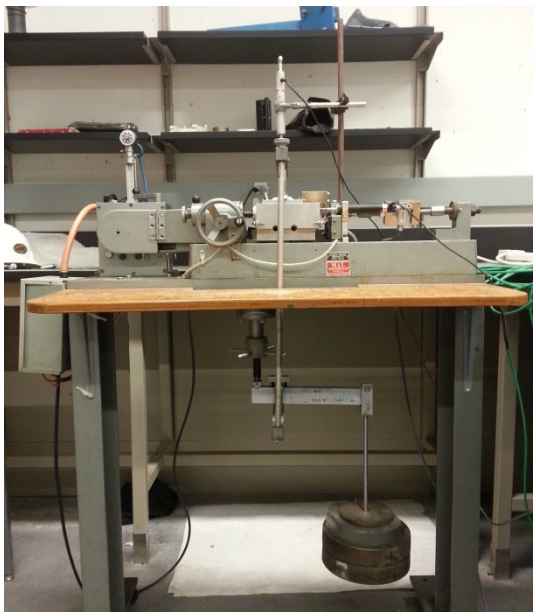

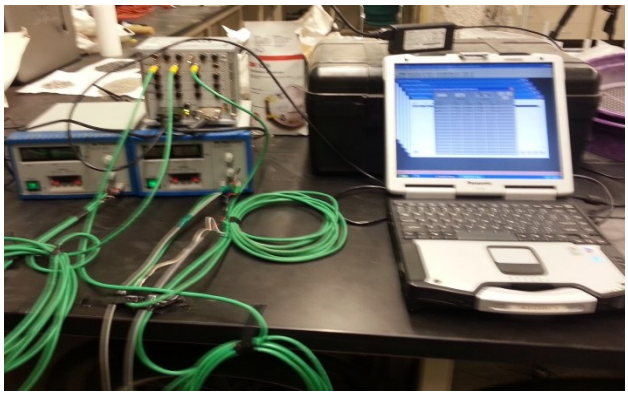

Figure 2-12 Direct Shear Test System with Data Logging

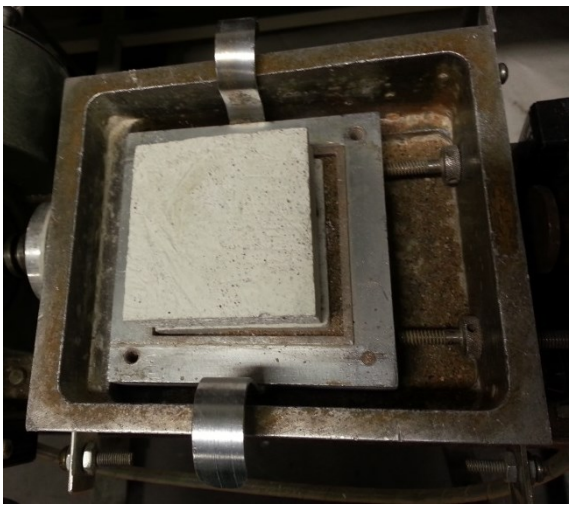

Figure 2-13 Lower Part of the Mold with Plaster Specimen

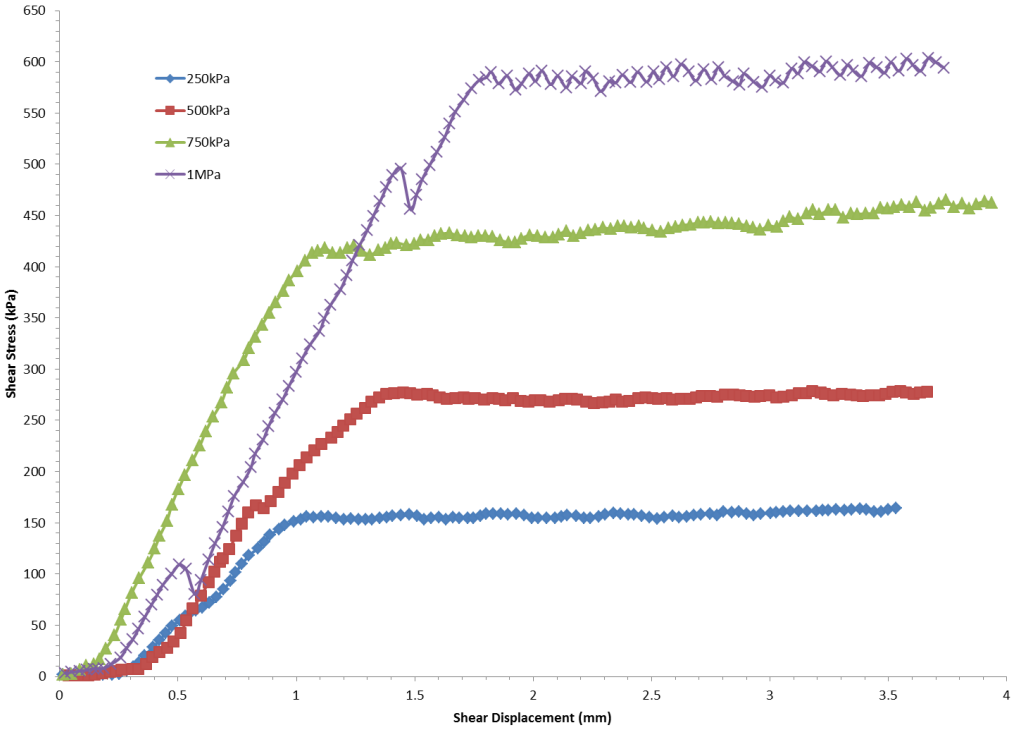

Figure 2-14 Shear Displacement – Shear Stress curve for concrete specimen under 4 different normal stresses

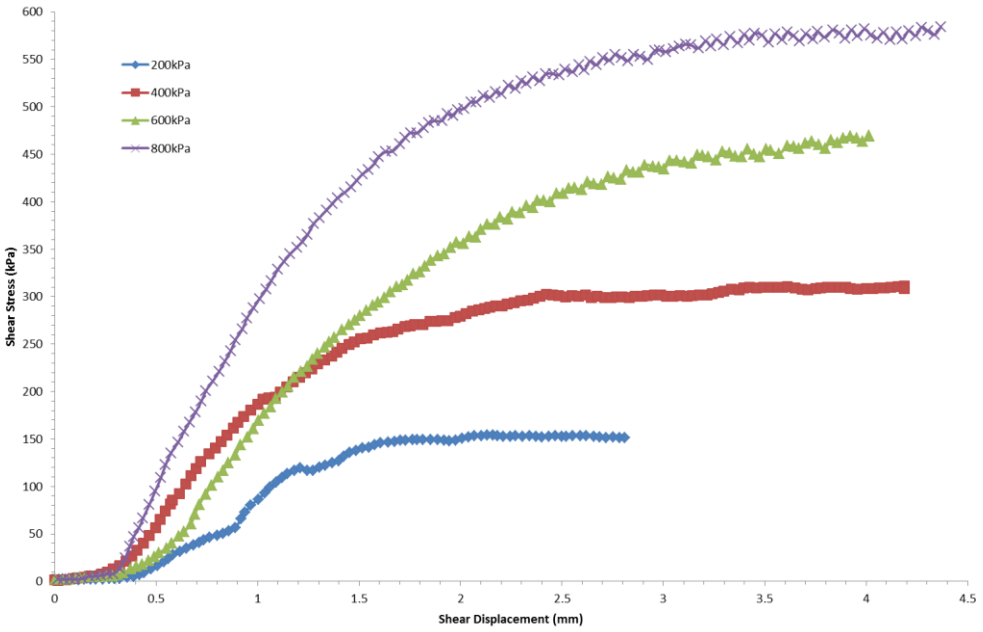

Figure 2-15 Shear Displacement – Shear Stress curve for plaster specimen under 4 different normal stresses

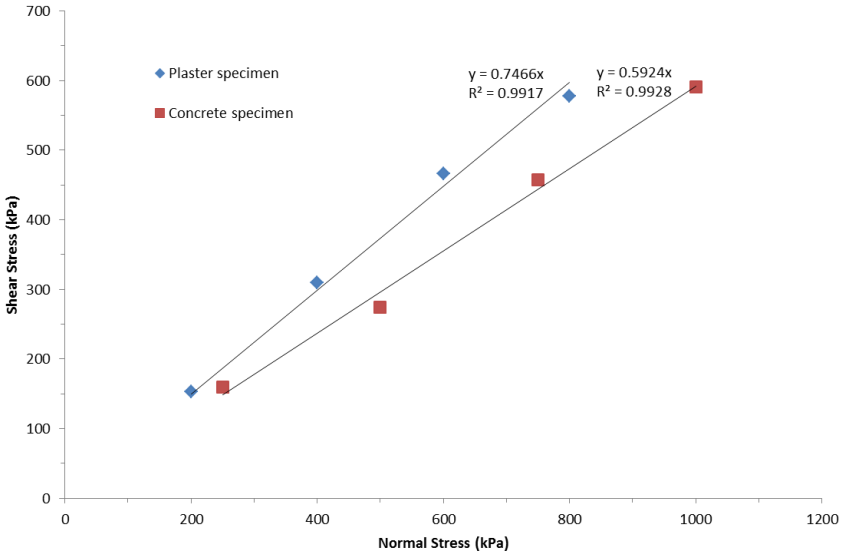

Figure 2-16 Direct Shear Behavior of Concrete and Plaster Planar Joint

Table 2-4 Shear Properties of the Planar Joint

	Friction angle of the planar joint, degree	Mohr-Coulomb Shear Strength
Plaster joint	36.7	$\tau = \sigma_n \tan 36.7^{\circ}$
Concrete joint	30.6	$\tau = \sigma_n \tan 30.6^{\circ}$

2.6 Conclusion

The results of material property test program were summarized in Table 2-5. The Coulomb Strength envelops were developed for concrete and plaster specimens respectively using *Rockdata* of *Rocscience*, as shown in Figure 2-17 and Figure 2-18.

Table 2-5 Properties of experimental samples

	Density kg/m^3	UCS and Standard Deviation MPa	Young's Modulus and Standard Deviation GPa	Poisson's ratio	Splitting Tensile Strength and Standard Deviation MPa	Internal Friction angle φ	Cohesion[1] c MPa	Friction angle of joints	Shear stiffness MPa/m
Concrete Sample	2203	41.98±6.29	5.72±1.42	0.32	4.386±0.38	54.2	6.81	30.6	316
Plaster Sample	1553	3.61±0.44	1.586±0.64	0.27	0.936±0.02	36.7	0.91	36.7	135

Note:

1 Internal friction angle and Cohesions were calculated according to the equations:

$$c = \frac{UCS(1-\sin\varphi)}{2\cos\varphi} \text{ and } \sigma_T = \frac{2c\cos\varphi}{1+\sin\varphi}$$

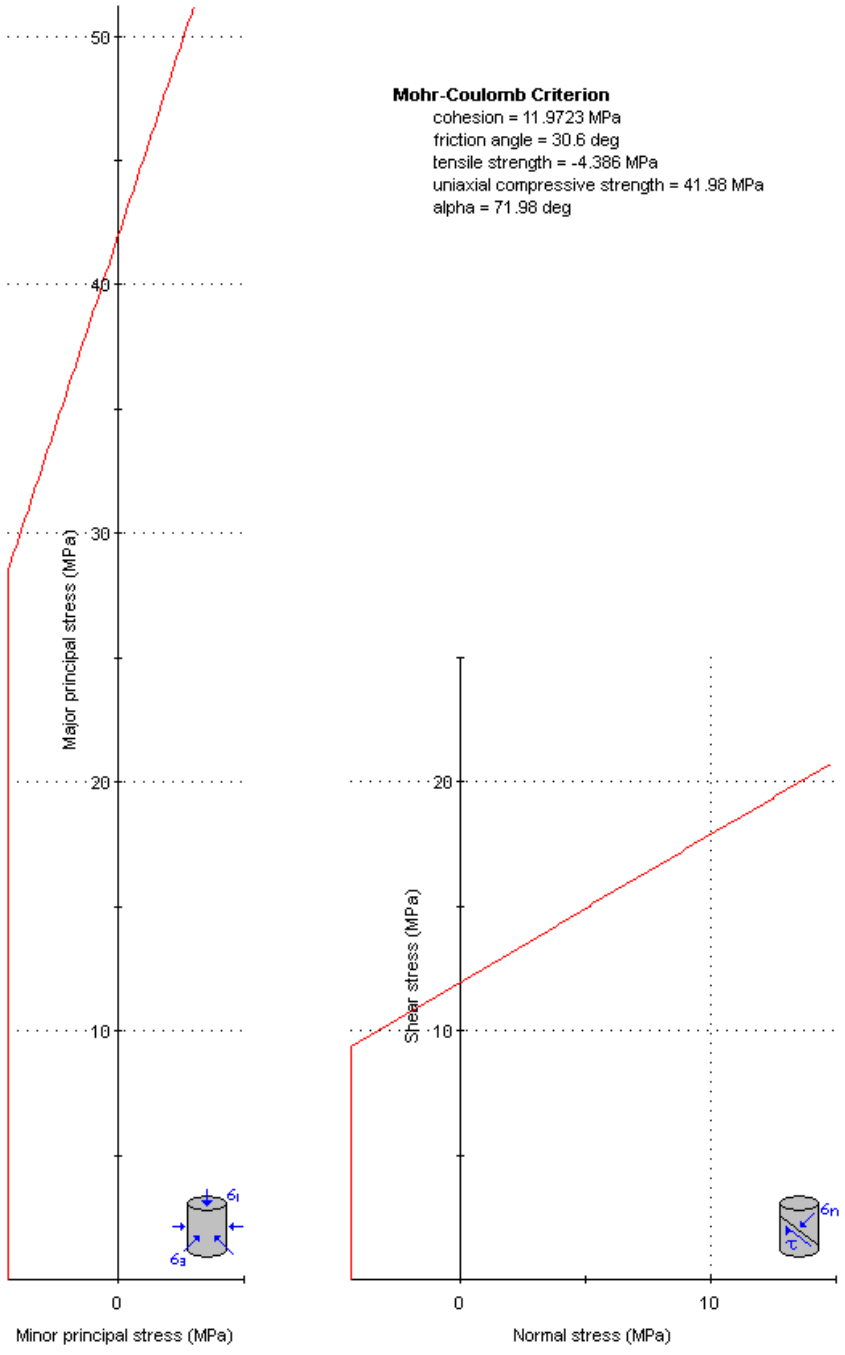

Figure 2-17 Concrete specimen Coulomb strength envelopes with a tensile cut-off in terms of principal stresses (left) and shear and normal stresses (right)

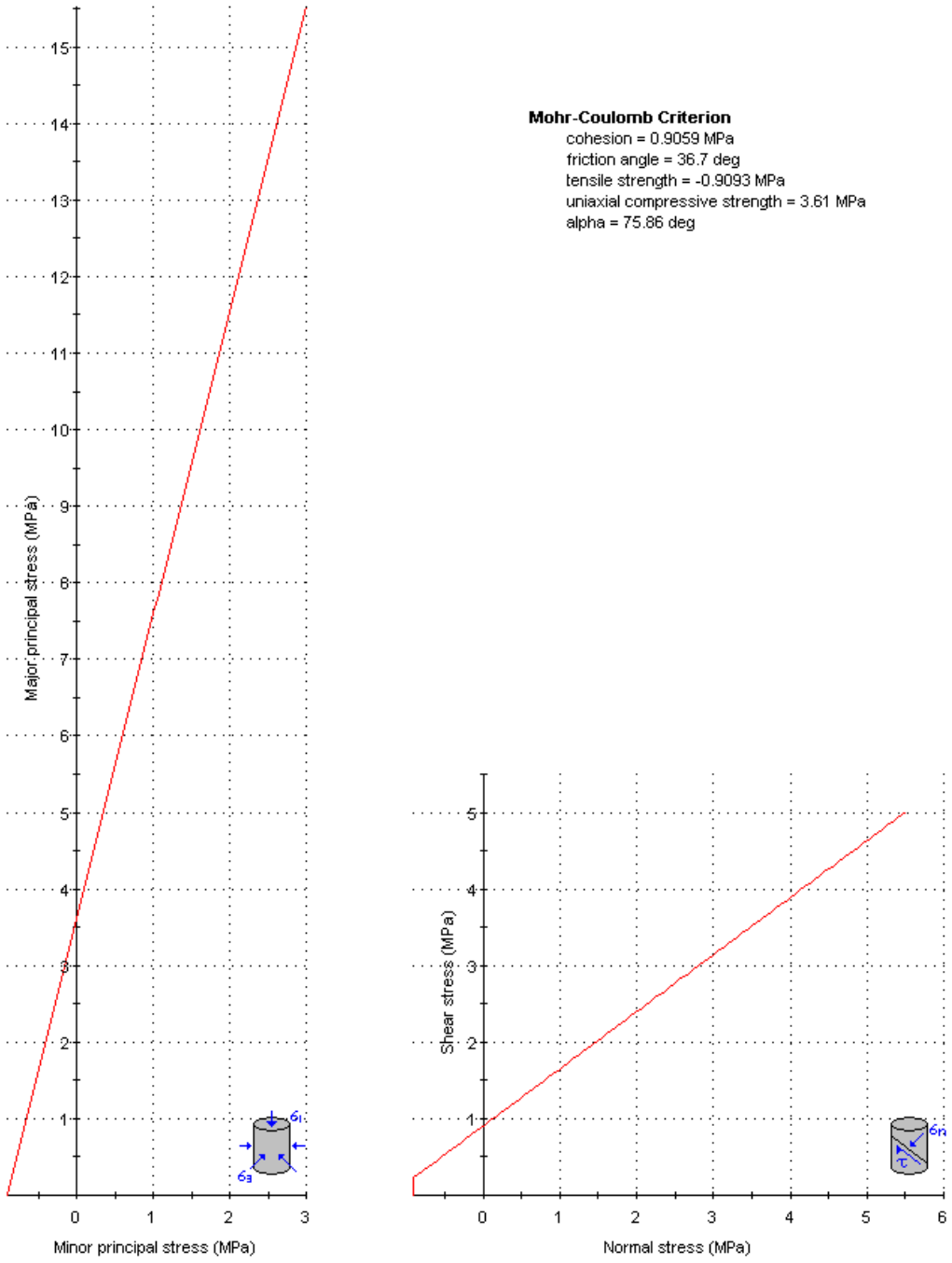

Figure 2-18 Plaster specimen Coulomb strength envelopes with a tensile cut-off in terms of principal stresses (left) and shear and normal stresses (right)

References

ASTM C496/C496M - 11 Standard Test Method for Splitting Tensile Strength of Cylindrical Concrete Specimens, (2011).

ASTM C192/C192M - 15 Standard Practices for Making and Curing Concrete Test Specimens in the Laboratory, (2015a).

ASTM C39/C39M - 15a Standard Test Method for Compressive Strength of Cylindrical Concrete Specimens. (2015).

Cho, N. (2008). Discrete element modeling of rock pre-peak fracturing and dilation (Doctor of Philosophy). Available from ProQuest Dissertations Publishing.

Cui, Y. (2012). Direct shear failure of a synthetic rock containing discontinuous joints (M.S.). Available from Dissertations & Theses @ University of Alberta. (1173644778).

3 Physical Investigation on the Behavior of Voussoir Beams[1]

3.1 Introduction

Stratified rock masses are often encountered in underground excavations. The stratified roof is usually cut by discontinuities. The discontinuities could be joints or faults which existed before the excavation or the appearance of tensile fractures caused by the excavation. The stratified roof should therefore be treated as jointed beams rather than intact, elastic beams. It is widely accepted that the self-support ability of jointed beams develops from the compression arch formed within the beam under transverse loading. Voussoir beam theory is a method for assessing the stability of a stratified roof based on the arching mechanism, as shown in Figure 3-1. Voussoir beam theory has been applied widely in the design and stability analysis of underground excavations. For example, it has been used for back-analyzing the failure of a mining roof (Alejano, Taboada, Garcia-Bastante, & Rodriguez, 2008), assessing the stability of an underground memorial site (Hutchinson et al., 2008), controlling the strata behavior in an underground long-wall mining face (Ju & Xu, 2013), and analyzing the roof collapse after the extraction of a coal pillar (Please et al., 2013).

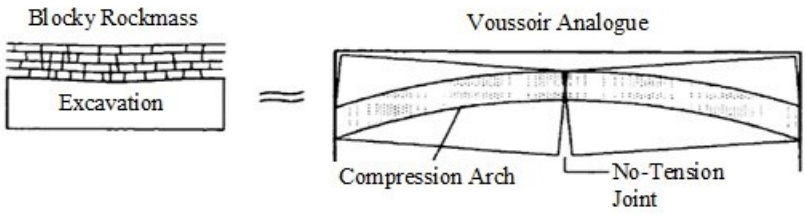

Figure 3-1 Voussoir beam analogy (M. S. Diederichs, 2000)

1 The content of this chapter has been prepared and submitted as a journal manuscript: Hu, C; Apel, D; Sudak, L; Szymanski, J; Liu, W. V. (2016) Physical Investigation on the Behavior of Voussoir Beams. *International Journal of Rock Mechanics and Mining Sciences (Submitted)*

The first analytical approach to describe the deformations of cracked roof beds was made by Evans (Evans, 1941). His analysis considers that cracks are created at the abutment and midspan of the rock beam. He assumes that the stress distributions induced at the abutments and midspan are triangular in shape and extend an equal distance, *nt*, over the depth of the beam. Furthermore, he makes an arbitrary assumption that $n=0.5$, i.e. the depth of induced stress equal to half of the thickness of the beam. The design procedure proposed by Evans was later modified by Beer and Meek (Beer & Meek, 1982). Subsequently, Sofianos (Sofianos, 1996) and then Diederichs and Kaiser (M. Diederichs & Kaiser, 1999b) noted some limitations in a simplified version of Beer and Meek's method and proposed alternative ways of addressing the static indeterminacy of roof-bed analysis. Diederichs and Kaiser (M. Diederichs & Kaiser, 1999b) proposed an algorithm to test the stability of a voussoir beam against snap-through and crushing based on the assumption that there will be the same linear stress at the abutment and midspan. This procedure is accepted by Brady and Brown (Brady & Brown, 2004), which proposed that the distribution of horizontal stress at the center of the arch is parabolic and presented a new formula to determine the deflection of the arch.

Wright (Wright, 1974) performed physical and finite element modeling to simulate cracked roof beams using limestone blocks and masonry bricks. From these results, he derived equations describing the thrust, the deflection, and the maximum stress generated by the beam. In addition to considering beams with cracks only at the abutment and midspan, he examined the effects of having multiple cracks throughout the beam. He showed that the worst case of a cracked beam, causing maximum stress concentration, is a beam that is cracked at the abutments and midspan only. Furthermore, Wright's results indicate that the assumptions made in Evans's approach, $n=0.5$ and the extent of the compression zones (*nt*) were the same at the abutments and midspan,

were incorrect. His results also indicate that the shape of the stress distributions acting at the abutments and midspan are not triangular; however, the stress distributions do seem to approach a triangular shape in beams with high span-to-depth ratios.

Sterling (Sterling, 1977) carried out both analytical and experimental analysis of voussoir beams. His analytical work involved examining six different shapes for the stress distribution acting upon the abutments and midspan. In all the cases, he assumed that the depth of stress distribution at abutment equal to it at midspan, i.e. $n=N$. Based on laboratory testing of a model of cracked beams, Sterling concluded that the assumption of a rectangular stress distribution agreed more closely with his experimental results.

Stimpson et al. (Stimpson & Ahmed, 1992) conducted physical testing on thick intact rock beams (i.e., the beams were not fractured) of limestone, granite and potash with span/depth ratios less than 5. These physical tests revealed a progressive failure mechanism dominated by tensile fracturing. This failure mechanism is characterized by three distinct stages. Stage I, the primary beam stage, terminates with the initiation of tensile cracking in the lower fibers at the midspan. This stage also marks the initiation of linear arching. As loading continues following midspan cracking, two diagonal cracks initiate and propagate very rapidly towards each abutment. Their development marks the end of stage II. Continued loading beyond the stage of diagonal cracking marks stage III. This stage is characterized by the ultimate failure of the rock beam which occurs either by the shearing of the rock above the diagonal crack or shearing along the diagonal crack. This shear failure mode, in the author's opinion, is caused by the large axial forces developed in the arch, which cause the shear strength of the rock to be exceeded. Stimpson also conducted a discrete crack propagation finite element analysis for a typical intact rock beam. The results validated the progressive failure mechanism observed in the laboratory testing.

Mottahed et al. (Mottahed & Ran, 1995) performed both physical and finite element testing. The physical tests involved voussoir beams cut from two types of Durox bricks of lightweight concrete. Because the lightweight concrete has low values of Young's modulus and compressive strength, the model beams failed at low transverse loads so that the horizontal movement of both abutments was negligible; therefore, the abutments were assumed to be rigid. This assumption, under which the tests were conducted, is valid; however, in reality, some small abutment movement occurs. Under the experimental conditions, almost all the model voussoir beams failed by crushing at the high stress areas located at the ends and at the midspan. The finite element approach considered triangular stress distributions acting at the midspan and abutments, and the depth of these distributions were assumed to be equal on both sides, i.e. $n=N$. The results showed that a linear analysis of the structure is inappropriate for describing the beam behaviour. Based on these conclusions, equations were therefore derived for the thrust, lever arm, centroid location, and crushing strength using non-linear analysis.

Talesnick et al. (Talesnick et al., 2007) studied the behavior of voussoir beams comprised of 6 plaster blocks using a centrifuge. Voussoir beam models of two different geometries were investigated. While both have the same length and width, one has half the thickness of the other. Displacements at the ends of each block were monitored by 12 LVDTs (Linear Variable Differential Transformer), and three pairs of strain gauges were used to measure the strain developed at the top, middle, and bottom of one of the blocks. Thrust was monitored by a load cell at the end. The model was subjected to accelerations of up to 90g. It was found that small rotation and displacement of the block near the abutment were required in order to set up a stable linear arch. Based on the two models tested, the thrust developed is independent of beam

thickness. The depth of the strain distribution ranges from the whole thickness of the beam near the abutment to half of the beam thickness near the midspan.

Yang et al. (Yang & Shang, 2007) modelled the voussoir beam using plaster blocks. Stress sensor was used to monitor the horizontal thrust during the test, and the initial constraining stress was applied by tightening the nut and measured by stress sensor as well. The span/depth ratio and the initial constraining stress was found to affect the behavior of the moment arm and the horizontal stress in the voussoir beam. The stress distribution was not investigated.

Based on the above literature review, a number of questions emerge with respect to assumptions about the stress distribution size and shape that lead to incompatibilities between results obtained by different investigators. All the analyses, except for Sterling's, assume triangular-shaped stress distributions of equal size acting at the abutment and midspan. Sterling dealt with six different stress distribution shapes, of which the rectangular-shaped stress block, which had equal depth at the abutment and midspan, gave the best fit to his experimental data. Nevertheless, Wright's results indicate that Sterling's finding in this case was incorrect. His results indicated that the induced lateral stresses, developed at the abutments and midspan, increase in a non-linear manner and that the depths over which they act are not equal. Mottahed et al. (Mottahed & Ran, 1995) does not identify where crushing first occurred. The author believes crushing occurs first at the abutments, because, as the beam deflects, the compressive stresses that are generated are being concentrated more at the ends than at the center. Consequently, the maximum stress generated at the ends is greater than that at the center.

In reality, the stress distribution along the boundary is not necessarily linear, and experimental studies are necessary to determine its exact geometry (Tsesarsky & Talesnick, 2007). Based on

the review of the experimental investigations, no test results were able to give the stress distributions at the abutments and midspan as either the beam tested was an intact beam or the instruments used were limited. In this paper, a series of 2-block voussoir beams will be tested. The deflection and strain distributions at midspan and abutment will be measured by Vic-3D digital image correlation system.

3.2 Physical Investigation

A series of tests is performed to investigate the behavior of a two-block voussoir beam under transverse loading; two of the tests are explained in detail below. The objectives of this series of tests are: (1) to investigate the behavior of voussoir beams; (2) to calibrate the numerical model for further investigation using the results from these tests.

3.2.1 Testing Apparatus

The testing apparatus consists of a constraining frame, loading system, and Vic-3D correlation system which will be discussed in detail in the following sections.

3.2.1.1 Constraining frame

The constraining frame consists of two end-plates of 25mm thickness, which are connected via 4 screwed rods of 30mm, as shown in Figure 3-2. The vertical supports of the two abutment blocks are two limestone blocks.

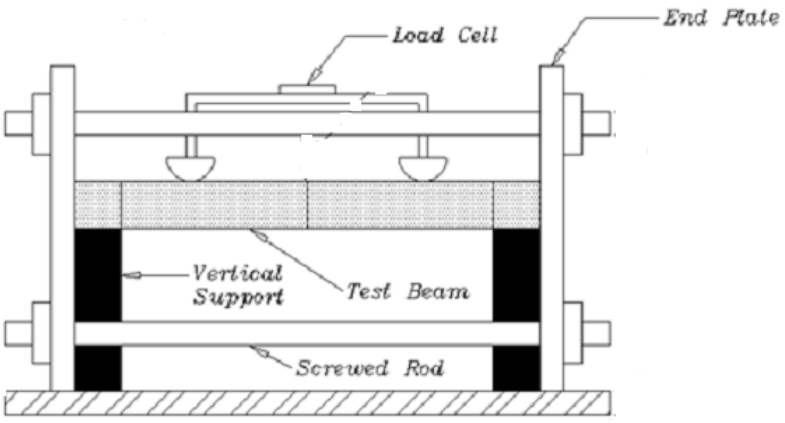

Figure 3-2 Constraining frame

3.2.1.2 The loading system

The load was applied by a servo-controlled loading frame, and a two-point load-spreading system was used, as shown in Figure 3-3.

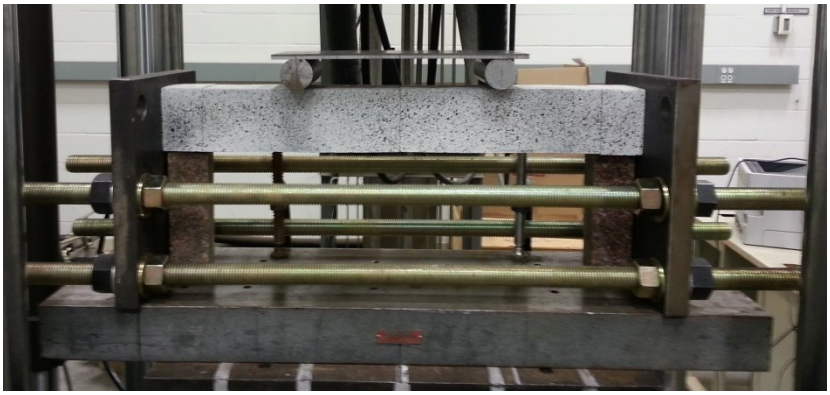

Figure 3-3 The two-point load-spreading system

3.2.1.3 Vic-3D correlation system

The displacement and deformation on the beam surface were measured by the Vic-3D correlation system, as shown in Figure 3-4. Photogrammetric analysis provides insights into the response of the rock mass during the application of transverse loading and assists in identifying the failure path that occurred.

The Vic-3D correlation system tracks the deformation of the subset, shown in Figure 3-5. Only information at the center of the subset will be outputted after processing. In these tests, subset size suggested by the software is 35*35 pixels. The cameras used have a resolution of 2048*2048 pixels.

In typical setups, the Vic-3D correlation system can see an in-plane displacement accuracy of 1/50,000 of the field of view. This means that, if a 1-meter area is imaged, a 20-micron motion can be detected (*Vic-3D 2010 reference manual*2010).

As stated in the literature review, either strain gages or LVDTs were used to track displacement at several points. The Vic-3D correlation used in the test, the displacement in the whole surface can be monitored. Then the strain distribution at the joint of voussoir beam can be measured.

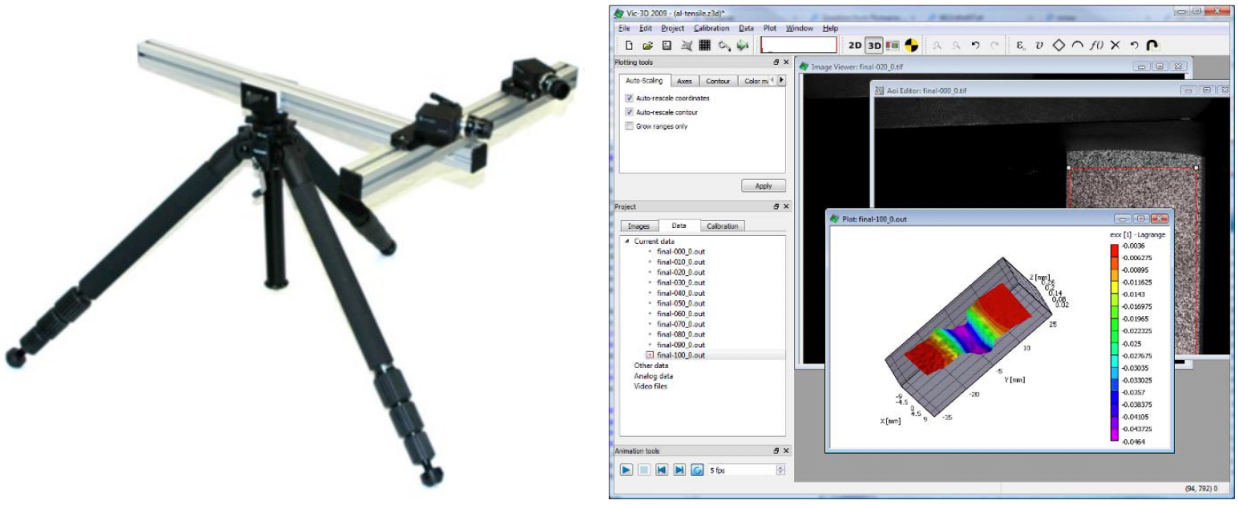

Figure 3-4 Vic-3D correlation system, the cameras (left) and the image processing software Vic-3D (right)

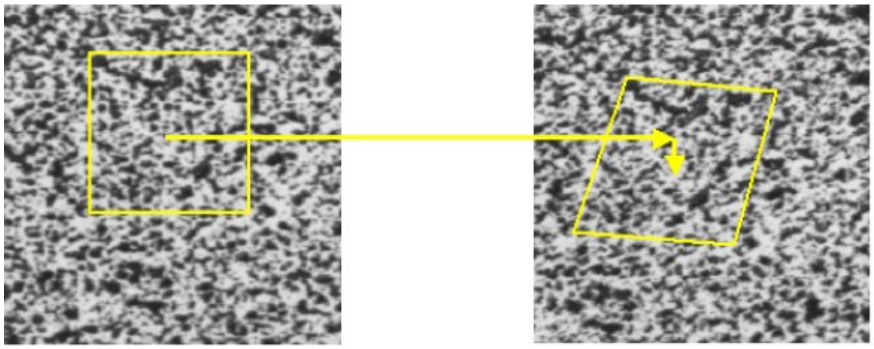

Figure 3-5 Undeformed and deformed image with subset

The final set-up is shown in Figure 3-6.

Figure 3-6 Experiment Set-up

3.2.2 Beam Specimen

Concrete and plaster specimens were made for the tests, as shown in Figure 3-7.

Figure 3-7 Plaster beam (left) and concrete beams (right)

The properties of the plaster and concrete samples are detailed in Table 3-1. The Poisson's ratio may be less accurate than other parameters because the instrument for transverse displacement measurement slightly pierced into the cylinder samples during test.

Table 3-1 Properties of experimental samples

	Density	Uniaxial Compressive	Splitting Tensile	Young's Modulus	Poisson's ratio

	kg/m^3	Strength MPa	Strength Mpa	Gpa	
Concrete Sample (after 28 days of curing)	2203	41.98	4.386	5.72	0.32
Plaster Sample	1553	3.61	0.936	1.586	0.27

In order to be tracked by the Vic-3D correlation system, the front surface of the beam is painted with black speckles on a white background (see Figure 3-8).

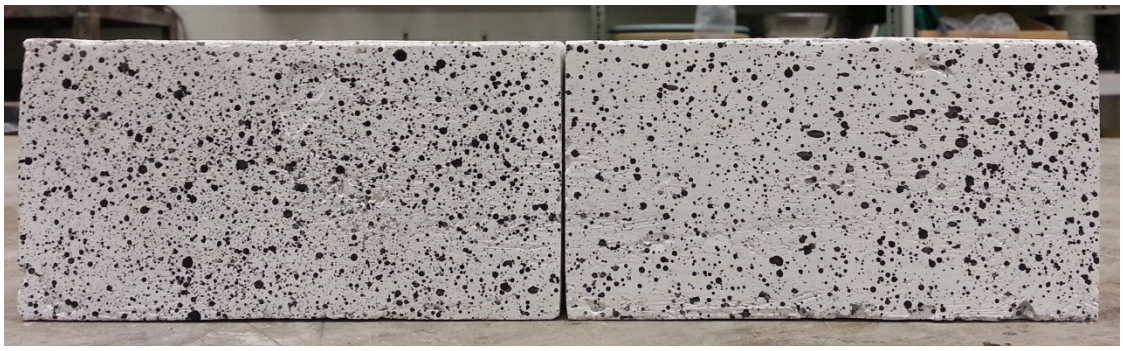

Figure 3-8 Two-block voussoir beam consisting of painted plaster samples

All of the tests performed are summarized in

Table 3-2.

Table 3-2 Summary of the Tests Conducted

No.	Type	Size of Beam/mm			Span / Depth	Size of End blocks/mm			Loading rate mm/min	Frequency of camera shooting sec./picture	Note
		Span	Depth	Wide		Length	Depth	Wide			
1	concrete	488	77	76	6.3	50	77	76	0. 5	5	no initial stress, finger tight
2	concrete	488	77	76	6.3	50	77	76	0.5	5	initial stress applied, no end supporting block; slide
3	concrete	488	77	76	6.3	50	77	76	0.5	8	slide at left end
4	concrete	488	77	76	6.3	50	77	76	0.5	8	slide
5	concrete	292	77	76	3.8	60	77	76	0.5	8	initial stress applied, slide
6	concrete	292	77	76	3.8	60	77	76	0.5	8	slide with initial stress
7	concrete	292	77	76	3.8	60	77	76	0.5	8	finger tight, slide
8	plaster	488	77	76	6.3	50	77	76	0.5	8	no initial stress
9	plaster	484	77	76	6.3	60	77	76	0.5	8	initial stress applied
10	plaster	296	77	76	3.8	60	77	76	0.5	8	initial stress applied

3.2.3 Typical Behaviour of Voussoir Beam Test

The No.1 Concrete and No. 8 Plaster in

Table 3-2 were selected to describe the behavior of a concrete voussoir beam and a plaster voussoir beam respectively during the test.

3.2.3.1 Typical Behavior of Concrete Voussoir Beams

1) Load – Deflection Relationship

Four points on the beam's front surface were selected to monitor the displacement of the beam (see Figure 3-9). To detect sliding at abutment, points *P0* and *P3* were selected. These will detect the slide at both sides of the voussoir beam near the abutments. The deflection at the centre was measured at points *P1* and *P2*, located at the left block and right block near the centre, respectively.

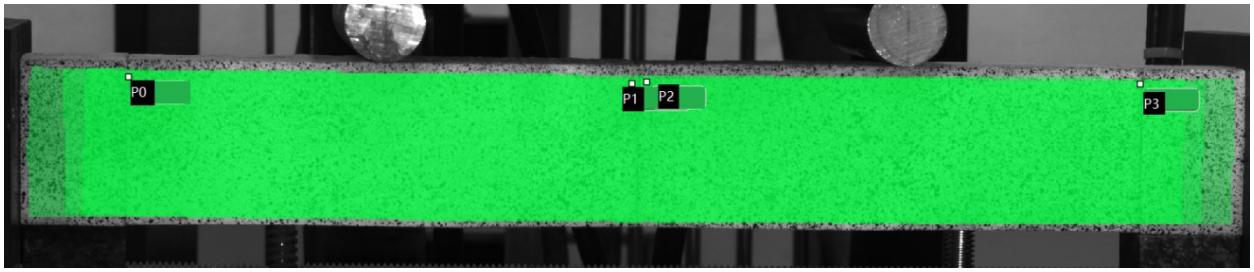

Figure 3-9 Four Points Selected to Monitor the Deflection of Concrete 1

The load-deflection relationship is shown in Figure 3-10. The load was applied by the MTS loading frame controlled in specified speed of 0.5mm/min. Five deflections are presented. The load – MTS deflection gives the full failure path of voussoir beam tested. As the tracking of monitoring points was lost after large deformation happened, the other four deflections didn't cover the whole failure path. The load – p1 and p2 average deflection gives the relationship between the load and the defection at the center of voussoir beam. The load – p0 and p3 average defection gives the relationship between the load and slide induced at the abutment. The relationships between the load and deflection of MTS and deflection at center of voussoir beam with slide deducted were presented as well.

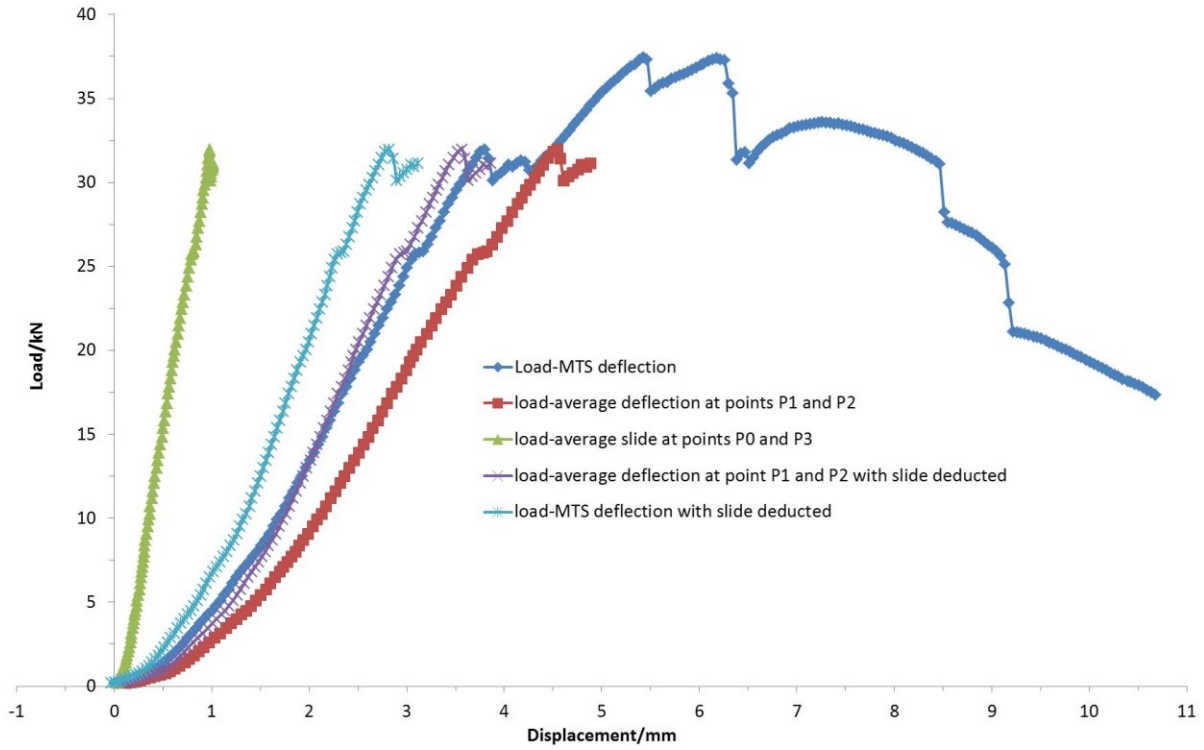

Figure 3-10 Load–Deflection Relationship for Concrete 1

2) Stress Distributions at the midspan and abutment

In the linear range for Load-Deflection of the beam behavior, two images were selected for analyzing the stress distributions at the abutment and midspan of the voussoir model under transverse load. The parameters of the images are presented in Table 3-3.

Table 3-3 Characteristics of the Two Images Selected

Image Index	Load/kN	MTS displacement/mm	Average deflection at point P1 and P2 with slide deducted/mm
Concrete1-033	2.05	0.6323	0.5273
Concrete1-040	4.01	0.9256	0.8140

Two lines, *L0* and *L1*, were drawn at the abutment and midspan, respectively, to extract the strain along the two lines, as shown in Figure 3-11.

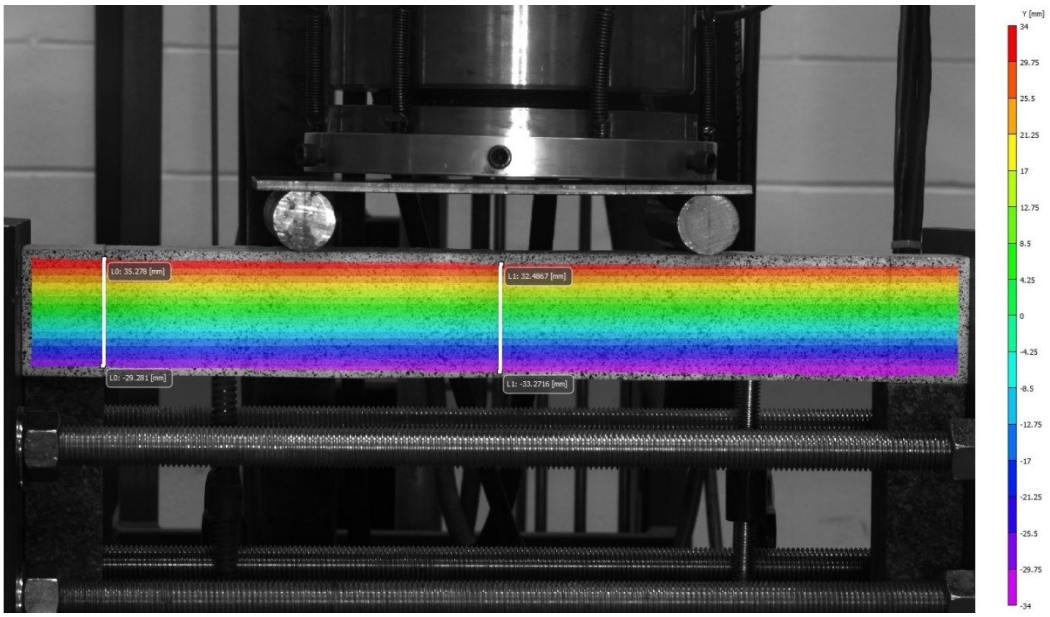

Figure 3-11 Two lines drawn at the abutment and midspan for Strain Extraction of Concrete 1

It is observed that the area near the edges of the front surface is not covered by the contour in Figure 3-11. This is a result of the principles of Vic-3D image correlation and also the limitations of camera resolution. The depth of the uncovered area is nearly 5mm from the horizontal edges, which is around 7% of the depth of the front surface of the beam. This makes the deformation at the very top and very bottom of the beam unknown. This lost area is of high interest. At this stage, the strain of this area was approximated by the trend line.

The positive strain is tension, and the negative strain is compression. The positive stress is compression.

a) Image Concrete 1-033

The contour of the horizontal strain ε_{xx} is shown in Figure 3-12.

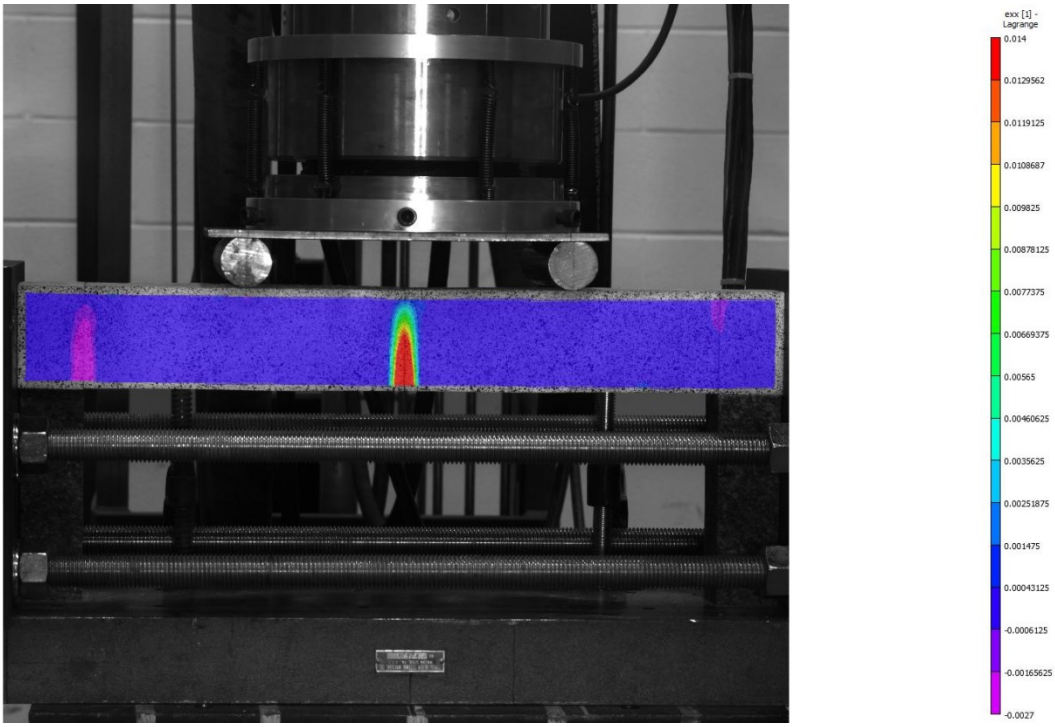

Figure 3-12 Strain ε_{xx} contour of the Image Concrete1-033

As the deformation at the very top and very bottom of the surface is unknown, a fitting method is used to find the strain distribution in this area.

The strain measured along line *L1* at the midspan is shown in Figure 3-13.

There is a linear relationship between the strain and the beam thickness at the upper part of the beam, as shown in following equation:

$$\varepsilon_{xx} = -0.0454y + 3.2163 \quad \text{when } y > 45, \text{ with } R^2 = 1 \qquad \text{Equation 3-1}$$

Where the ε_{xx} is the horizontal strain in percent (%), and y is the coordinate of vertical axis, with 0 at the beam bottom.

The graph of above equation is shown in Figure 3-13.

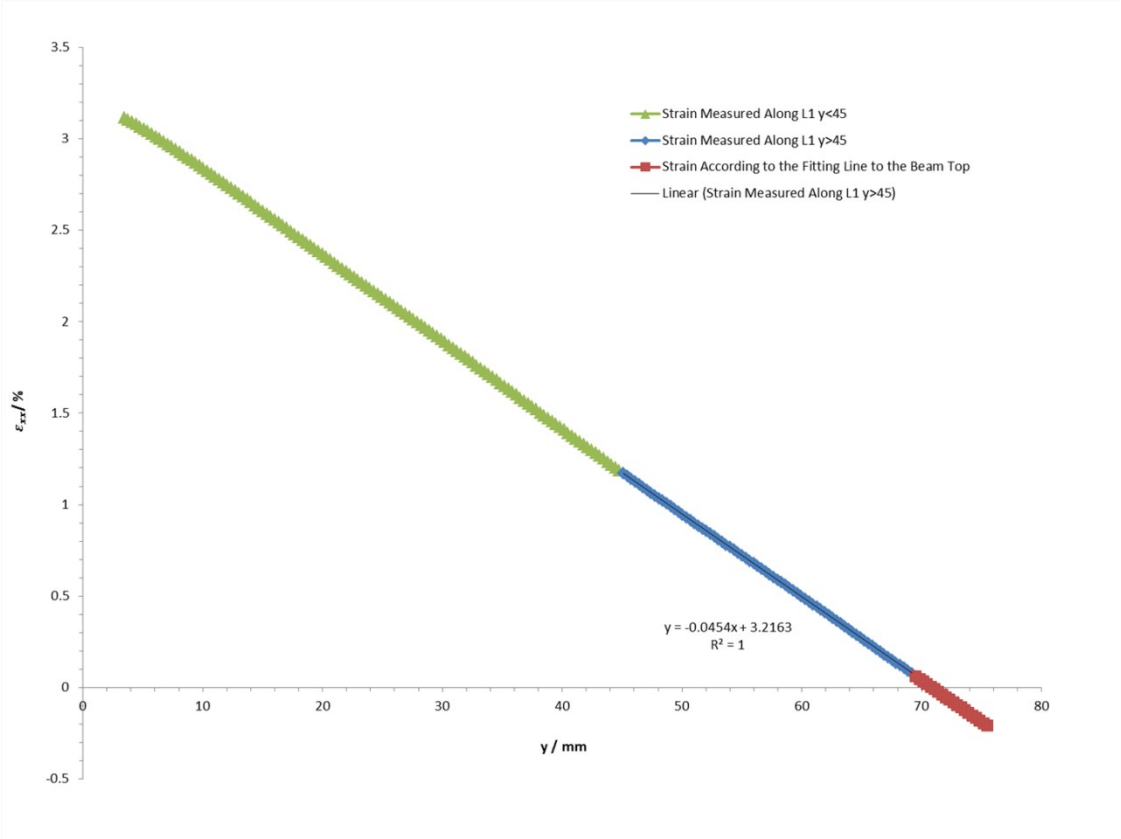

Figure 3-13 Strain along the line *L1* at the midspan of Image Concrete1-033

Figure 3-13 shows the strain is in compression when $y > 70.84$, and the thickness of the beam or the length of line $L1$ is

$$t = 75.48 \qquad \text{Equation 3-2}$$

Therefore the ratio of the compression zone depth to the beam thickness at the midspan is

$$N = 0.0614 \qquad \text{Equation 3-3}$$

From the compressive strain in Figure 3-13 and the Young's modulus of the concrete sample in Table 3-1, the compressive stress at the midspan is calculated, as shown in Figure 3-14. From Equation 3-1, the equation for stress distribution along line $L1$ at the midspan is

$$\sigma_{xx} = 2.60y - 183.97 \quad \text{When } y > 45 \qquad \text{Equation 3-4}$$

Where σ_{xx} is horizontal stress in *MPa*, and y is in *mm*.

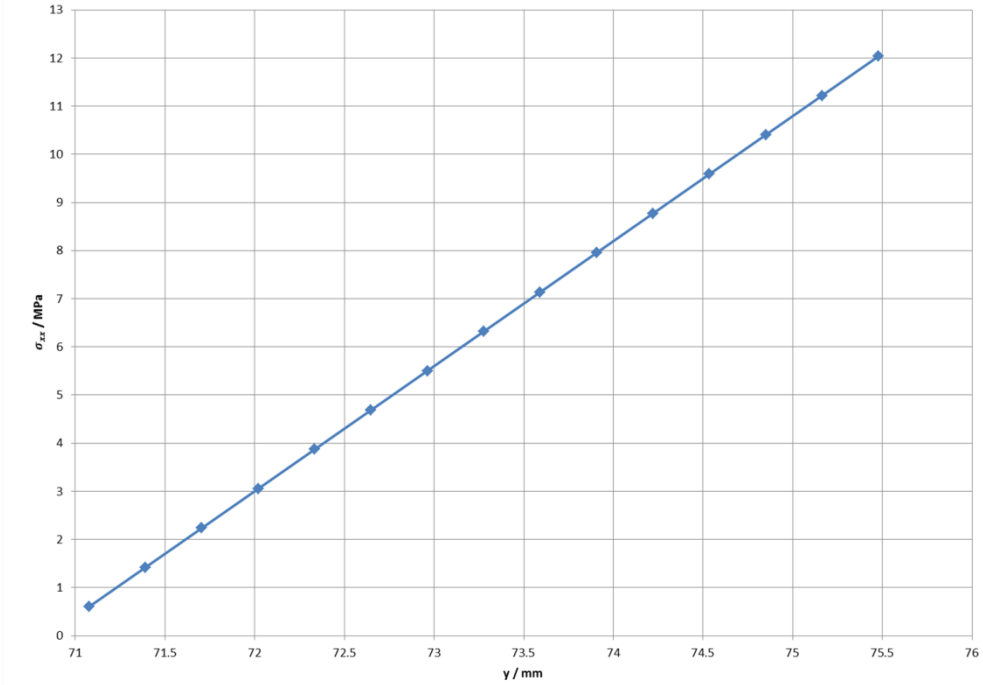

Figure 3-14 Compressive Stress Distribution along line *L1* at the Midspan of Image Concrete1-033

The strain measured along line *L0* at the abutment is shown in Figure 3-15.

When$y < 20$, the best fitting relationship between the strain and the beam thickness is

$$\varepsilon_{xx} = 0.00007y^2 + 0.008y - 0.638 \quad \text{When } y < 20, \text{ with } R^2 = 0.9999 \qquad \text{Equation 3-5}$$

The graph of the above equation is shown in Figure 3-15 too.

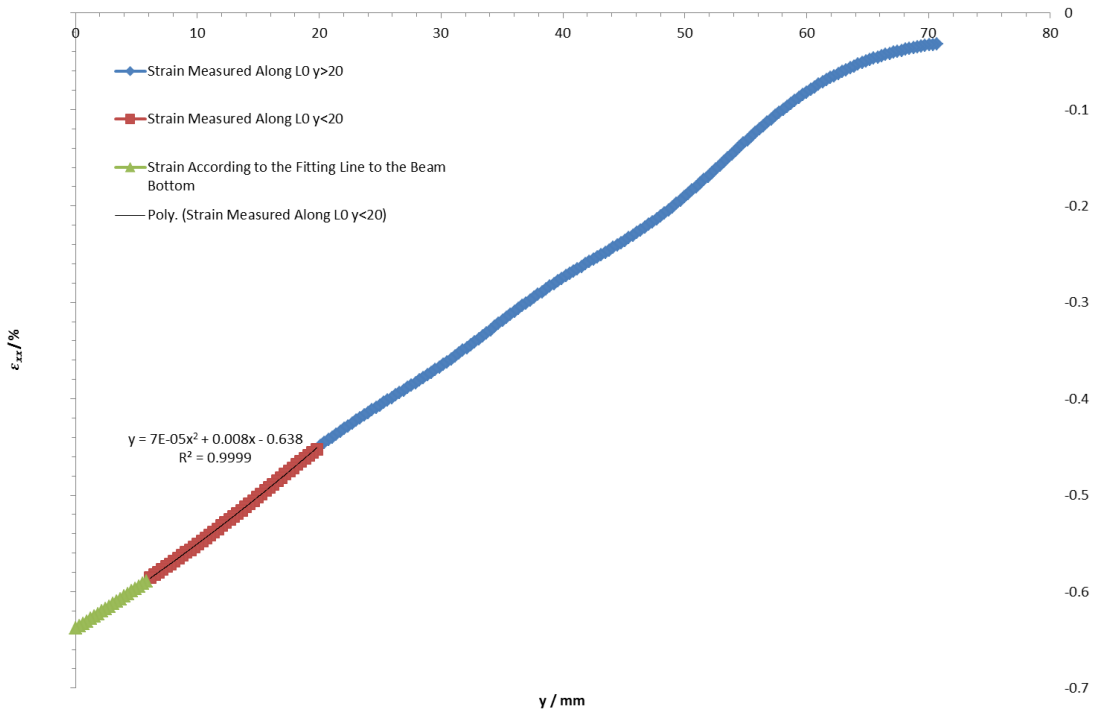

Figure 3-15 Strain along the line *L0* at the abutment of Image Concrete1-033

Figure 3-15 shows that the compression zone is extended over the whole depth of the beam. The ratio of the compression zone to the beam thickness at the abutment is 1, as shown in Equation 3-6. Further investigation is needed to determine whether this is a consequence of the experiment setup.

$$n = 1 \qquad \text{Equation 3-6}$$

The stress distribution at the abutment is shown in Figure 3-16.

Similarly, the stress distribution at the lower abutment is:

$$\sigma_{xx} = -0.004004y^2 - 0.4579 + 36.4936 \quad \text{When } y < 20 \qquad \text{Equation 3-7}$$

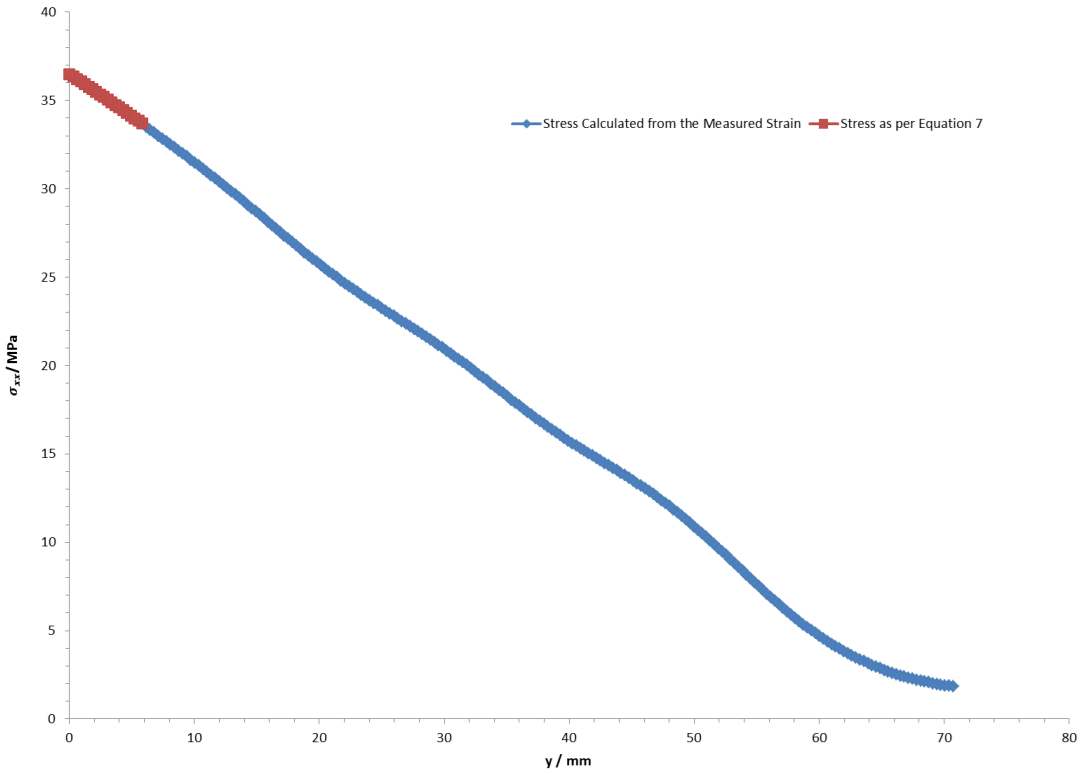

Figure 3-16 Stress Distribution at the abutment of Image Concrete1-033

b) Image Concrete 1-040

Similarly, the Image 1-040 was analysed in the same way as for Image 1-033. The contour of horizontal strain of Image Concrete 1-040 is shown in Figure 3-17. The strain along the midspan and abutment was extracted and presented in Figure 3-18 and Figure 3-20 respectively. With the Young's modulus known, the stress distribution along midspan and abutment was obtained and shown in Figure 3-19 and Figure 3-21 respectively.

The strain at upper midspan can be represented by the linear equation, Equation 3-8. And the strain at lower abutment can be represented by polynomial equation, Equation 3-12. The ratio of stress distributions to the total thickness of voussoir beam at midspan and abutment was obtained respectively, as shown in Equation 3-11 and Equation 3-15.

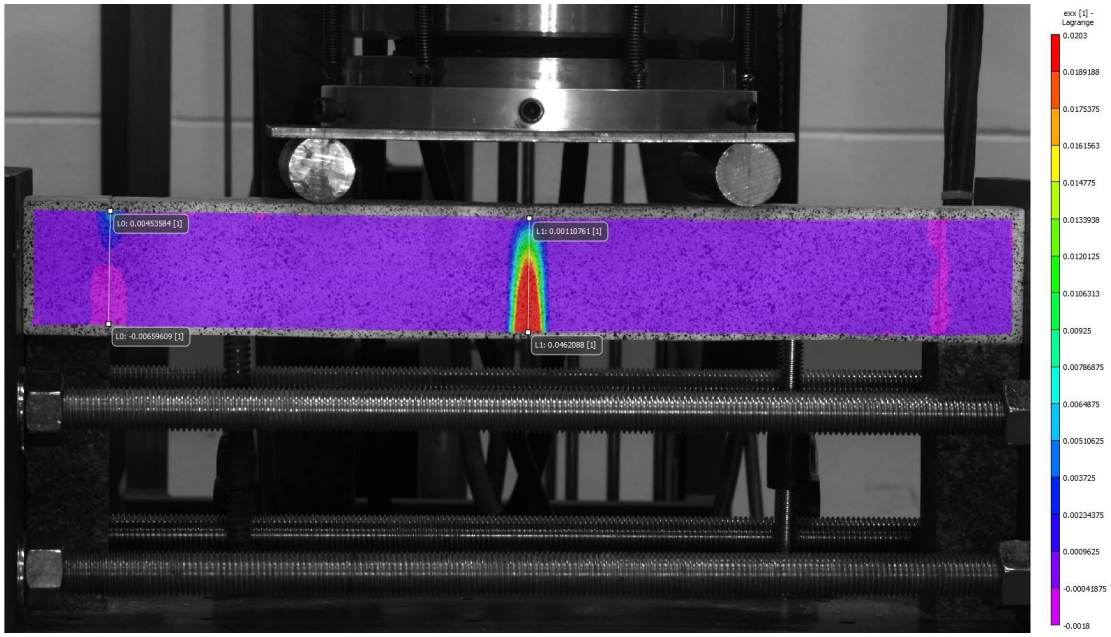

Figure 3-17 Horizontal Strain ε_{xx} Contour of the Image Concrete1-040

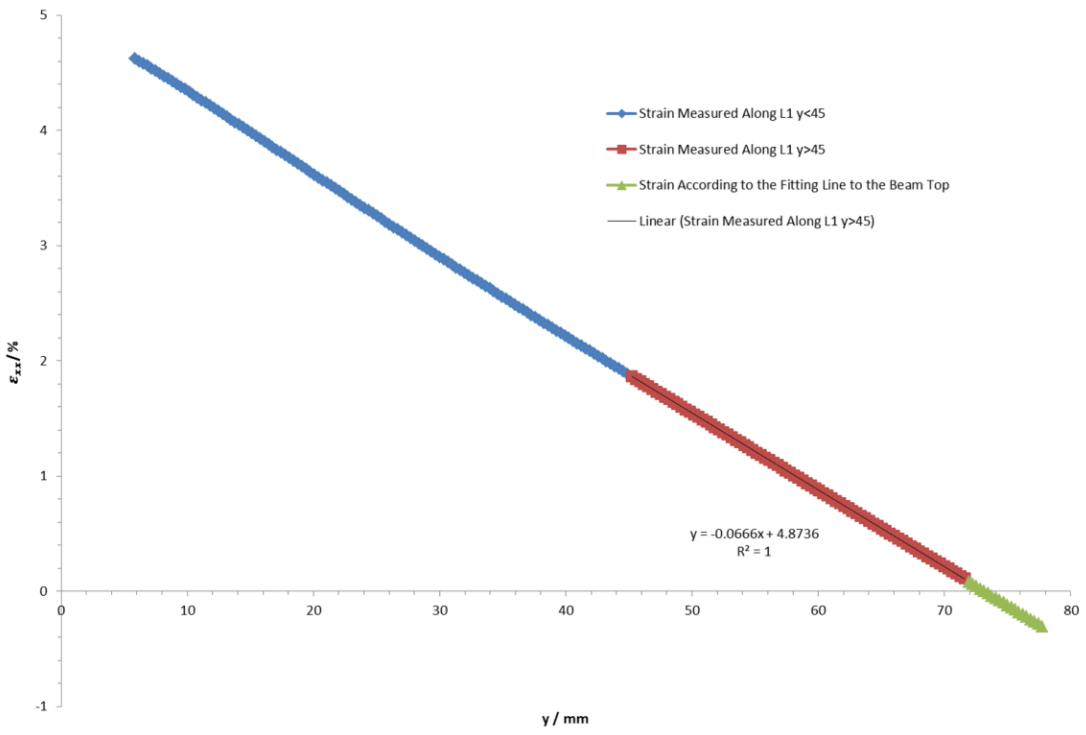

Figure 3-18 Strain along the line *L1* at the midspan of Image Concrete1-040

The strain along *L1* at the upper midspan:

$$\varepsilon_{xx} = -0.0666y + 4.8736 \quad \text{when } y > 45, \text{ with } R^2 = 1 \qquad \text{Equation 3-8}$$

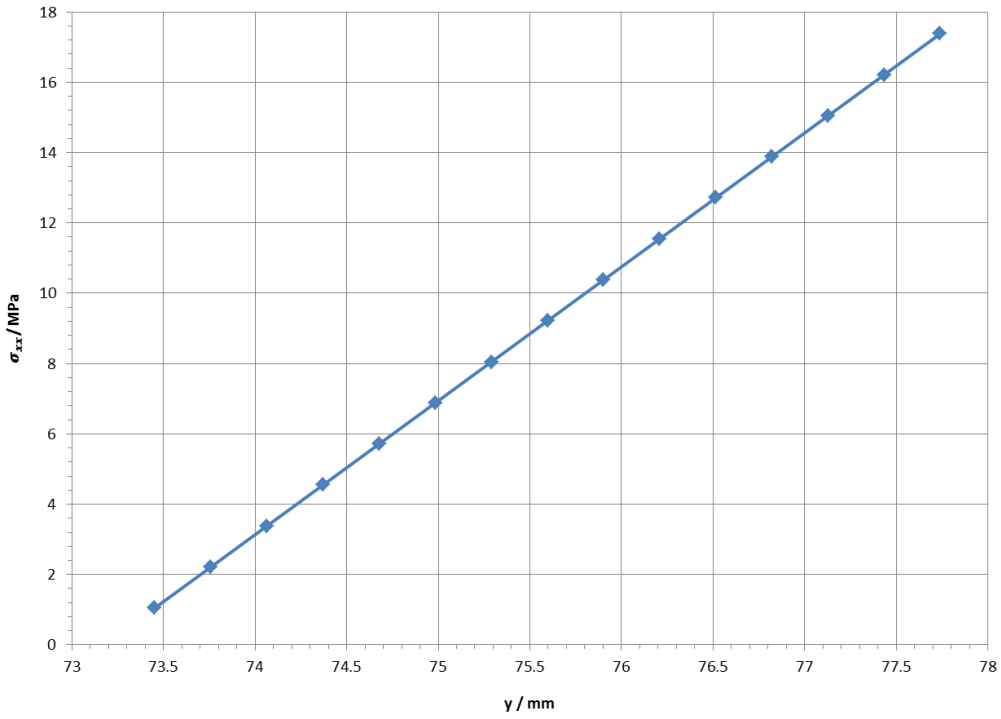

Figure 3-19 Compressive Stress along the line *L1* at the midspan of Image Concrete1-040

The stress along *L1* at the upper midspan:

$$\sigma_{xx} = 3.81y - 278.77 \quad \text{when } y > 45 \qquad \text{Equation 3-9}$$

$$t = 77.7386 \qquad \text{Equation 3-10}$$

$$N = 0.0586 \qquad \text{Equation 3-11}$$

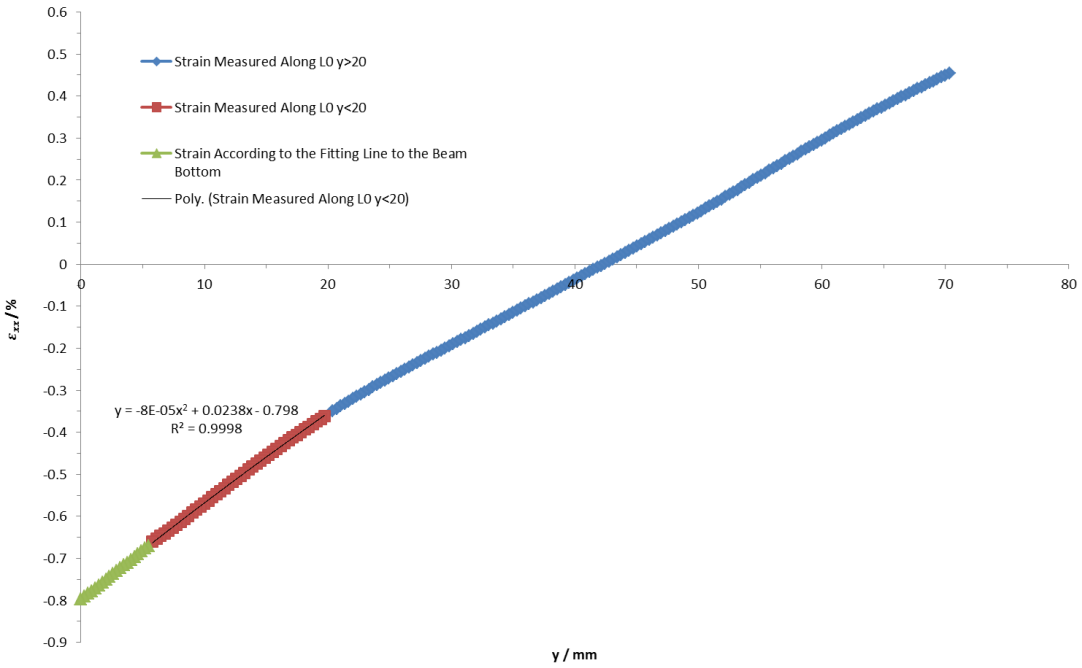

Figure 3-20 Strain along the line *L0* at the abutment of Image Concrete1-040

The strain along *L0* at the lower abutment:

$$\varepsilon_{xx} = -0.00008y^2 + 0.0238y - 0.798 \quad \text{when } y < 20, \text{ with } R^2 = 0.9998 \qquad \text{Equation 3-12}$$

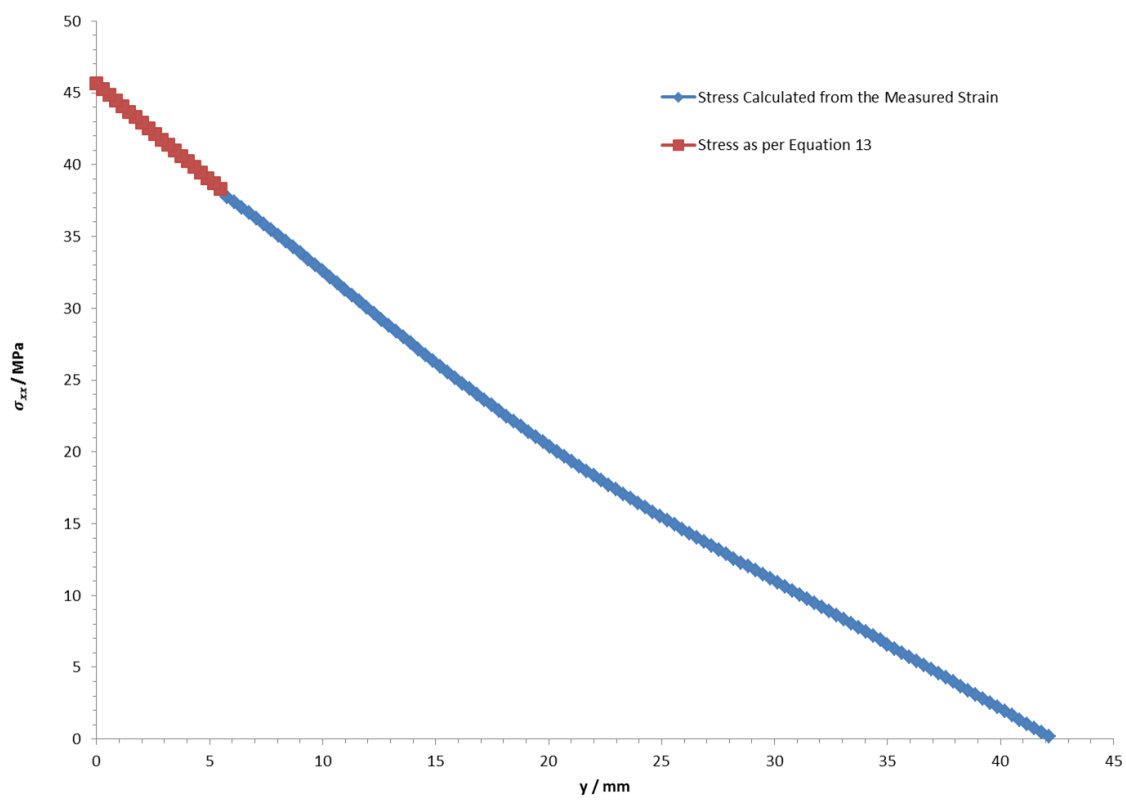

Figure 3-21 Stress Distribution along the line *L0* at the abutment of Image Concrete1-040

The stress along *L0* at the lower abutment:

$$\sigma_{xx} = 0.004576y^2 - 1.36136y + 45.6456 \quad \text{when } y < 20 \qquad \text{Equation 3-13}$$

$$t = 76.106 \qquad \text{Equation 3-14}$$

$$n = 0.5536 \qquad \text{Equation 3-15}$$

3.2.3.2 Typical Behaviour of Plaster Voussoir Beams

No. 8 Plaster in

Table 3-2 is selected to show the behavior of plaster voussoir beams.

The following analysis is similar to the one performed for the concrete voussoir beam above.

1) Load – Deflection Relationship

Similarly, four points were selected to track the displacement at abutment and midspan of the voussoir beam as shown in Figure 3-22. The load-displacement relationship was presented in Figure 3-23.

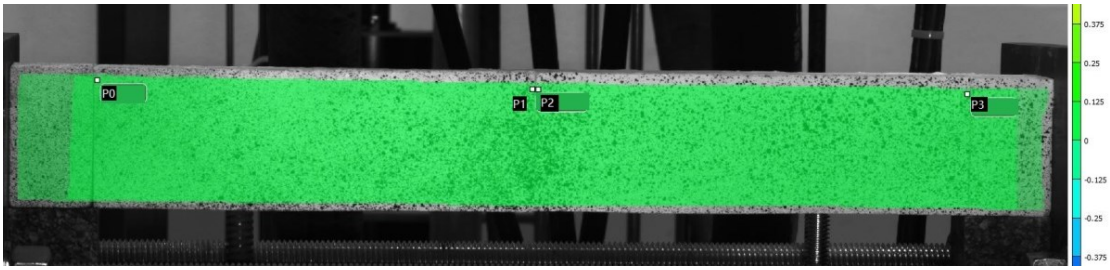

Figure 3-22 Four Points Selected to Monitor the Deflection of the Plaster 1

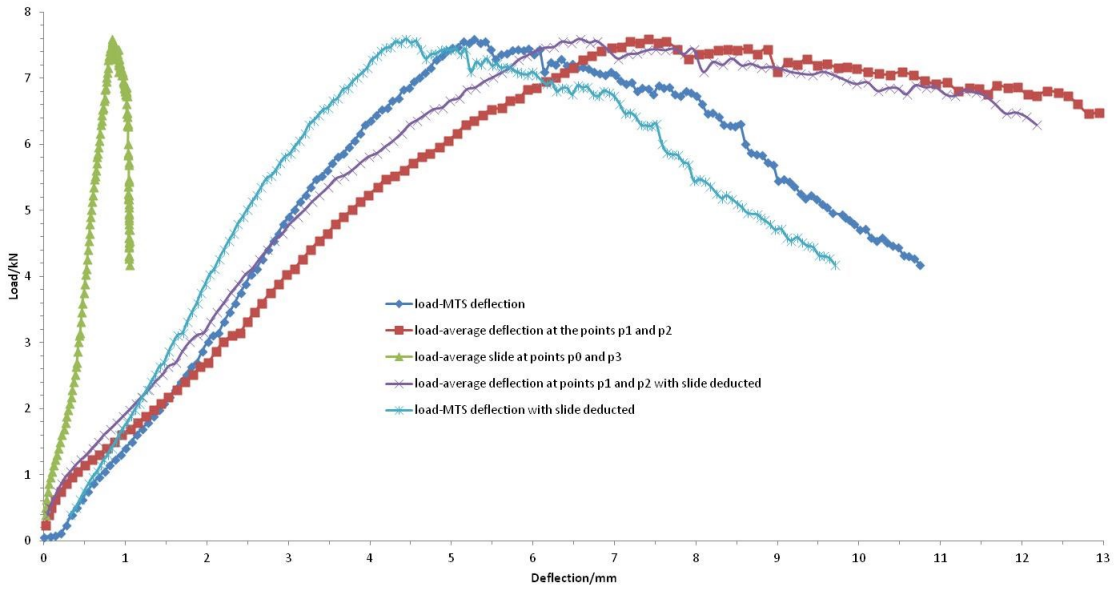

Figure 3-23 Load–Deflection Relationship for Plaster 1

2) Stress Distributions at the midspan and abutment

Within the linear range of load-deflection relationship, two images, Image Plaster 1-038 and Image Plaster 1-070 were selected to investigate the stress distribution characterises at midspan and abutment. The load and displacement of the two images are presented in Table 3-4.

Table 3-4 Characteristics of the Two Images Selected

Image Index	Load/kN	MTS displacement/mm	Average deflection at point P1 and P2 with slide deducted/mm
Plaster 1-038	1.404	1.0022	0.5912
Plaster 1-070	5.132	3.1389	3.291

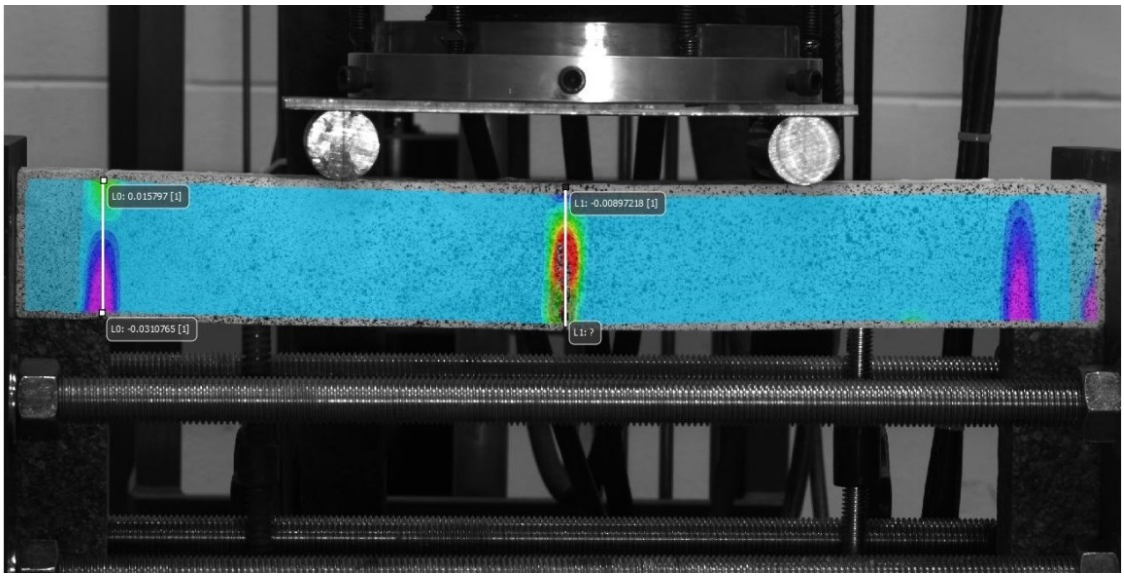

Figure 3-24 Two lines drawn at the abutment and midspan for Strain Extraction of Plaster 1

The two lines, *L1 and L0*, to extract the strain distribution at midspan and abutment are shown in Figure 3-24. This image is the contour of the horizontal strain of image Plaster 1-070.

a) Image Plaster 1-038

The contour of the horizontal strain ε_{xx} is shown in Figure 3-25.

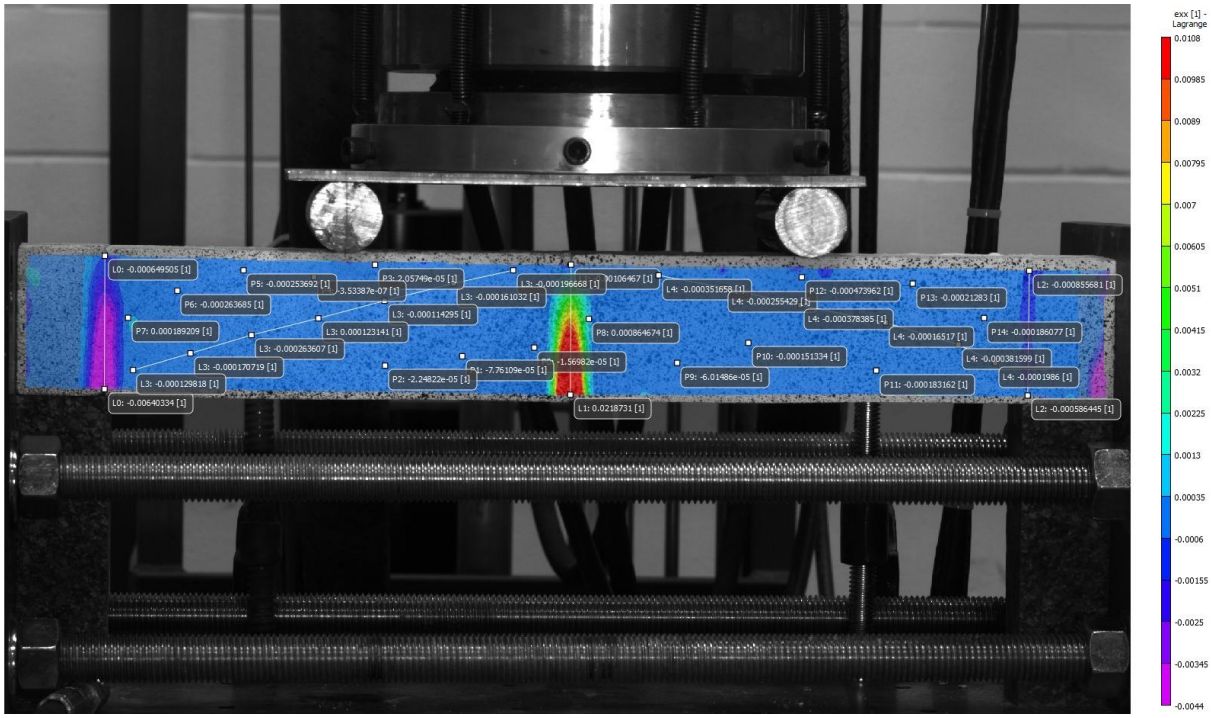

Figure 3-25 Strain ε_{xx} contour of the Image Plaster1-038

Figure 3-25 shows that it is under compression over the whole beam thickness between the midspan and abutment.

The strain along the midspan was extracted and shown in Figure 3-26. The strain was fitted by a linear equation, Equation -3-16.

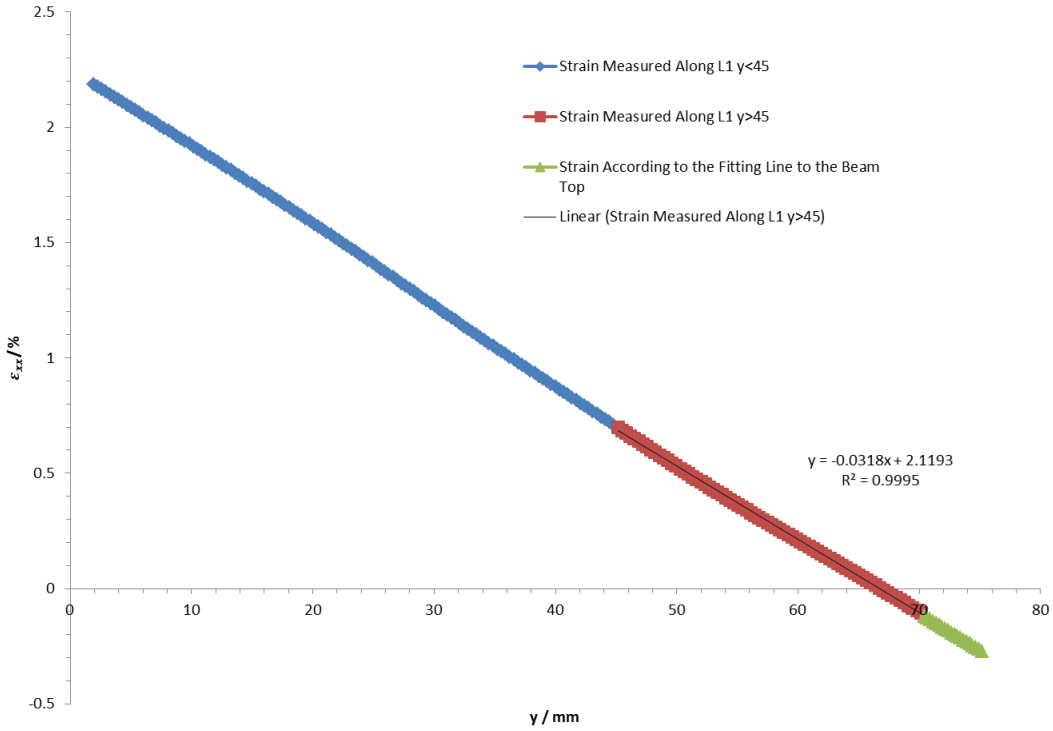

Figure 3-26 Strain along the line *L1* at the midspan of Image Plaster1-038

The strain along *L1* at the upper midspan:

$$\varepsilon_{xx} = -0.0318y + 2.1193 \quad \text{when } y > 45, \text{ with } R^2 = 0.99 \qquad \text{Equation -3-16}$$

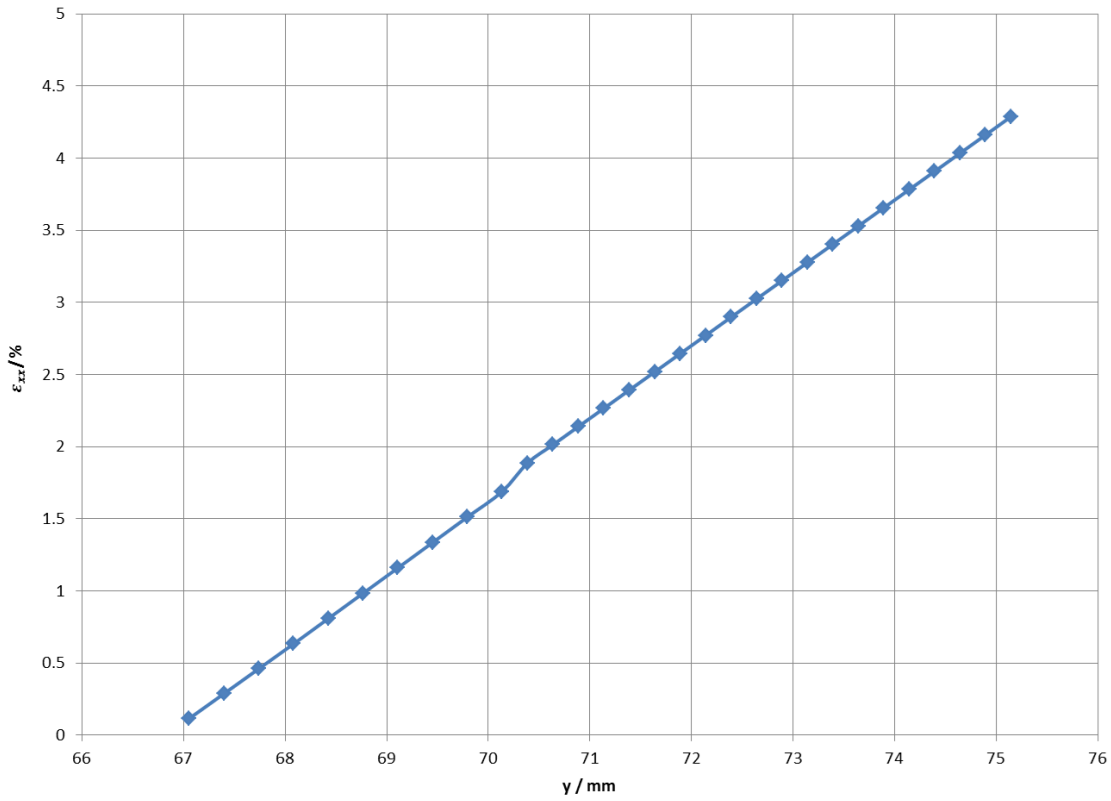

Figure 3-27 Compressive Stress along the line *L1* at the midspan of Image Plaster1-038

With the Young's modulus, the stress at the midspan was obtained as Equation 3-17. The ratio of stress distribution depth to beam thickness was got in Equation 3-19. The stress distribution at the upper part of midspan is shown in Figure 3-27.

$$\sigma_{xx} = 0.5403y - 33.6121 \quad \text{when } y > 45 \qquad \text{Equation 3-17}$$

$$t = 75.145 \qquad \text{Equation 3-18}$$

$$N = 0.1131 \qquad \text{Equation 3-19}$$

Similarly, the strain along the abutment was shown in Figure 3-28 and fitted by Equation 3-20.

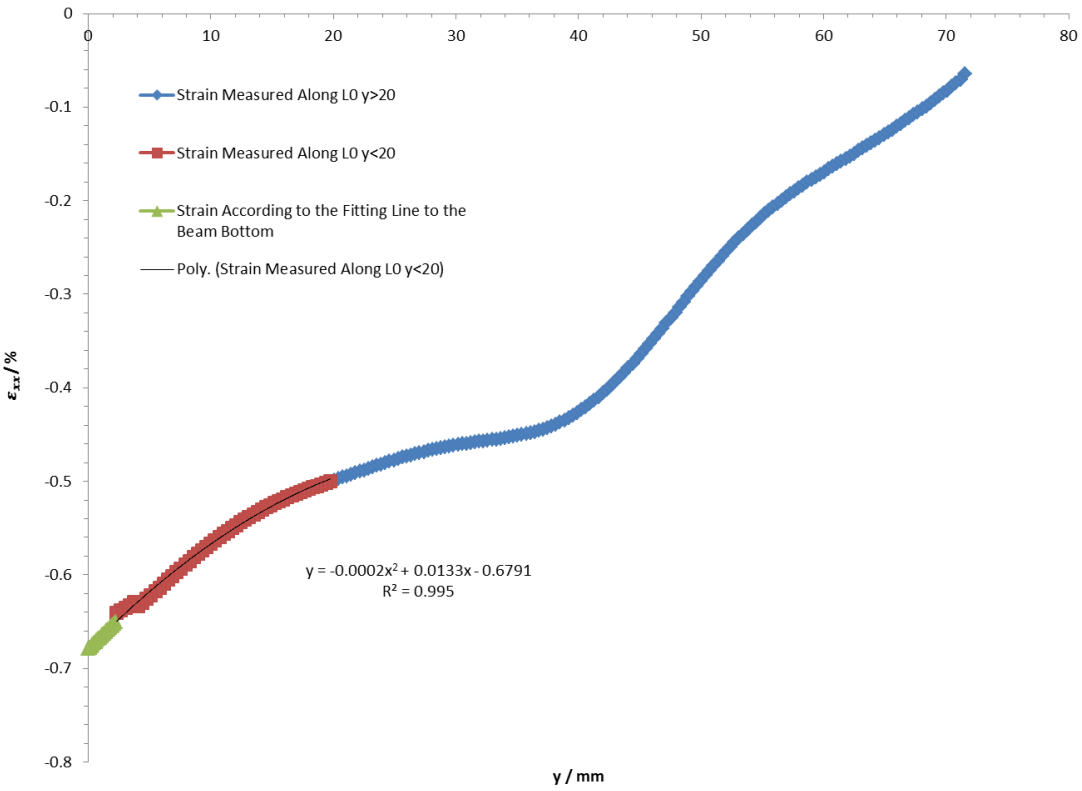

Figure 3-28 Strain along the line *L0* at the abutment of Image Plaster 1-038

$$\varepsilon_{xx} = -0.0002y^2 + 0.0133y - 0.6791 \quad \text{when } y < 20, \text{ with } R^2 = 0.995 \qquad \text{Equation 3-20}$$

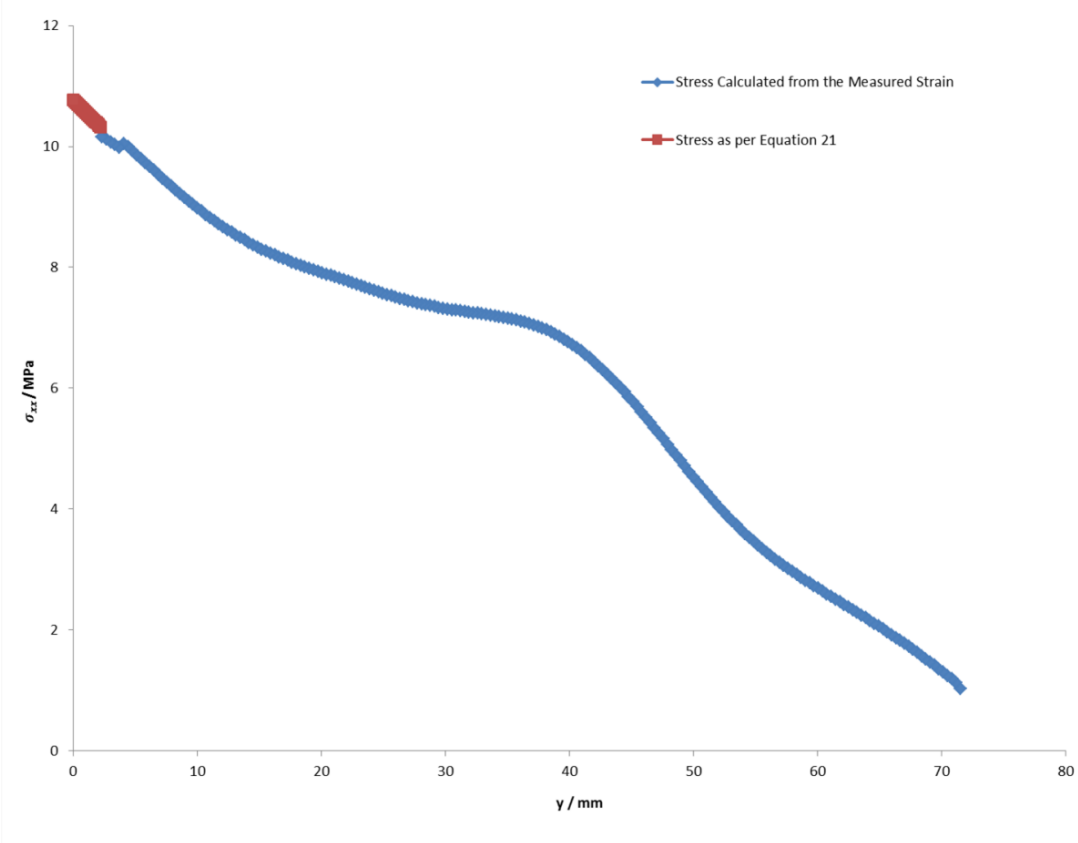

Figure 3-29 Stress Distribution along the line *L0* at the abutment of Image Plaster1-038

The stress was calculated along *L0* at the lower abutment. It was shown in Figure 3-29 and Equation 3-21. The ratio of stress distribution at abutment to the beam thickness is shown in Equation 3-23.

$$\sigma_{xx} = 0.003172y^2 - 0.2109y + 10.7705 \quad \text{when } y < 20 \qquad \text{Equation 3-21}$$

$$t = 76.16 \qquad \text{Equation 3-22}$$

$$n = 1 \qquad \text{Equation 3-23}$$

a) Image Plaster 1-070

The contour of the horizontal strain ε_{xx} is shown in Figure 3-30. The strain along midspan was extracted and shown in Figure 3-31.

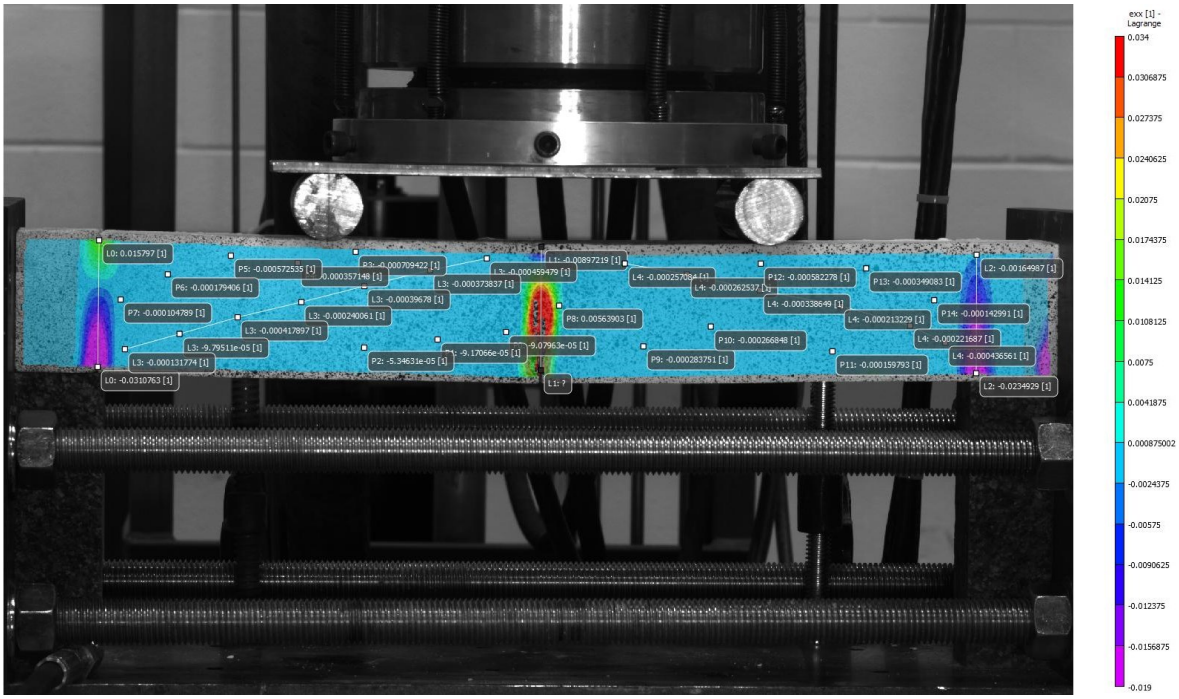

Figure 3-30 Strain ε_{xx} contour of the Image Plaster1-070

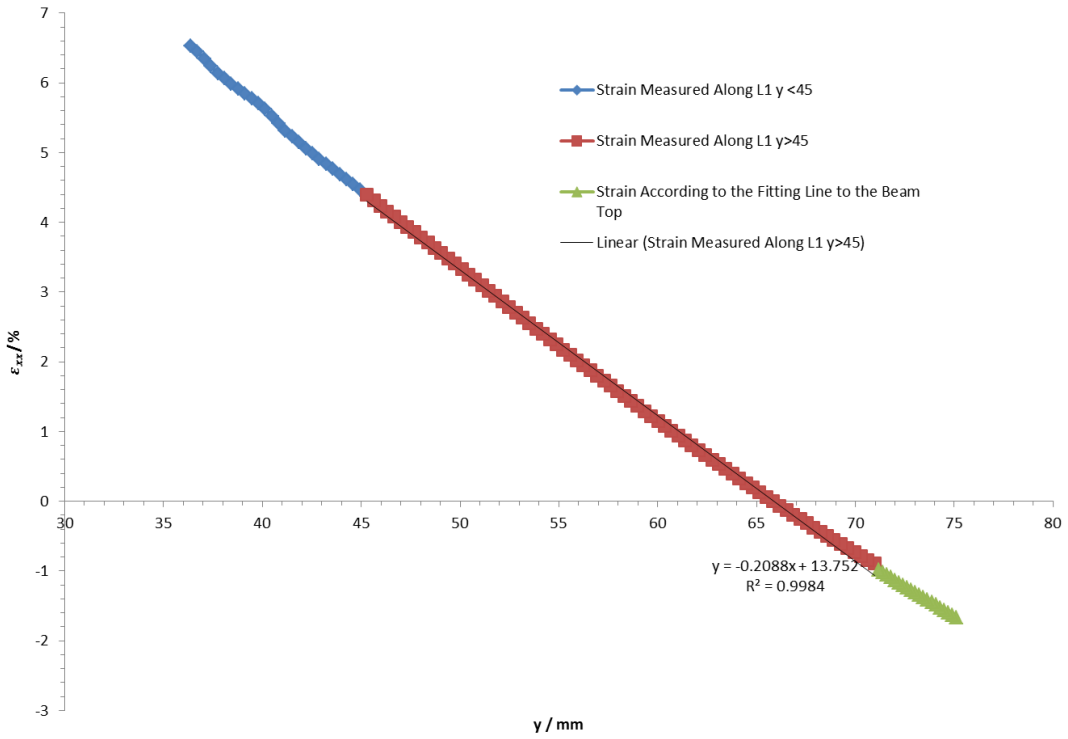

Figure 3-31 Strain along the line *L1* at the midspan of Image Plaster1-070

The strain along *L1* at the upper midspan can be fitted as:

$$\varepsilon_{xx} = -0.2088y + 13.752 \quad \text{when } y > 45, \text{ with } R^2 = 0.9984 \qquad \text{Equation 3-24}$$

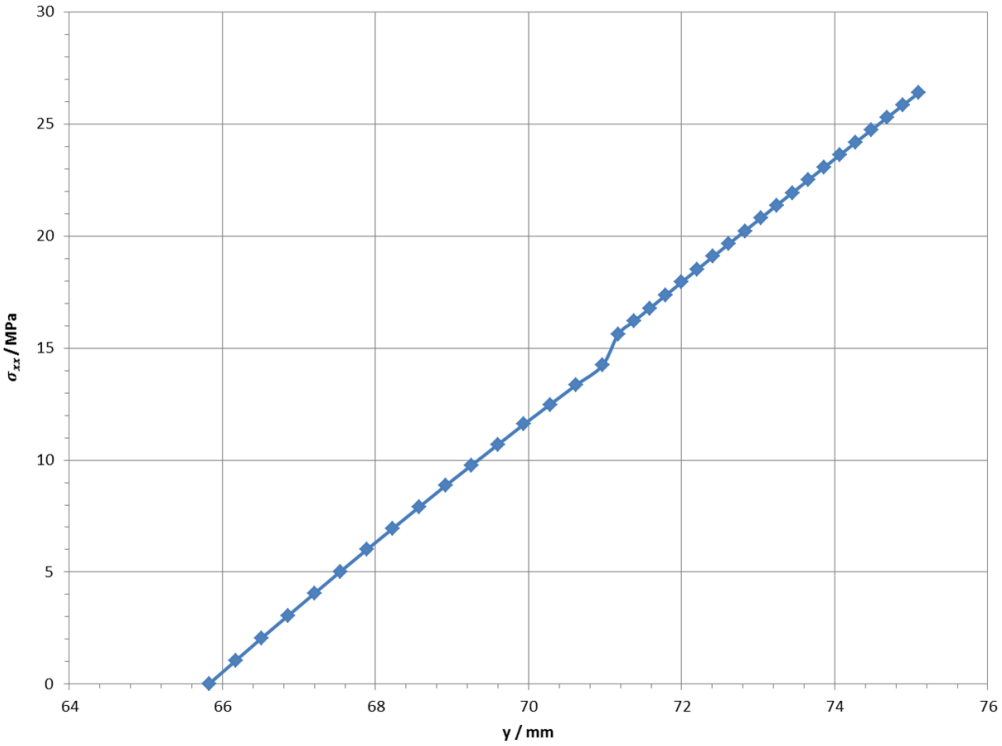

Figure 3-32 Compressive Stress along the line *L1* at the midspan of Image Plaster1-070

The stress along *L1* at the upper midspan is shown in Figure 3-32 and Equation 3-25. The ratio of depth of stress distribution to beam thickness is calculated as shown in Equation 3-27.

$$\sigma_{xx} = 3.3116y - 218.107 \quad \text{when } y > 45 \qquad \text{Equation 3-25}$$

$$t = 75.0984 \qquad \text{Equation 3-26}$$

$$N = 0.1234 \qquad \text{Equation 3-27}$$

The strain along the abutment was shown in Figure 3-33.

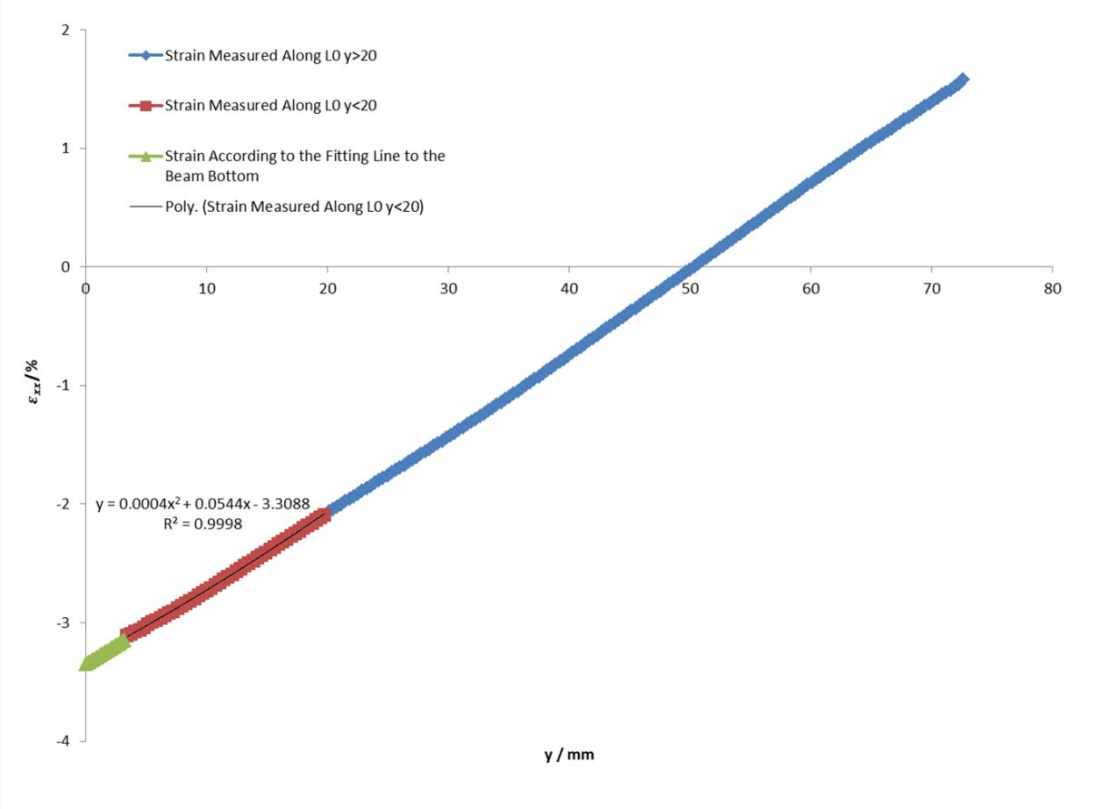

Figure 3-33 Strain along the line *L0* at the abutment of Image Plaster 1-070

The strain along *L0* at the lower abutment was fitted by:

$$\varepsilon_{xx} = 0.0004y^2 + 0.0544y - 3.3088 \quad \text{when } y < 20, \text{ with } R^2 = 0.9998 \qquad \text{Equation 3-28}$$

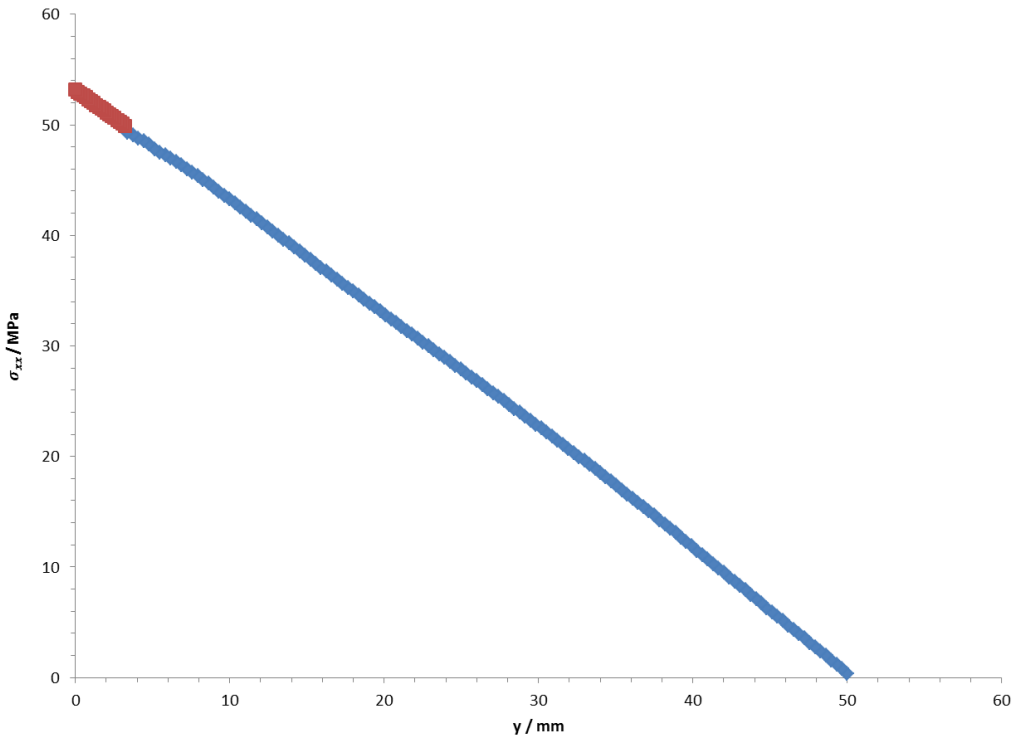

Figure 3-34 Stress Distribution along the line *L0* at the abutment of Image Plaster1-070

The stress along *L0* at the lower abutment was represented by Equation 3-29 and shown in Figure 3-34. The ratio of depth of stress distribution to the beam thickness was calculated and shown in Equation 3-31.

$$\sigma_{xx} = -0.006344y^2 - 0.863y + 52.477 \quad \text{when } y < 20 \qquad \text{Equation 3-29}$$

$$t = 75.09 \qquad \text{Equation 3-30}$$

$$n = 0.666 \qquad \text{Equation 3-31}$$

3.3 Conclusion

The characteristics of stress distribution are summarized in Table 3-5. From these physical tests utilizing the photogrammetric measures, it is firstly found that the stress distributions at the midspan and abutment are different both in shape and depth. And the stress distribution is changing as the loading changes as well. These are different from the assumptions made in previous analysis. These finds should be included the theoretical modelling of voussoir beams.

It is should be noted the strain measured including not only the strain in the beam body but also the displacement of the joints. This resulted the relative large strain at the joints.

The findings are summarized as following:

1) The stress distribution at the midspan is best fitted by a linear function, and the extent of the distribution is much smaller than it is at the abutment. The depth of the distribution is changing with the loading increase.
2) The stress distribution at the abutment is best fitted by a polynomial function, and the extent of the distribution is more than one half of the beam's thickness. The distribution decreases rapidly with an increasing load.
3) The maximum stress at the abutment is larger than it is at the midspan. The first stress is nearly three times that of the last one.
4) The shear sliding failure at the abutments is likely to happen with the voussoir beams of high strength and low span/thickness ratio. For stable voussoir beams, sliding also happened at the beginning of the test, until it ceased at a certain stage. The load-bearing ability of the beam kept increasing at this time. This indicates the onset of stable arching after initial shear.

5) Except for the area near the top of the abutment, the whole beam is under axial compression. This means that the thickness of the arch developed is equal to the beam's thickness.

Table 3-5 Summary of the characteristics of stress distribution

Sample	Image No.	Stress distribution at the abutment		Stress distribution at the midspan	
		Shape	Size/n	Shape	Size/N
Concrete 1	033	$\sigma_{xx} = -0.004004y^2 - 0.4579y + 36.4936$	1	$\sigma_{xx} == 2.60y - 183.97$	0.0614
	040	$\sigma_{xx} = 0.004576y^2 - 1.36136y + 45.6456$	0.5536	$\sigma_{xx} = 3.81y - 278.77$	0.0586
Plaster 1	038	$\sigma_{xx} = 0.003172y^2 - 0.2109y + 10.7705$	1	$\sigma_{xx} = 0.5403y - 33.6121$	0.1131
	070	$\sigma_{xx} = -0.006344y^2 - 0.863y + 52.477$	0.666	$\sigma_{xx} = 3.3116y - 218.107$	0.1234

References

Alejano, L. R., Taboada, J., Garcia-Bastante, F., & Rodriguez, P. (2008). Multi-approach back-analysis of a roof bed collapse in a mining room excavated in stratified rock. International Journal of Rock Mechanics and Mining Sciences, 45(6), 899-913. doi: 10.1016/j.ijrmms.2007.10.001

Beer, G., & Meek, J. L. (1982). DESIGN CURVES FOR ROOFS AND HANGING-WALLS IN BEDDED ROCK BASED ON VOUSSOIR BEAM AND PLATE SOLUTIONS. Transactions of the Institution of Mining and Metallurgy Section a-Mining Industry, 91(JAN), A18-A22.

Brady, B. H. G., & Brown, E. T. (2004). Rock mechanics: For underground mining Kluwer Academic Publishers.

Diederichs, M. S. (2000). Instability of hard rockmasses: The role of tensile damage and relaxation (Ph.D.). Available from ProQuest Dissertations & Theses Full Text. (304676346).

Diederichs, M., & Kaiser, P. (1999). Stability of large excavations in laminated hard rock masses: The voussoir analogue revisited. International Journal of Rock Mechanics and Mining Sciences, 36(1), 97-117. doi:10.1016/S0148-9062(98)00180-6

Evans, W. H. (1941). The strength of undermined strata. Trans. Inst. of Mining and Metallurgy, 50, 475-500.

Hutchinson, D. J., Diederichs, M., Pehme, P., Sawyer, P., Robinson, P., Puxley, A., & Robichaud, H. (2008). Geomechanics stability assessment of world war I military excavations at the canadian national vimy memorial site, france. International Journal of Rock Mechanics and Mining Sciences, 45(1), 59-77. doi: 10.1016/j.ijrmms.2007.04.014

Ju, J., & Xu, J. (2013). Structural characteristics of key strata and strata behaviour of a fully mechanized longwall face with 7.0 m height chocks. International Journal of Rock Mechanics and Mining Sciences, 58, 46-54. doi: 10.1016/j.ijrmms.2012.09.006

Mottahed, P., & Ran, J. (1995). DESIGN OF THE JOINTED ROOF IN STRATIFIED ROCK BASED ON THE VOUSSOIR BEAM MECHANISM. Cim Bulletin, 88(994), 56-62.

Please, C. P., Mason, D. P., Khalique, C. M., Ngnotchouye, J. M. T., Hutchinson, A. J., van der Merwe, J. N., & Yilmaz, H. (2013). Fracturing of an euler-bernoulli beam in coal mine pillar extraction. International Journal of Rock Mechanics and Mining Sciences, 64, 132-138. doi: 10.1016/j.ijrmms.2013.08.001

Sofianos, A. (1996). Analysis and design of an underground hard rock voussoir beam roof. International Journal of Rock Mechanics and Mining Sciences & Geomechanics Abstracts, 33(2), 153-166. doi:10.1016/0148-9062(95)00052-6

Sterling, R. L. (1977). ROOF DESIGN FOR UNDERGROUND OPENINGS IN NEAR-SURFACE BEDDED ROCK FORMATIONS (Ph.D.). Available from ProQuest Dissertations & Theses (PQDT). (302852510).

Stimpson, B., & Ahmed, M. (1992). FAILURE OF A LINEAR VOUSSOIR ARCH - A LABORATORY AND NUMERICAL STUDY. Canadian Geotechnical Journal, 29(2), 188-194.

Talesnick, M. L., Bar Ya'acov, N., & Cruitoro, A. (2007). Modeling of a multiply jointed voussoir beam in the centrifuge. Rock Mechanics and Rock Engineering, 40(4), 383-404. doi:10.1007/s00603-006-0104-9

Tsesarsky, M., & Talesnick, M. L. (2007). Mechanical response of a jointed rock beam - numerical study of centrifuge models. International Journal for Numerical and Analytical Methods in Geomechanics, 31(8), 977-1006. doi:10.1002/nag.568

Vic-3D 2010 reference manual (2010). Correlated Solutions.

Wright, F. D. (1974). Design of roof bolt patterns for jointed rock. (USBM Grant Final Report). College of Engineering, University of Kentucky, distributed by National Technical Information Service, Springfield, Va.

Yang, J., & Shang, Y. (2007). Experimental study on complete mechanical characteristics of voussoir beam in stratified rock. Yanshilixue Yu Gongcheng Xuebao/Chinese Journal of Rock Mechanics and Engineering, 26, 2852-2857.

4 Numerical Investigation on the Behavior of Voussoir Beams[2]

4.1 Introduction

The physical investigation described in the previous part provided direct insights into the behavior of voussoir beams under transverse loading, especially the shape of the stress distribution at the abutments and midspan. Nevertheless, due to the difficulties in physical setup, there are many variances between experiments which are difficult to control, such as horizontal confinement, joint conditions. It is hard/impossible to achieve the perfect symmetry in physical setup. This makes it hard to further the investigation on the behavior of voussoir beams by physical experiments. Numerical modeling was used to enhance the understanding of the voussoir beams behavior.

The Finite Element Code, *Phase² 8.0*, was selected to numerically model the behavior of voussoir beams under transverse loading due to its capacity for modeling joints, providing multiple material models for rock, and providing flexibility for the staging of loading (Phase2 features overview.2014).

The uniaxial compression test and the direct splitting test were used to calibrate the numerical models. A series of numerical tests were performed, accounting for the common ratios of span to thickness for stratified rock strata encountered in the field. The results from the modeling are summarized and discussed in closing.

---

2 The content of this chapter has been prepared and submitted as a journal manuscript: Hu, C; Apel, D; Sudak, L; Szymanski, J; Liu, W. V. (2016) Numerical Investigation on the Behavior of Voussoir Beams. *International Journal of Rock Mechanics and Mining Sciences (Submitted)*

4.2 Phase2 Numerical Modeling

4.2.1 Cohesion-softening friction-hardening (CSFH) material model

Based on the laboratory test results, the linear Mohr-Coulomb model was considered the most appropriate for the intact concrete specimens. According to Edelbro's research in *Phase*^{2} modeling, the results from the cohesion-softening friction-hardening (CSFH) model best captured the observed rock behavior in the field (Edelbro, 2010). In the cohesion-softening friction-hardening (CSFH) model, peak cohesion equals to the tested uniaxial compression strength. The strength parameters used in the modeling were presented in Section 3 below, on Model Calibration.

4.2.2 Indicator of Failure for Voussoir beams

The maximum shear strain is the most reliable indicator of fallout according to Edelbro's research (Edelbro, 2010). As noted below, the maximum shear strain was also found to be the most reliable indicator of failure for voussoir beams (see Section 4.3).

4.2.3 Heterogeneous Approach

The concrete specimens investigated were mixed by sand, cement, and water. The presence of a granular material, sand, made the concrete cement heterogeneous. According to Lan's investigation (Lan, Martin, & Hu, 2010), the presence of material and geometric heterogeneity in intact rock can have a significant influence on intact rock behavior. The heterogeneity was treated by applying the Voronoi joint patterns by Lan (Lan et al., 2010) and Cui (Cui, 2012). The Voronoi tessellation option in *Phase*^{2} was used to simulate the geometric heterogeneity of the grains and/or clumps thought to be present in the concrete specimen, similar to the approach of Cui (Cui, 2012). Two-dimensional Voronoi tessellation is a process that randomly subdivides a

plane into non-overlapping convex polygons. A Voronoi joint network consists of joints that are defined by the bounding segments of these polygons (Dershowitz, 1985). This Voronoi tessellation scheme when combined with discrete joints can simulate both intact rock breakage and slip along a discrete joint.

Phase^2 is able to create the Voronoi tessellation pattern automatically. In the following models, the joint density was defined by using the average joint length equal to 1mm. This was a practical minimum selected for the computing capacity available. The Voronoi tessellation at this scale was experimental in *Phase*^{2} and several modifications were made by the developers of the software to accommodate this small-scale feature.

4.3 Model Calibration

4.3.1 Uniaxial Compression

The concrete specimen model in *Phase*^{2} has the same dimension as the specimen tested in laboratory, i.e., 50 mm diameter by 100 mm height. A steel cap and pedestal with a Young's modulus of 200 *GPa* were put on the top and bottom of the sample, respectively, to simulate the end's treatment for the physical sample tested. The steel cap and the sample were separated by a horizontal joint. There is also a horizontal joint between the pedestal and concrete sample. The bottom of the pedestal was fixed to prevent movement in both X and Y directions. The vertical sides of the cap and the bottom pedestal were fixed to prevent movement in X direction only. The model in *Phase*^{2} is shown in Figure 4-1.

The CSFH Mohr-Coulomb Failure Criterion was used in the numerical model. Voronoi joint network was applied in the model to simulate the heterogeneity in the physical model. The parameters used in the numerical model are presented in Table 4-1.

In the physical uniaxial compression test of concrete specimens, a vertical displacement rate of 0.005mm/s was applied on the specimen. In the numerical modeling, a 7-staged vertical displacement was applied at the top of the cap, as shown in Table 4-2.

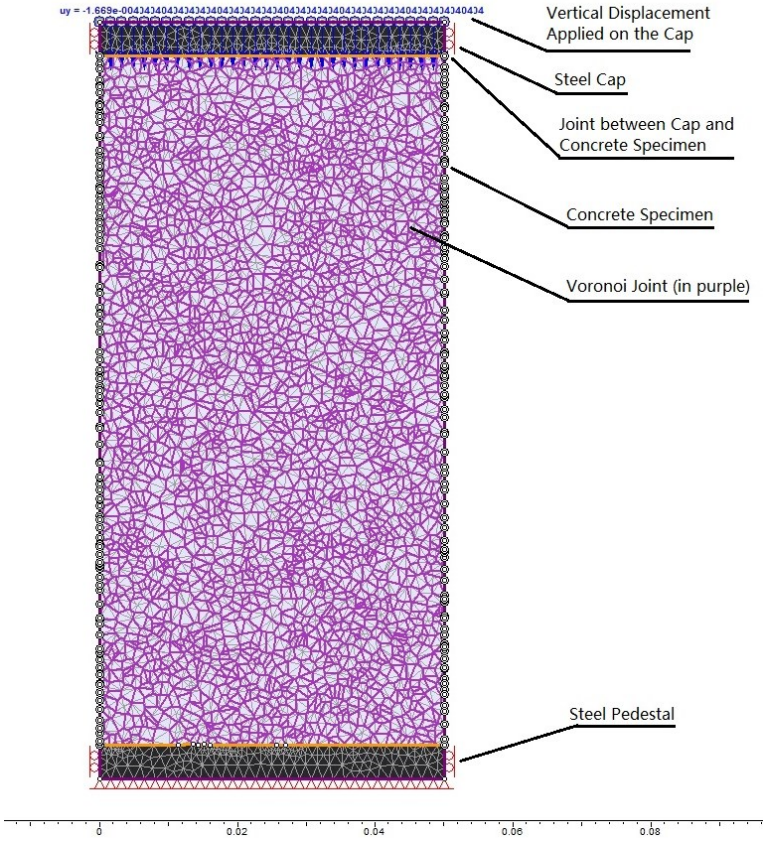

Figure 4-1 Concrete Cylinder Model in *Phase²*

Table 4-1 Material Parameters Used in the *Phase²* Model

	Unit Weight (MN/m^3)	Poisson's Ratio	Young's Modulus (MPa)	Dilation Angle (Deg)	Normal Stiffness (MPa/m)	Shear Stiffness (MPa/m)	Tensile Strength (MPa)		Friction Angle (deg)		Peak Cohesion (MPa)	
							Peak	resid	peak	resid	peak	resid
Concrete	0.021589	0.25	5720	27	N/A		4.4	0	52	56	8.5	4
Steel cap and pedestal	0.027	0.25	200000	N/A	N/A		400	N/A	40	N/A	100	N/A
Voronoi joint					$5*10^8$	$5*10^7$	4.4	0	52	56	8.5	4
Joint between steel cap and concrete specimen, joint between steel pedestal and concrete specimen					$5*10^7$	$5*10^7$	N/A					

Table 4-2 Staged Displacement and Vertical Strain in Numerical Model

Stage	1	2	3	4	5	6	7
Vertical Displacement in mm	0.16687	0.27104	0.35211	0.43241	0.5159	0.65791	0.72237
Corresponding Vertical Strain in %	0.15	0.25	0.32	0.39	0.47	0.60	0.66

A comparison of the relationships of longitudinal stress and longitudinal strain to the physical test and numerical modeling is presented in Figure 4-2. From comparison, the numerical model is able to replicate the concrete specimen behavior in uniaxial compression test. The failure of joint in the model is shown in Figure 4-3. The yield elements are shown in Figure 4-4. In the modeling results, the concrete model has two symmetrical failure surfaces of approximately 45-degrees. This may have been caused by the 2D simulation.

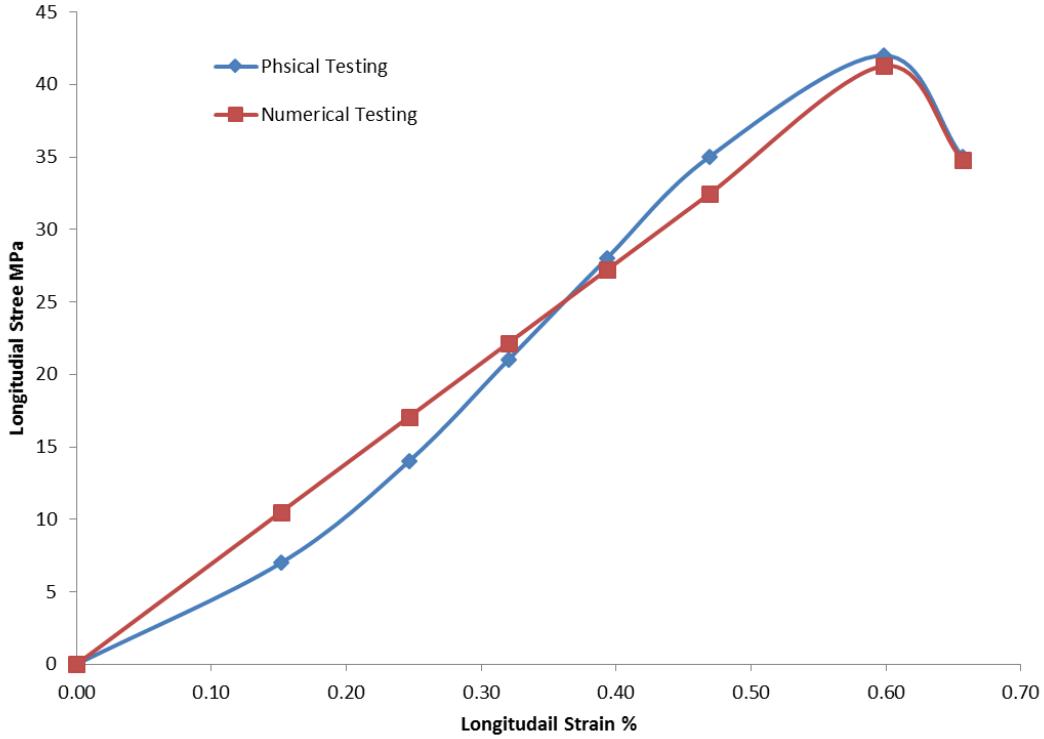

Figure 4-2 Physical Testing Results and Numerical Modeling Results

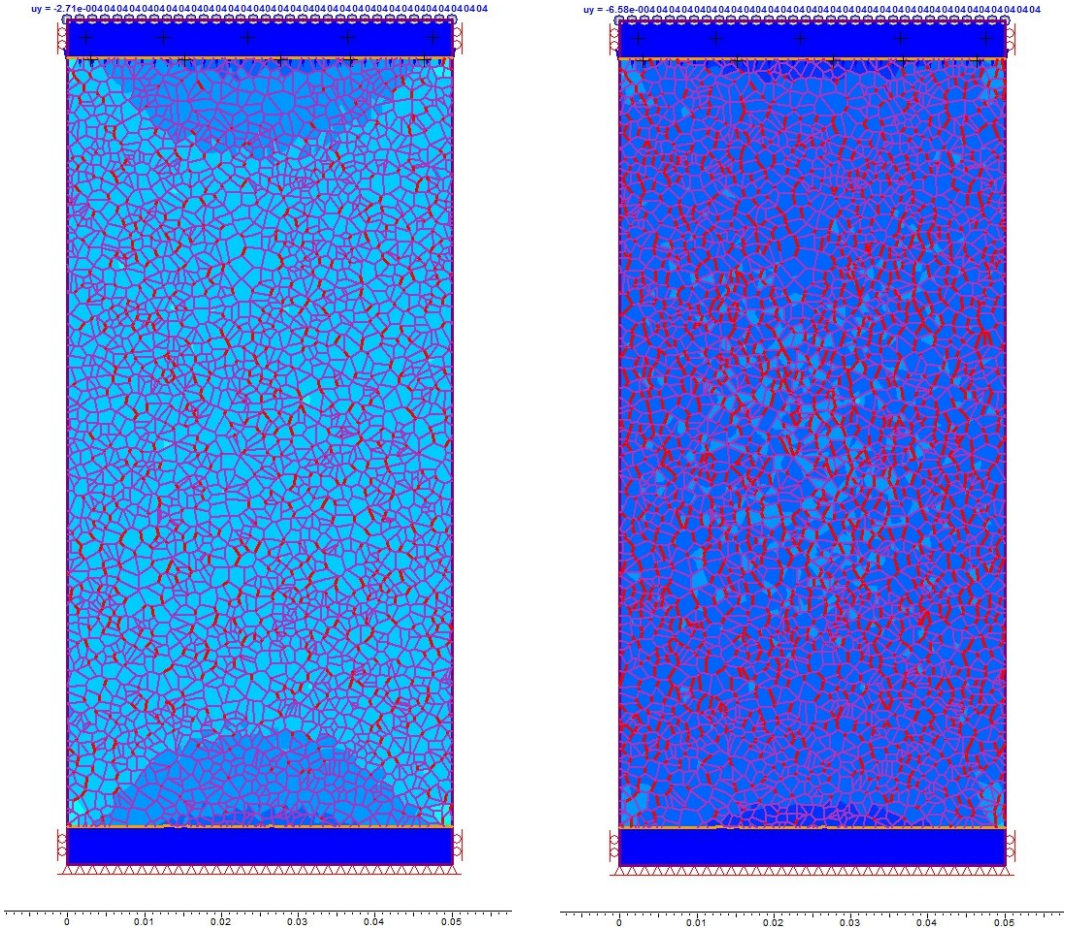

Figure 4-3 Propagation of Joint Failure (mark as thick red lines), Stage 2 left, Stage 6 right

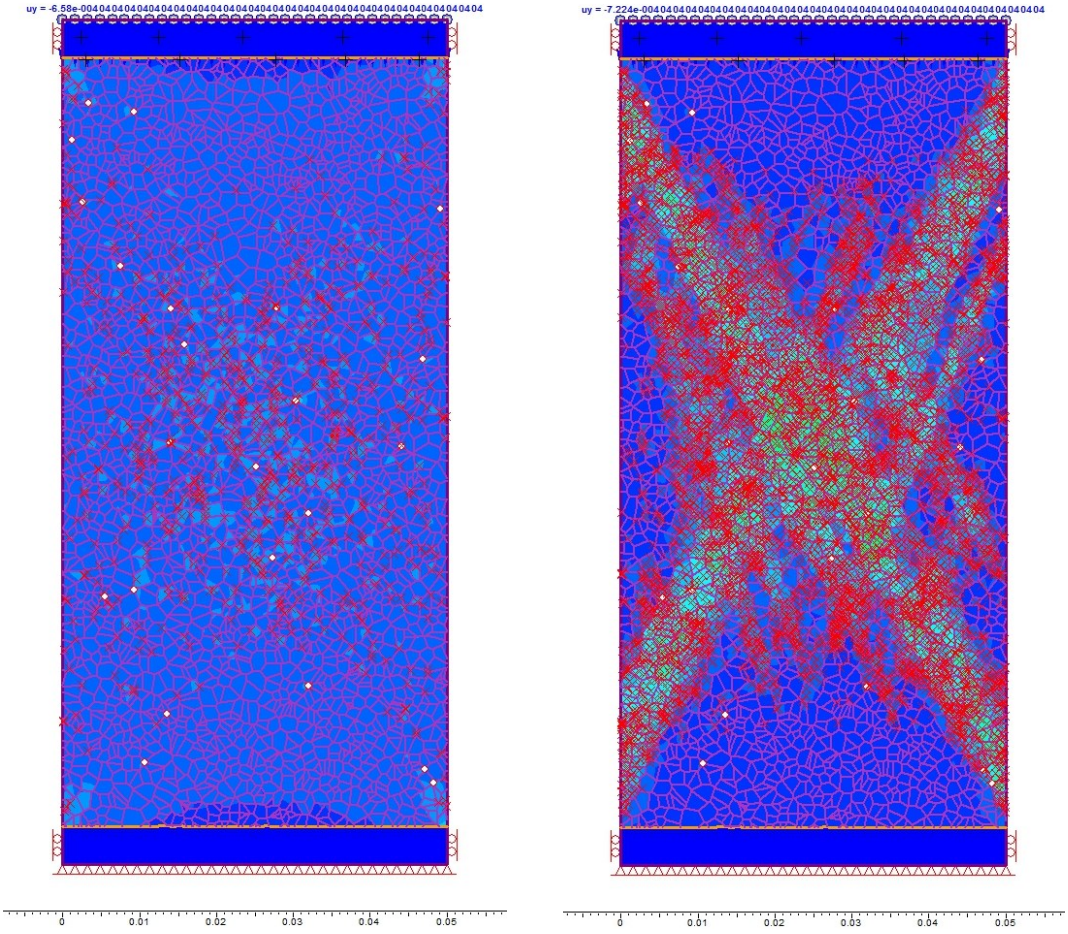

Figure 4-4 Yielded Elements, Stage 6 left, Stage 7 right

4.3.2 Splitting Tensile Strength Test

A 2-D concrete model was built in *Phase*^{2} to simulate the direct splitting test, as shown in Figure 4-5 below. The diameter of the concrete sample is 50mm, which is the same as the tested samples. In the physical testing, the average peak load is 38.1kN. Accordingly, the peak uniform load applied in *Phase*^{2} is 7.6MPa. A five-staged load was applied to simulate the gradual loading process in laboratory testing. The staged load is shown in Table 4-3. The material model is specified in Table 4-1, which is the same as the uniaxial compression test.

The maximum shear strain with yielded elements is shown in Figure 4-6, Figure 4-7 and Figure 4-8. The model failed at the same load as in the physical test. The two symmetrical failure surfaces could be caused by the two-dimensional modeling.

From the calibration study, the numerical model can capture the key characteristics (the break pattern and deformation pattern) of concrete samples through the uniaxial compression test and direct splitting test. The same numerical model will be applied to model voussoir beams.

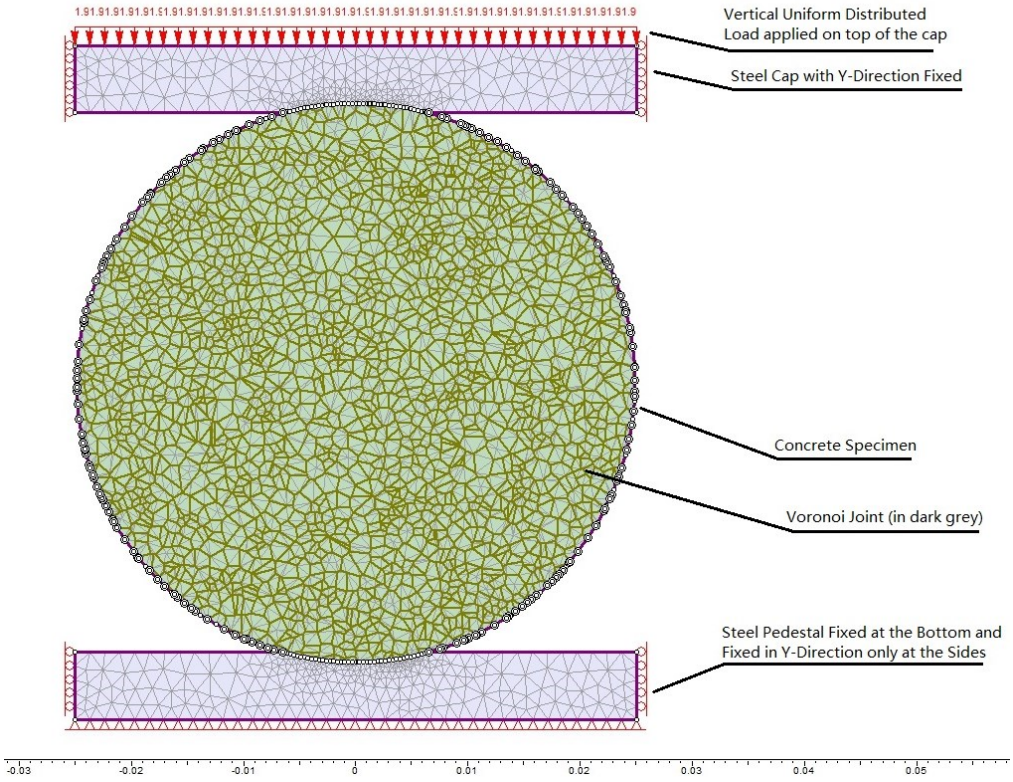

Figure 4-5 Direct Splitting Model

Table 4-3 Staged Load

Stage No.	1	2	3	4	5
Uniform Distributed Load, MPa	1.9	3.8	5.7	6.86	7.6

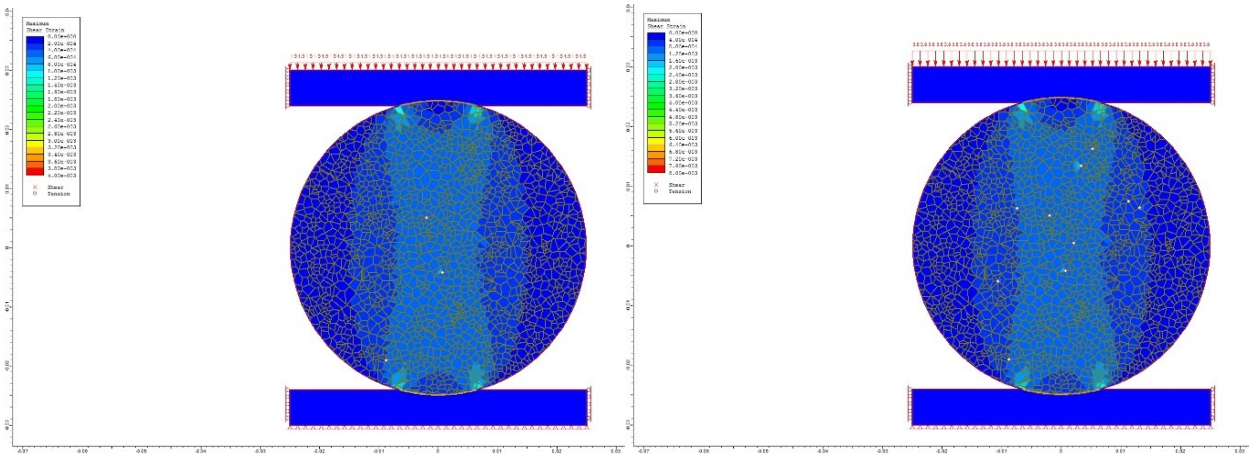

Figure 4-6 Maximum Shear Strain with Yielded Elements at Stage 1 (Left) and Stage 2 Loading (right)

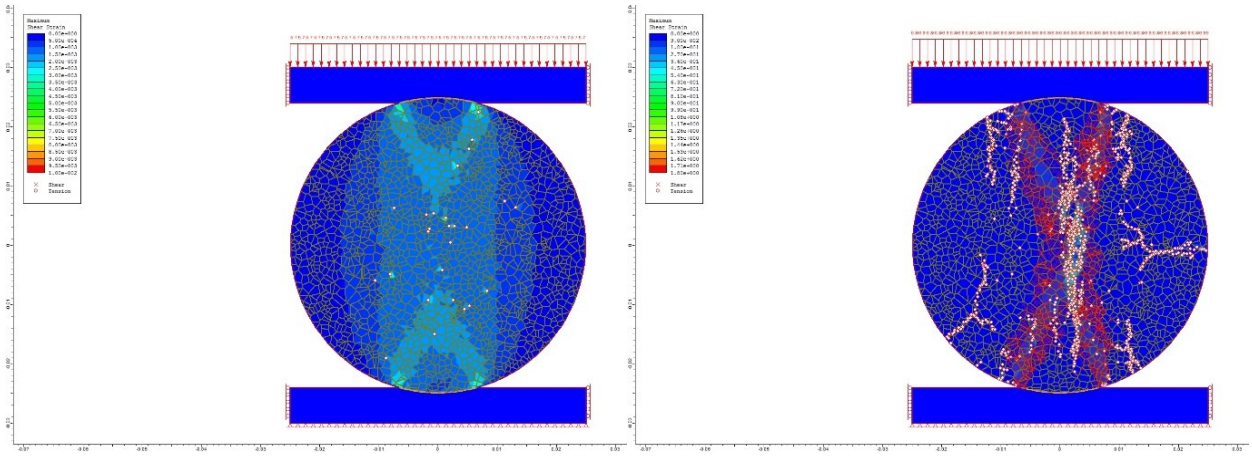

Figure 4-7 Maximum Shear Strain with Yielded Elements at Stage 3 (Left) and Stage 4 Loading (Right)

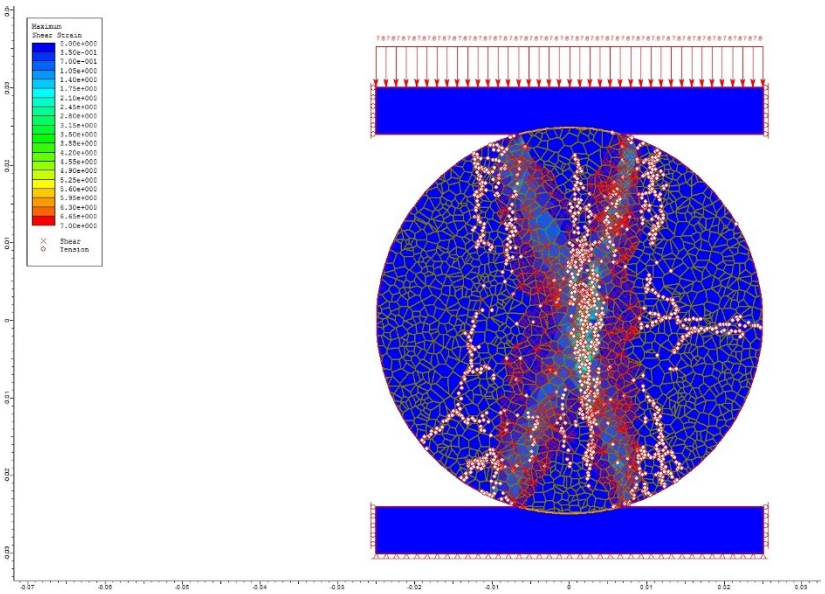

Figure 4-8 Maximum Shear Strain with Yielded Elements at Stage 5 Loading

4.4 Numerical Modeling

4.4.1 Voussoir Beam Model

A voussoir beam model was created in *Phase*^{2}, as shown in Figure 4-9. This model has the same dimensions as the concrete Model 1, with a span/depth ratio of 6.3.

All the material properties applied in the model except the normal stiffness and shear stiffness of the joints are shown above in Table 4-1. The behavior of the numerical model was compared with its physical test, using two load conditions where the first load is 2.05KN, and the second is 4.01KN. Under the same load conditions, the physical test results of voussoir beams of the same dimensions are presented in Physical investigation of this research.

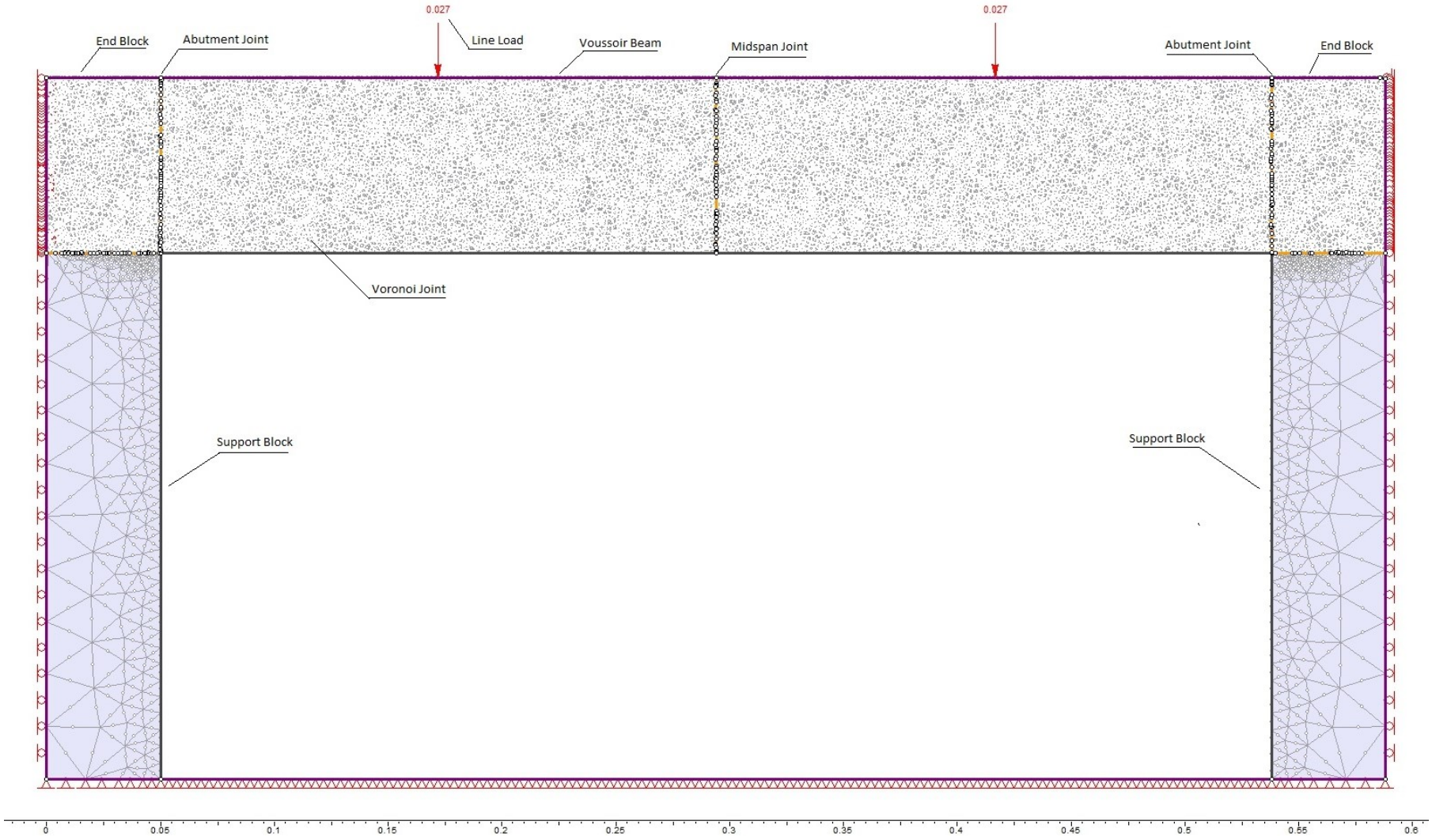

Figure 4-9 Voussoir Beam Model in *Phase*[2]

4.4.2 Normal Stiffness and Shear Stiffness for the Joints of Concrete Blocks

Normal stiffness of the joints between concrete blocks has a major impact on the modeling of voussoir beams. Unlike the shear stiffness, the normal stiffness for joints between concrete specimens is difficult to test because of the hardness of the rock. Zangerl analysed 115 different laboratory and in-situ normal closure experiments in granitic rock (Zangerl, Evans, Eberhardt, & Loew, 2008). The results showed a very wide range of normal stiffness characteristic values. The normal stiffness is highly stress-dependent. It was found that $10mm^{-1}$ to $70mm^{-1}$ multiples of normal stress is the common range for normal stiffness. From the physical test, the stress at the abutment is approximately three times the stress at the midspan. Therefore, in the numerical modeling, it is assumed that the normal stiffness of the abutment joint ($K_{n-abutment}$) is three times the normal stiffness of the midspan joint ($K_{n-midspan}$), as shown in Equation 4-1.

Several researchers have simulated stratified rock mass behavior using *Phase*^{2} (Barla, Bonini, & Semeraro, 2011; Fortsakis, Nikas, Marinos, & Marinos, 2012; Perras, 2009). In the research described in this chapter, it is found that shear stiffness could not be 316 *MPa/m*, which was the value tested in the lab. If the shear stiffness is 316 *MPa/m*, the result from numerical voussoir beam model would significantly different from the physical model. Barton (Barton, 2007) suggested that the ratio of normal stiffness to shear stiffness is between 11 and 15 for a very good surface. In this chapter, the normal stiffness and shear stiffness ratio was selected to be 15, as the concrete joint is clean and well-mated, as shown in Equation 4-2 and Equation 4-3.

$$K_{n-abutment} = 3K_{n-midspan} \quad \text{Equation 4-1}$$

$$K_{n-abutment} = 15K_{s-abutment} \quad \text{Equation 4-2}$$

$$K_{n-midspan} = 15K_{s-midspan} \quad \text{Equation 4-3}$$

Based on this assumption, the proper value of normal stiffness and shear stiffness was found by comparison with the physical testing results.

4.4.3 Comparison with Physical Testing Results

According to Equation 4-1, Equation 4-2 and Equation 4-3, several combinations of stiffness were tried and the results then compared with the physical modeling results. The stiffness shown in Table 4-4 was selected as the appropriate set of values to duplicate the voussoir beam behavior in the physical test. The abutment stress, as shown in Figure 4-10, is close to the stress measured in the physical test, described in Part 1 of this investigation. The stress distribution at the midspan, shown in Figure 4-11, is also close to the measured distribution. The differences of the deflections from the numerical modeling and physical modeling are presented in Table 4-5. The differences, especially the absolute differences, are within a reasonable range.

The stiffness value in Table 4-4, combined with the material properties in Table 4-1, comprise the material properties used for the following numerical modeling.

Table 4-4 Stiffness of Joints

	Normal Stiffness, MPa/m	Shear Stiffness, MPa/m
Abutment Joints	$5 * 10^6$	$3.33 * 10^5$
Midspan Joint	$1.67 * 10^6$	$1.11 * 10^5$

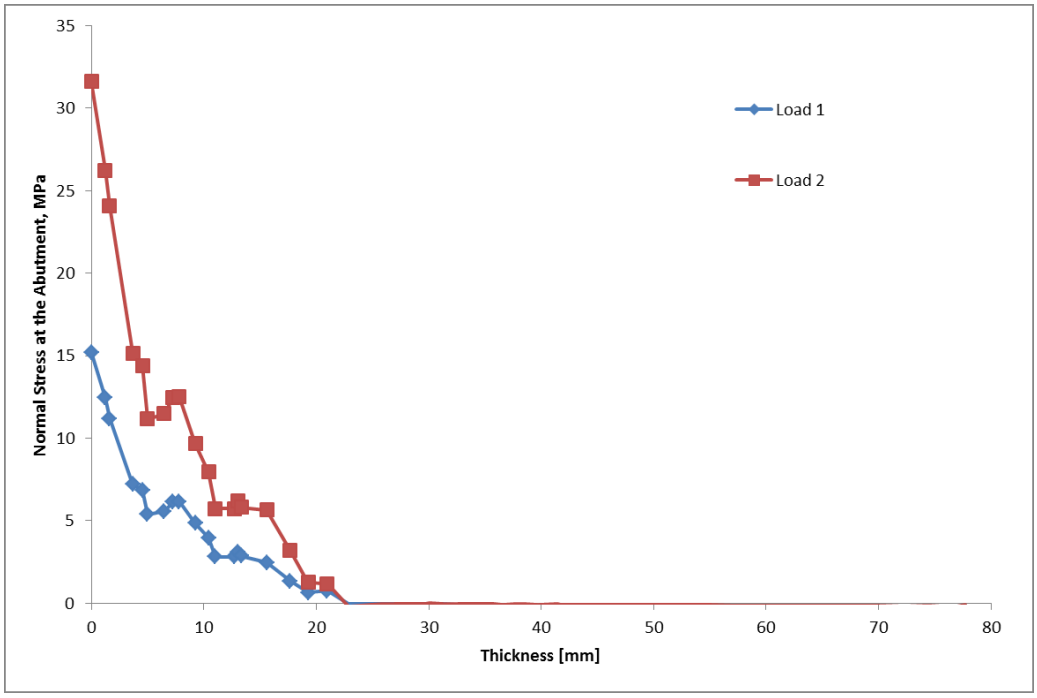

Figure 4-10 Abutment Normal Stress Distribution ("Thickness" is measured from bottom of the voussoir beam)

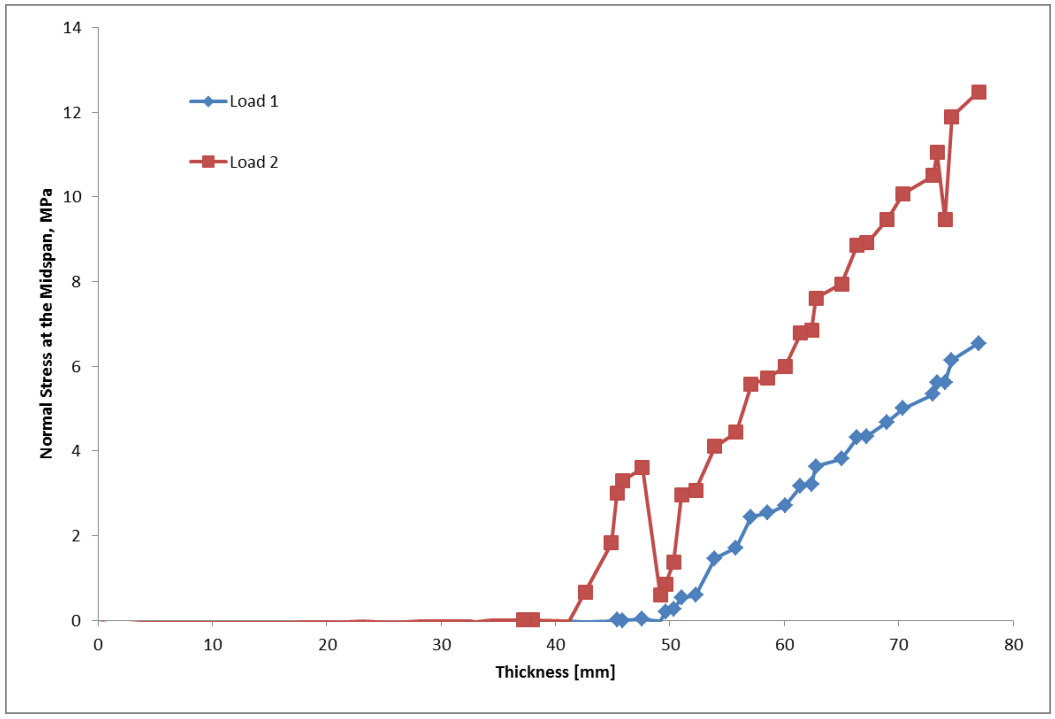

Figure 4-11 Midspan Normal Stress Distribution ("Thickness" is measured from bottom of the voussoir beam)

Table 4-5 Deflection Comparison for the Physical and Numerical Tests

	Load 1 = 2.05kN		Load 2 = 4.01KN	
	Abutment Deflection/mm	Midspan Deflection/mm	Abutment Deflection/mm	Midspan Deflection/mm
Physical Test Results	0.10	0.63	0.11	0.92
Numerical Modeling Results	0.07	0.60	0.11	1.10
Difference/%	30%	-5%	0%	19%

4.4.4 Numerical Modeling

A series of voussoir beams were modeled in *Phase*^{2} using the material properties from previous calibration research, shown in Table 4-1. The model is similar to the model used for calibration, shown in Figure 4-9, with the dimensions that differ specified in Table 4-6.

Table 4-6 Numerical Investigation on Behaviour of Voussoir Beams

No.	Voussoir Models			End Blocks		Transvers Load/kN	
	Span/Thickness	Span/mm	Thickness/mm	Span /mm	Thickness/mm	Load 1	Load 2
1	3	300	100	50	100	2.05	4.01
2	6	600	100	50	100	2.05	4.01
3	8	600	75	50	75	2.05	4.01
4	10	600	60	50	60	2.05	4.01
5	12	600	50	50	50	2.05	4.01
6	15	600	40	50	40	2.05	4.01
7	18	720	40	50	40	2.05	4.01
8	20	800	40	50	40	2.05	4.01

4.5 Conclusion

The stresses induced at the midspan and abutment of the voussoir models are showed in Figure 4-12, Figure 4-13, Figure 4-14, and Figure 4-15. The midspan deflections, depth of the stress induced at the midspan and abutment, and failure are summarized in Table 4-7. The findings from the numerical modeling are as follows:

1) The stress induced at the abutment is nonlinear, and, at the midspan, it is linear;
2) The stress induced at the abutment is approximately three times the stress at the midspan under the same transverse load;
3) The ratio of the depth of stress induced at the abutment to beam thickness (n) is close to 0.3 before crushing. After the crushing occurred, the ratio increased to close to 0.5. The ratio decreased to 0.3 until it fully crushed the beam;
4) The ratio of the depth of stress induced at the midspan to beam thickness (n) is close to 0.4 before crushing the beam. After the crushing occurred, the ratio increased to close to 1 until it fully crushed the beam.

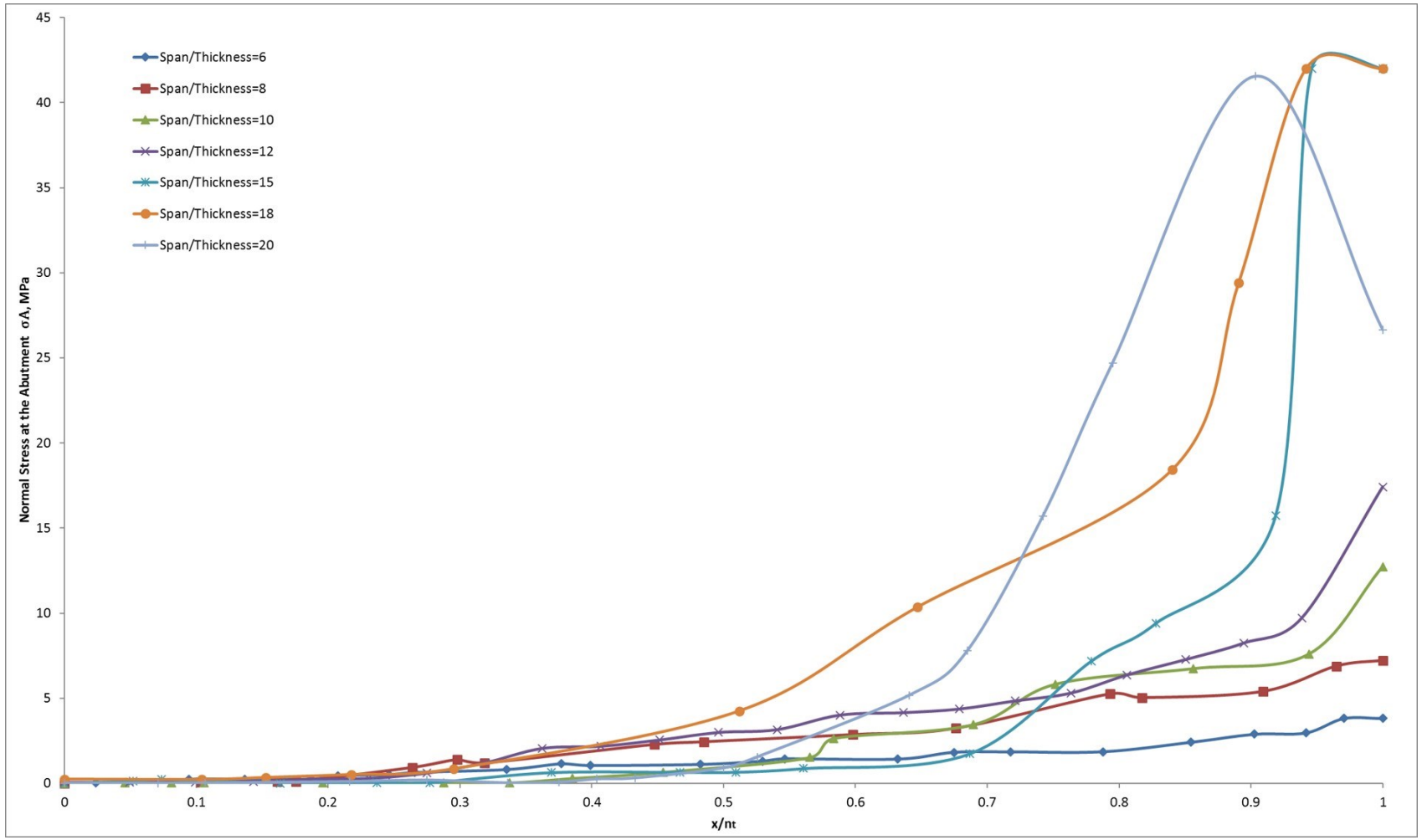

Figure 4-12 Stress Distribution at Abutment under Load 1 (2.05kN)

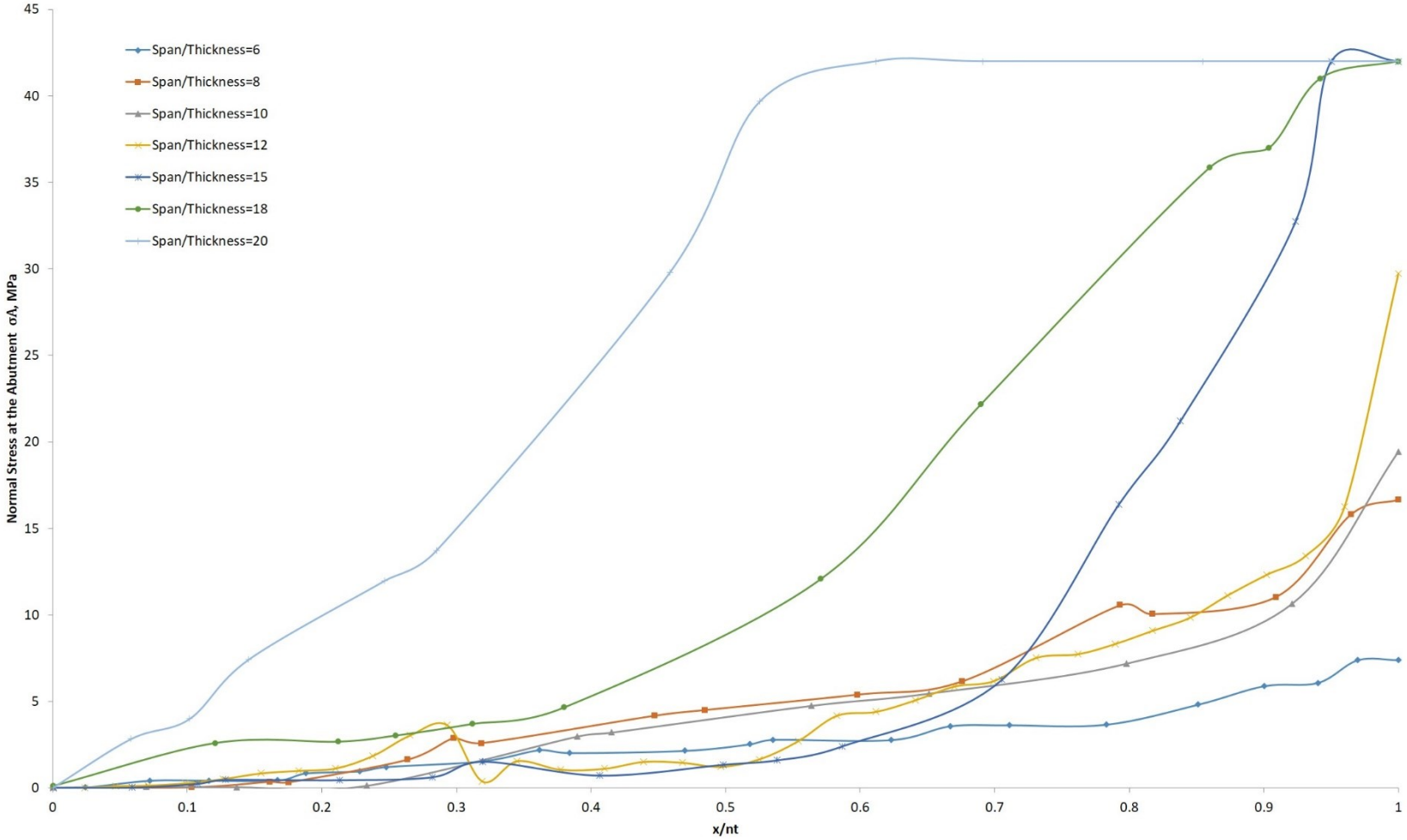

Figure 4-13 Stress Distribution at Abutment under Load 2 (4.01kN)

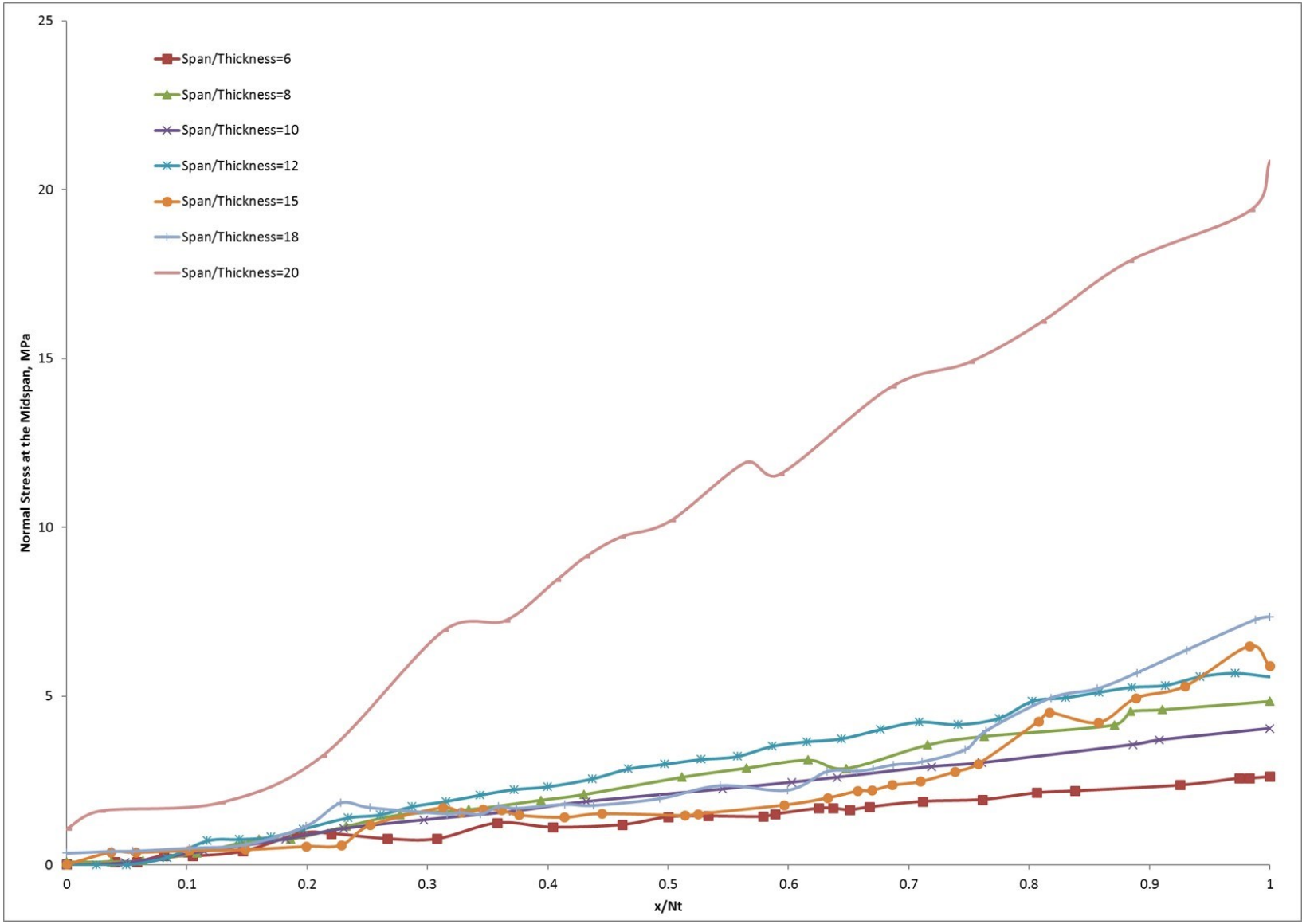

Figure 4-14 Stress Distribution at Midspan under Load 1 (2.05kN)

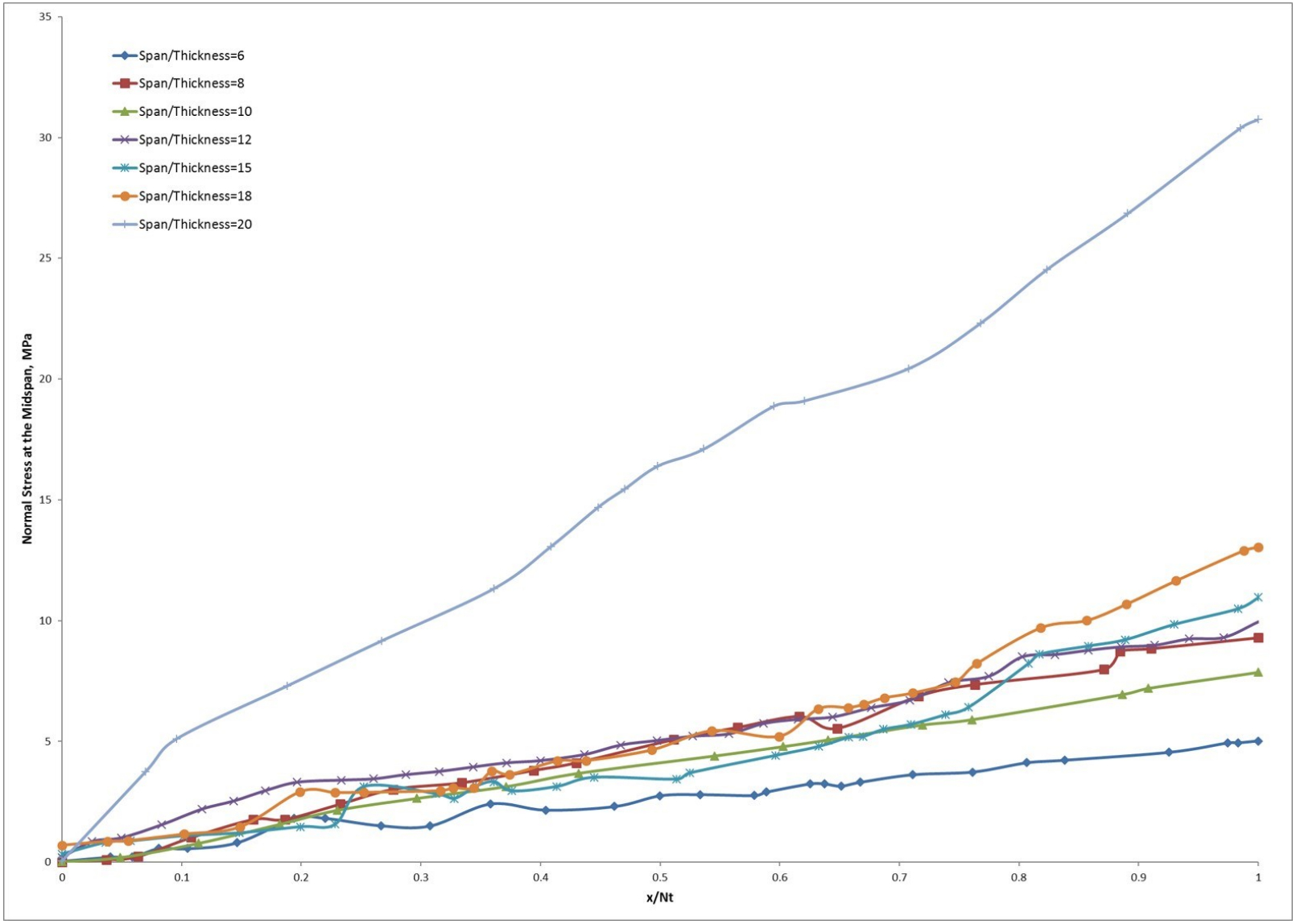

Figure 4-15 Stress Distribution at Midspan under Load 2 (4.01kN)

Table 4-7 Summary of Modeling Results

No.	Midspan Deflection under Load 1, mm	Midspan Deflection under Load 2, mm	Ratio of the depth of stress induced at the abutment to beam thickness, n		Ratio of the depth of stress induced at the midspan to beam thickness, N		Notes
			Load 1	Load 2	Load 1	Load 2	
1	N/A	N/A	N/A	N/A	N/A	N/A	Sliding failure at the abutment
2	0.26	0.49	0.34	0.33	0.38	0.38	No crushing happened
3	0.54	1.05	0.30	0.30	0.36	0.36	No crushing happened
4	0.51	0.97	0.37	0.27	0.43	0.43	No crushing happened
5	0.84	1.78	0.24	0.37	0.33	0.33	Crushing happened at corner of both abutment and midspan
6	1.56	3.17	0.48	0.51	1	1	Crushing happened at corner of both abutment and midspan
7	2.61	5.36	0.29	0.33	1	1	Crushing happened at corner of both abutment and midspan
8	N/A	N/A	0.53	0.35	N/A	N/A	Crushing failure at the middle

References

Barla, G., Bonini, M., & Semeraro, M. (2011). Analysis of the behaviour of a yield-control support system in squeezing rock. Tunnelling and Underground Space Technology, 26(1), 146-154. doi: 10.1016/j.tust.2010.08.001

Barton, N. (2007). Rock quality, seismic velocity, attenuation and anisotropy. [electronic resource] London; New York: Taylor & Francis, c2007.

Cui, Y. (2012). Direct shear failure of a synthetic rock containing discontinuous joints (M.S.). Available from Dissertations & Theses @ University of Alberta. (1173644778).

Dershowitz, W. S. (1985). ROCK JOINT SYSTEMS (Ph.D.). Available from ProQuest Dissertations & Theses Global. (303456905).

Edelbro, C. (2010). Different approaches for simulating brittle failure in two hard rock mass cases: A parametric study. Rock Mechanics and Rock Engineering, 43(2), 151-165. doi:10.1007/s00603-008-0025-x

Fortsakis, P., Nikas, K., Marinos, V., & Marinos, P. (2012). Anisotropic behaviour of stratified rock masses in tunnelling. Engineering Geology, 141, 74-83. doi: 10.1016/j.enggeo.2012.05.001

Lan, H., Martin, C. D., & Hu, B. (2010). Effect of heterogeneity of brittle rock on micromechanical extensile behavior during compression loading. Journal of Geophysical Research-Solid Earth, 115, B01202. doi:10.1029/2009JB006496

Perras, M. A. (2009). Tunnelling in horizontally laminated ground: The influence of lamination thickness on anisotropic behaviour and practical observations from the niagara tunnel project (M.Sc.Eng.). Available from ProQuest Dissertations & Theses Global. (760951037).

Phase^2 features overview. (2014). Retrieved from https://www.rocscience.com/help/phase2/webhelp9/phase2.htm

Zangerl, C., Evans, K. F., Eberhardt, E., & Loew, S. (2008). Normal stiffness of fractures in granitic rock: A compilation of laboratory and in-situ experiments. International Journal of Rock Mechanics and Mining Sciences, 45(8), 1500-1507. doi: 10.1016/j.ijrmms.2008.02.001

5 Theoretical Modeling

5.1 Derivation of the Centroids and Lateral Thrusts for the Stress Distributions located at the Abutment and Midspan of the beam

The initial step in the theoretical analysis of the voussoir beam is the assumption regarding the shape and size of the horizontal compressive stress distributions acting at the abutment and at the center of the beam (which will be referred as "midspan" thereafter). In this model, the stress distributions acting at the abutments and at the midspan are assumed to be a general non-linear form, and the extent of the compression zones of the two distributions are assumed to be different, see Figure 5-1.

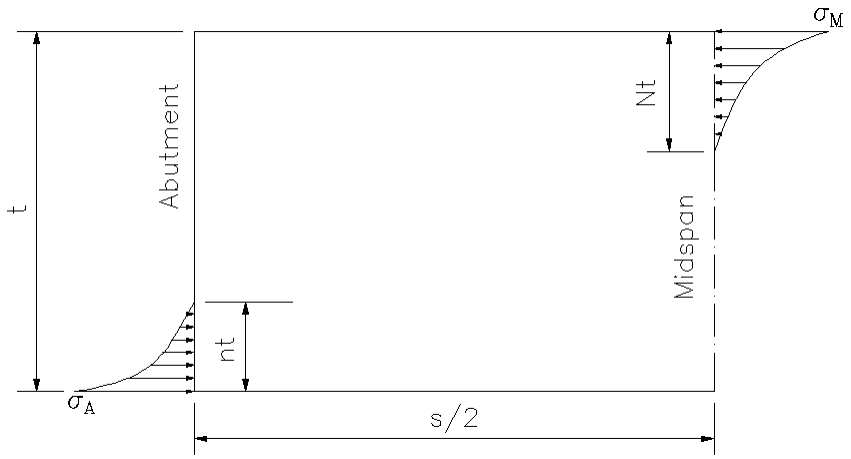

Figure 5-1 Half of the Voussoir Beam Model with General Stress Distributions

Prior to analyzing the Voussoir Beam, the thrust and centroid locations due to the stress distributions must be determined. Therefore, calculations showing the thrust and centroid locations at the abutment and midspan will be examined separately.

The general equation for stress distribution at both the abutment and the midspan is in the form

$$\sigma = \beta x^k \qquad \text{Equation 5-1}$$

Where β and k is a constant.

ABUTMENT

Figure 5-2 illustrates a non-linear stress distribution where the stress at the abutment varies as a power form from a point of zero stress to a maximum stress, σ_A, at the lower fibers over a depth, nt, of the beam. Only the lower half of the voussoir beam model is displayed in Figure 5-2.

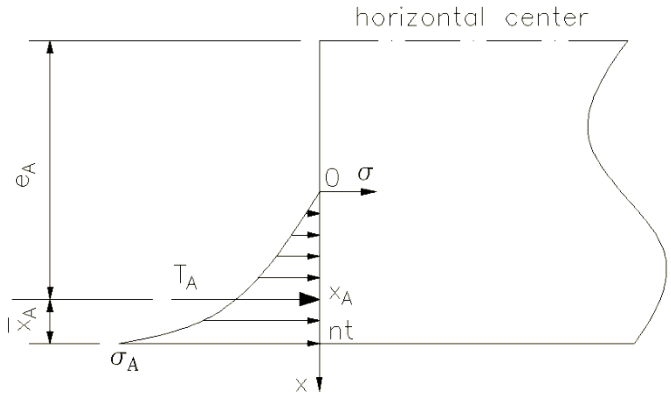

Figure 5-2 Stress distribution at the lower Abutment with the lower half of the model

The value of β can be determined as follows:

When $x = nt$ then $\sigma = \sigma_A$, from Figure 5-2.

Therefore, using Equation 5-1 yields

$$\sigma_A = \beta(nt)^{k_1} \qquad \text{Equation 5-2}$$

$$\beta = \frac{\sigma_A}{(nt)^{k_1}} \qquad \text{Equation 5-3}$$

Hence, the equation of the stress block at the abutments is

$$\sigma_A(x) = \sigma_A\left(\frac{x}{nt}\right)^{k_1} \qquad \text{Equation 5-4}$$

The area under the curve in Figure 5-2 represents the lateral thrust (T_A)

$$T_A = \int \sigma_A(x)dx = \frac{\sigma_A}{(nt)^{k_1}} \int_0^{nt} x^{k_1} dx = \frac{\sigma_A nt}{k_1 + 1}$$ Equation 5-5

The line of action of the resulting lateral thrust, T_A, is assumed to act horizontally through the centroid of the non-linear stress block. The equation of the centroid for the stress block at the abutment is given by:

$$\overline{x_A} = nt - x_A$$ Equation 5-6

where

$$x_A = \frac{1}{T_A} \int_0^{nt} x\sigma_A(x)dx = \frac{1}{T_A} \frac{\sigma_A (nt)^2}{k_1+2} = \left(\frac{k_1+1}{k_1+2}\right)nt$$ Equation 5-7

Hence, the equation of the centroid for the stress block at the abutment is given by

$$\overline{x_A} = \frac{nt}{k_1 + 2}$$ Equation 5-8

MIDSPAN

Figure 5-3 illustrates a non-linear stress distribution where the stress at the center of the beam varies as a power form from a point of zero stress to a maximum stress, σ_M, at the upper fibers over a depth, Nt, of the beam.

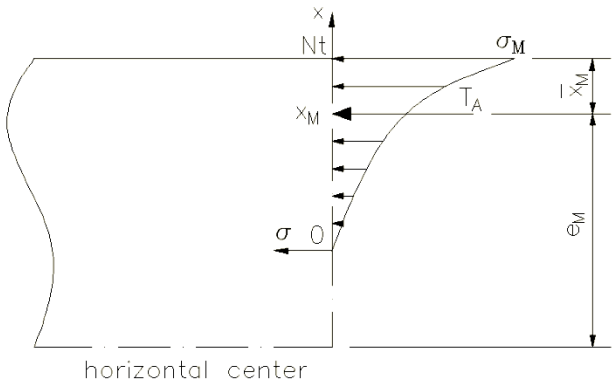

Figure 5-3 Stress distribution at the upper Midspan with the upper half of the model

The determination for the stress distribution, the thrust (T_M) and the centroid ($\overline{x_M}$) at the midspan is similar to that at the abutment. The stress distribution, the thrust (T_M) and the centroid ($\overline{x_M}$) at the midspan are given by:

$$\sigma_M(x) = \sigma_M \left(\frac{x}{Nt}\right)^{k_2} \qquad \text{Equation 5-9}$$

$$T_M = \frac{\sigma_M Nt}{k_2 + 1} \qquad \text{Equation 5-10}$$

$$\overline{x_M} = \frac{Nt}{k_2 + 2} \qquad \text{Equation 5-11}$$

5.2 Derivation of the Moment Arm and Eccentricities of the Voussoir Beam

As the voussoir beam model is not hinged at the lower abutment and upper midspan, it is indeterminate in its actions and is subject to internal stress and abutment forces as a result of thermal expansion.

Normally the Voussoir Beam is a statically indeterminate structure, but because of the uniform loading condition (i.e. self-weight of the beam) a solution can be obtained by analyzing only half of the structure, as shown in Figure 5-4. Please noted, the shear force at the bottom of abutment is not plotted in Figure 5-4 for the neat of the figure. The shear force is a result of normal stress induced at abutment and the relative movement at the abutment. There is no shear force at midspan as no relative movement between the two blocks of voussoir beam.

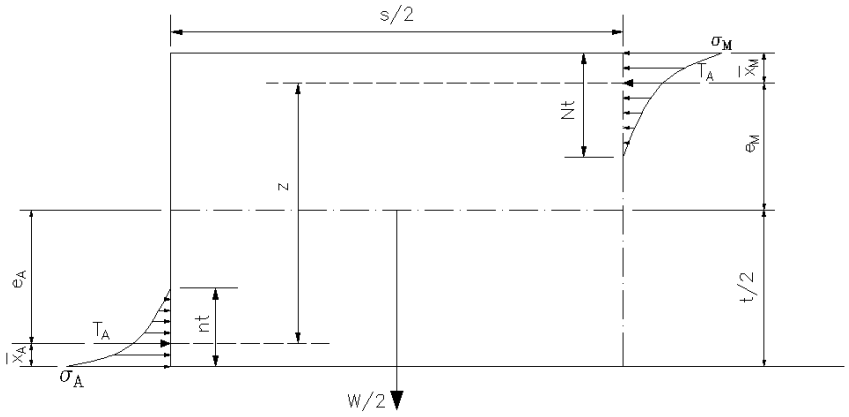

Figure 5-4 Force Diagram for Half Span of Voussoir Beam

Let γ be the unit weight of the voussoir beam and let the beam be of unit depth. Therefore, the weight of half the rock beam is given by:

$$W/2 = \frac{\gamma ts}{2} \quad \text{Equation 5-12}$$

There is no frictional force at the centre as there is no relative movement between the two blocks. The only frictional force happens at the abutment; the magnitude of the friction is equal to half of the weight of the block according to the force equilibrium.

From the force equilibrium, the thrust at the abutment, T_A, and the thrust at the midspan, T_M, must be equal even though the stress distributions are different.

$$T_A = T_M \quad \text{Equation 5-13}$$

$$\frac{\sigma_A nt}{k_1 + 1} = \frac{\sigma_M Nt}{k_2 + 1} \quad \text{Equation 5-14}$$

$$\frac{N}{n} = \frac{\sigma_A}{\sigma_M}\left(\frac{k_2 + 1}{k_1 + 1}\right) \quad \text{Equation 5-15}$$

Let $\lambda = \frac{N}{n}$, $\omega = \frac{\sigma_A}{\sigma_M}$ then,

$$\lambda = \omega\left(\frac{k_2 + 1}{k_1 + 1}\right) \quad \text{Equation 5-16}$$

For moment equilibrium of the rock beam at the lower abutment, the moment associated with the gravitational load must be balanced by the moments of the end thrusts. i.e.

$$\sum M_A = 0 \quad \text{Equation 5-17}$$

$$Tz = \frac{Ws}{8} \quad \text{Equation 5-18}$$

$$T = \frac{\gamma ts^2}{8z} \quad \text{Equation 5-19}$$

The distance between the line of the thrust at the abutment and that at the midspan (i.e. the moment arm z) is calculated as follows:

$$z = t - (\overline{x_A} + \overline{x_M}) \quad \text{Equation 5-20}$$

Given $\overline{x_A} = \frac{nt}{k_1+2}$, $\overline{x_M} = \frac{Nt}{k_2+2}$ then

$$z = t - nt\left[\frac{(k_1+1)(k_2+2)+\omega(k_1+2)(k_2+1)}{(k_1+1)(k_1+2)(k_2+2)}\right] \quad \text{Equation 5-21}$$

Let $\eta = \left[\frac{(k_1+1)(k_2+2)+\omega(k_1+2)(k_2+1)}{(k_1+1)(k_1+2)(k_2+2)}\right]$,

$$z = t(1 - n\eta) \quad \text{Equation 5-22}$$

Now let $T = T_A$, combine Equation 5-5 and Equation 5-19

$$\frac{\sigma_A nt}{k_1+1} = \frac{\gamma t s^2}{8z} \quad \text{Equation 5-23}$$

From Equation 5-22,

$$\frac{\sigma_A nt}{k_1+1} = \frac{\gamma t s^2}{8t(1-n\eta)} \quad \text{Equation 5-24}$$

$$\sigma_A = \frac{\gamma s^2(k_1+1)}{8nt(1-n\eta)} \quad \text{Equation 5-25}$$

The value of the eccentricity corresponding to thrust T_A and T_B are,

$$e_A = \frac{t}{2} - \overline{x_A} \quad \text{Equation 5-26}$$

Or

$$e_A = t\left[\frac{k_1+2-2n}{2(k_1+2)}\right] \quad \text{Equation 5-27}$$

$$e_M = \frac{t}{2} - \overline{x_M} \quad \text{Equation 5-28}$$

Or

$$e_M = t\left[\frac{k_2+2-2N}{2(k_2+2)}\right] \quad \text{Equation 5-29}$$

5.3 The Derivation of the Arch Length Equation

According to the principle that the internal compression of an arch will follow a parabolic profile when the load applied is uniformly distributed (Ambrose & Tripeny, 2012), the internal compression or thrust in the voussoir beam model will follow a parabolic profile as the only load is itself weight in the model, as shown in Figure 5-5. This parabolic profile passes through the centroids of the stress blocks at the abutment and midspan, and it can be represented as a smooth continuous curve in rectangular coordinates.

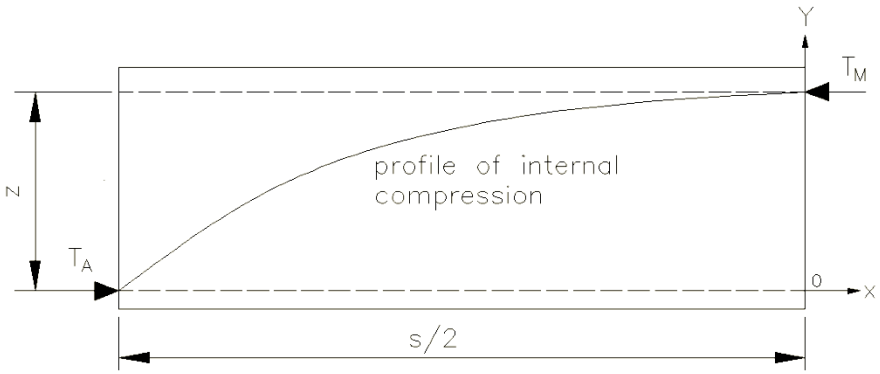

Figure 5-5 The Shape of the Linear Arch

Therefore, this parabolic arch profile can be expressed in the form

$$y = ax^2 + b \qquad \text{Equation 5-30}$$

The value of the constants, a and b, can be determined as follows:

When $x = 0$ then $y = z$

$$b = z \qquad \text{Equation 5-31}$$

When $x = -s/2$ then $y = 0$

$$a = -\frac{4z}{s^2} \qquad \text{Equation 5-32}$$

Hence the equation of the linear arch is

$$y = -\frac{4z}{s^2}x^2 + z \qquad \text{Equation 5-33}$$

Now the equation for the arch length is given by

$$l = \int \left[1 + \left(\frac{dy}{dx}\right)^2\right]^{1/2} dx \qquad \text{Equation 5-34}$$

But the total length of the arch is

$$L = 2l \qquad \text{Equation 5-35}$$

Then

$$L = 2\int_{-\frac{s}{2}}^{0}\left(1 + \frac{64z^2}{s^4}x^2\right)^{1/2} dx \qquad \text{Equation 5-36}$$

Integrating the above expression to obtain an exact solution is possible, but the result is complicated. Therefore, consider an approximate solution by expanding the integrand as a binomial Taylor series.

$$\left(1 + \frac{64z^2}{s^4}x^2\right)^{1/2} = 1 + \frac{1}{2}\left(\frac{64z^2x^2}{s^4}\right) + \left(\frac{-1}{8}\right)\left(\frac{64z^2x^2}{s^4}\right) + \cdots \qquad \text{Equation 5-37}$$

Now considering the first two terms only, Equation 5-36 can be written as follows:

$$L \approx 2\int_{-\frac{s}{2}}^{0}\left(1 + \frac{32z^2}{s^4}x^2\right)dx$$

$$\approx s + \frac{8z^2}{3s}$$

Hence, the approximate length of the parabolic arch line, *L*, can be expressed in terms of the lever arm (z) and the span (s) by:

$$L = s + \frac{8z^2}{3s} \qquad \text{Equation 5-38}$$

Now, in order to evaluate the relative error associated in deriving Equation 5-38, the exact solution to the arc length is calculated.

So from Equation 5-36 let

$$x = \left(\frac{s^2}{8z}\right)\tan\theta \qquad \text{Equation 5-39}$$

Therefore

$$dx = \left(\frac{s^2}{8z}\right)sec^2\theta d\theta \qquad \text{Equation 5-40}$$

So Equation 5-36 becomes

$$L = \left(\frac{s^2}{4z}\right)\int_{tan^{-1}(-\frac{4z}{s})}^{0} sec^3\theta d\theta \qquad \text{Equation 5-41}$$

Therefore, integrating the above expression results in the exact value of the arch length which is given by:

$$L_{exact} = \frac{s^2}{8z}\left\{\frac{4z}{\cos\left[tan^{-1}(\frac{4z}{s})\right]s} + \ln\left|\frac{1}{\cos\left[tan^{-1}(\frac{4z}{s})\right]} + \frac{4z}{s}\right|\right\} \qquad \text{Equation 5-42}$$

The relative error (R.E.) due to the approximation is calculated using the following expression:

$$R.E. = \frac{|L_{exact} - L|}{|L_{exact}|} \quad and\ L_{exact} \neq 0 \qquad \text{Equation 5-43}$$

By assuming a number of values for the lever arm (z) and span (s) the relative error due to the approximation can be evaluated.

Table 5-1 Relative Error due to Approximation

Span(s)/m	Lever Arm(z)/m	L/m	L_{exact}/m	R.E.
50	2	50.2133	50.2125	1.62E-05
100	4	100.4267	100.4250	1.62E-05
150	6	150.6400	150.6376	1.62E-05
200	8	200.8533	200.8501	1.62E-05
250	10	251.0667	251.0626	1.62E-05
300	12	301.2800	301.2751	1.62E-05

Clearly the magnitude of the relative error is on the order of 10^{-5}. Thus the approximate solution, as given by Equation 5-38, can be used to approximate the exact solution without significant loss in accuracy.

5.4 Derivation of Beam Shortening Equation

In order to determine the stability of voussoir beams against buckling failure, the horizontal shortening of the beam needs to be investigated first. Making use of the symmetry, only half of the voussoir beam is investigated. As shown in Figure 5-1, half of the voussoir beam is constrained by two non-uniform distributed stresses, one of them is at the lower abutment and the other is at the upper midspan. As the horizontal stress distributions in the internal vertical sections are unknown, an approximation method is proposed to determine the mean horizontal stress in the beam, and then the shortening can be known from the elastic relationship.

From the parabolic profile of internal thrust of voussoir beam in Figure 5-5-6, it is noticed that there is an intersection (point *u* in Figure 5-5-6) of the profile and the beam horizontal central line. So the thrust on this section is along the beam horizontal central line. A further assumption is made that there is uniform stress (σ_u) acting over this section. The average compressive stress in the beam will be estimated by the weighted mean of the average stresses between Au ($\boldsymbol{\sigma_{Au}}$) and uM ($\boldsymbol{\sigma_{uM}}$). This is validated from the physical testing which shows the entire beam is under compression except at the abutment and midspan joints.

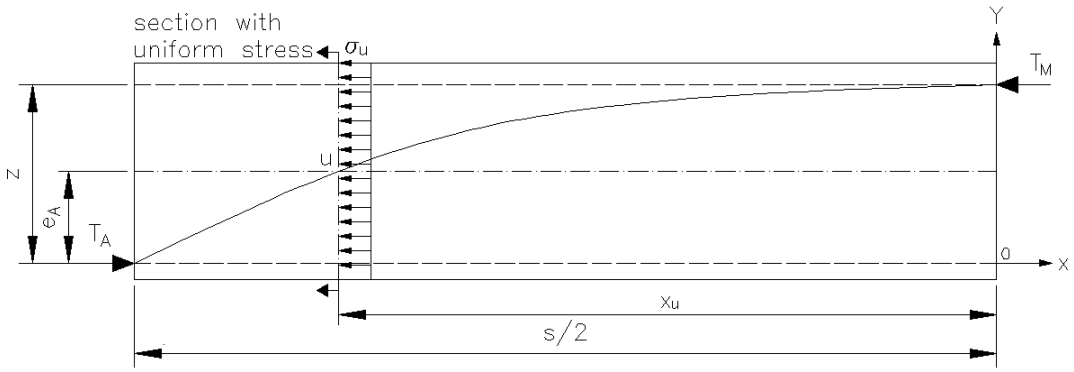

Figure 5-5-6 Compressive Stress Acting on the Arch Line

It is assumed that this section is at a distance "x_u" away from the midspan section. Therefore, the point 'u', as defined by the coordinate system in Figure 5-5-6, has the following coordinates:

$$u(x, y) = (-x_u, e_A) \quad \text{Equation 5-44}$$

From Equation 5-33, at point 'u' Equation 5-44 becomes,

$$e_A = -\frac{4z}{s^2} x_u{}^2 + z \quad \text{Equation 5-45}$$

The midspan thrust eccentricity (e_M) is

$$\mathrm{e_M} = \mathrm{z} - \mathrm{e_A} \quad \text{Equation 5-46}$$

$$\mathrm{e_M} = \mathrm{t}\left[\frac{k_2 + 2 - 2N}{2(k_2 + 2)}\right] \quad \text{Equation 5-47}$$

And given that

$$z = \mathrm{t}(1 - n\eta) \quad \text{Equation 5-48}$$

Then

$$x_u = \frac{s}{2}\left[\frac{k_2 + 2 - 2N}{2(k_2 + 2)(1 - n\eta)}\right]^{1/2} \quad \text{Equation 5-49}$$

Now the stress acting on the arch from point "A" to "u" is defined as

$$\sigma_{Au} = \frac{\sigma_A^{'} + \sigma_u}{2} \quad \text{Equation 5-50}$$

Similarly the stress acting on the arch from point "u" to "M" is defined as

$$\sigma_{uM} = \frac{\sigma_u + \sigma_M^{'}}{2} \quad \text{Equation 5-51}$$

Hence, the equivalent horizontal stress acting on the arch is

$$\sigma_{arch} = \left(\frac{\overline{Au}}{\overline{AM}}\right)\sigma_{Au} + \left(\frac{\overline{uM}}{\overline{AM}}\right)\sigma_{uM} \quad \text{Equation 5-52}$$

By Pythagorean Theorem,

$$\overline{Au} = \sqrt{\left(\frac{s}{2} - x_u\right)^2 + e_A^2} \quad \text{Equation 5-53}$$

$$\overline{uM} = \sqrt{{x_u}^2 + e_M^2} \quad \text{Equation 5-54}$$

$$\overline{AM} = \sqrt{\left(\frac{s}{2}\right)^2 + z^2} \quad \text{Equation 5-55}$$

Now, where the arch line intersects the horizontal center of the beam the stress is assumed to be uniformly distributed over the entire beam height and is given by

$$\sigma_u = \frac{T_u}{t} \quad \text{Equation 5-56}$$

From the beam equilibrium, $T_u = T$, combining Equation 5-5,

$$\sigma_u = \frac{\sigma_A n}{k_1 + 1} \quad \text{Equation 5-57}$$

The stress, σ_A', which is the stress acting at the intersection of the arch line and abutment is given by

$$\sigma_A' = \sigma_A\left(\frac{x_A}{nt}\right)^{k_1} \quad \text{Equation 5-58}$$

$$x_A = \left(\frac{k_1 + 1}{k_1 + 2}\right)nt \quad \text{Equation 5-59}$$

$$\sigma_A' = \sigma_A\left(\frac{k_1 + 1}{k_1 + 2}\right)^{k_1} \quad \text{Equation 5-60}$$

Similarly, at the midspan, the stress acting at the intersection of the arch line and abutment is given by

$$\sigma_M' = \sigma_M\left(\frac{k_2 + 1}{k_2 + 2}\right)^{k_2} \quad \text{Equation 5-61}$$

As $\sigma_A = \omega\sigma_M$

$$\sigma_M^{'} = \frac{\sigma_A}{\omega}\left(\frac{k_2+1}{k_2+2}\right)^{k_2} \qquad \text{Equation 5-62}$$

Now substituting Equation 5-50, Equation 5-51, Equation 5-53, Equation 5-54, Equation 5-55, Equation 5-57, Equation 5-60, Equation 5-62, into Equation 5-52,

$$\sigma_{arch} = \left[\frac{\left(s/2 - x_u\right)^2 + e_A^2}{(s/2)^2 + z^2}\right]^{1/2}\left\{\frac{\sigma_A}{2}\left[\left(\frac{k_1+1}{k_1+2}\right)^{k_1} + \frac{n}{k_1+1}\right]\right\} + \left[\frac{x_u{}^2 + e_M^2}{(s/2)^2 + z^2}\right]^{1/2}\left\{\frac{\sigma_A}{2}\left[\frac{1}{\omega}\left(\frac{k_2+1}{k_2+2}\right)^{k_2} + \frac{n}{k_1+1}\right]\right\}$$

Equation 5-63

Rearranging gives

$$\sigma_{arch} = \frac{\sigma_A}{2[(s/2)^2 + z^2]^{1/2}}\left\{\left[\left(s/2 - x_u\right)^2 + e_A^2\right]^{1/2}\left[\left(\frac{k_1+1}{k_1+2}\right)^{k_1} + \frac{n}{k_1+1}\right] + \left[x_u{}^2 + e_M^2\right]^{1/2}\left[\frac{1}{\omega}\left(\frac{k_2+1}{k_2+2}\right)^{k_2} + \frac{n}{k_1+1}\right]\right\}$$

Equation 5-64

$$\left(x_u{}^2 + e_M^2\right)^{1/2} = \left\{\frac{s^2}{4}\frac{(k_2+2-2N)}{2(k_2+2)(1-n\eta)} + \frac{t^2}{4}\left(\frac{k_2+2-2N}{k_2+2}\right)^2\right\}^{1/2} \qquad \text{Equation 5-65}$$

Rearranging gives

$$\left(x_u{}^2 + e_M^2\right)^{1/2} = \left\{\frac{s^2(k_2+2-2N)(k_2+2) + 2t^2(1-n\eta)(k_2+2-2N)^2}{8(k_2+2)^2(1-n\eta)}\right\}^{1/2} \qquad \text{Equation 5-66}$$

Now let

$$\rho_1 = \left[s^2(k_2+2-2N)(k_2+2) + 2t^2(1-n\eta)(k_2+2-2N)^2\right]^{1/2} \qquad \text{Equation 5-67}$$

Then

$$\left(x_u{}^2 + e_M^2\right)^{1/2} = \frac{\rho_1}{\left[8(k_2+2)^2(1-n\eta)\right]^{1/2}} \qquad \text{Equation 5-68}$$

$$\left[\left(s/2 - x_u\right)^2 + e_A^2\right]^{1/2} = \left\langle\left\{\frac{s}{2} - \frac{s}{2}\left[\frac{k_2+2-2N}{2(k_2+2)(1-n\eta)}\right]^{1/2}\right\}^2 + \left\{\frac{t[(k_2+2)(1-2n\eta)+2N]}{2(k_2+2)}\right\}^2\right\rangle^{1/2} \qquad \text{Equation 5-69}$$

Rearranging gives

$$\left[\left(s/2 - x_u\right)^2 + e_A^2\right]^{1/2} = \left\langle\frac{s^2(k_2+2)\left\{[2(k_2+2)(1-n\eta)]^{1/2} - (k_2+2-2N)^{1/2}\right\}^2}{8(k_1+2)^2(1-n\eta)} + \frac{2t^2(1-n\eta)[(k_2+2)(1-2n\eta)+2N]^2}{8(k_2+2)^2(1-n\eta)}\right\rangle^{1/2}$$

Equation 5-70

Now let

$$\rho_2 = \langle s^2(k_2+2)\{[2(k_2+2)(1-n\eta)]^{1/2} - (k_2+2-2N)^{1/2}\}^2 + 2t^2(1-n\eta)[(k_2+2)(1-2n\eta)+2N]^2\rangle^{1/2}$$

Equation 5-71

Then

$$\left[(S/2 - x_u)^2 + e_A^2\right]^{1/2} = \frac{\rho_2}{[8(k_2+2)^2(1-n\eta)]^{1/2}}$$

Equation 5-72

So substituting Equation 4-23 and 4-27 into Equation 4-19 results in the following expression for the average stress acting along the arch line:

$$\sigma_{arch} = \frac{\sigma_A}{2[(s/2)^2+z^2]^{1/2}}\left\{\frac{\rho_2}{[8(k_2+2)^2(1-n\eta)]^{1/2}}\left[\left(\frac{k_1+1}{k_1+2}\right)^{k_1} + \frac{n}{k_1+1}\right] + \frac{\rho_1}{[8(k_2+2)^2(1-n\eta)]^{1/2}}\left[\frac{1}{\omega}\left(\frac{k_2+1}{k_2+2}\right)^{k_2} + \frac{n}{k_1+1}\right]\right\}$$

Equation 5-73

$$\sigma_{arch} = \frac{\sigma_A}{2}\left[\frac{\begin{array}{c}\rho_1\{n\omega(k_1+2)^{k_1}(k_2+2)^{k_2}+(k_1+1)(k_1+2)^{k_1}(k_2+1)^{k_2}\}+\\ \rho_2\{n\omega(k_1+2)^{k_1}(k_2+2)^{k_2}+\omega(k_1+1)^{k_1+1}(k_2+2)^{k_2}\}\end{array}}{\omega\{(S/2)^2+t^2(1-n\eta)^2\}^{1/2}\{8(k_2+2)^2(1-n\eta)\}^{1/2}(k_1+1)(k_1+2)^{k_1}(k_2+2)^{k_2}}\right]$$

Equation 5-74

The elastic shortening of the arch is given by

$$\Delta L_{arch} = \left(\frac{\sigma_{arch}}{E_{beam}}\right)L$$

Equation 5-75

Where E_{beam} is the modulus of elasticity of the voussoir beam.

5.5 Derivation of the Displacement Equation along the Abutment

The horizontal thrust of the voussoir beam is resisted by the abutments, and resulted displacement of the abutments will influence the stability of voussoir beam. This section will examine the displacement of the abutment.

As was shown in Figure 5-7, the load distribution acting on the abutment is statically equivalent to a concentrated thrust acting at the centroid. So consider this concentrated thrust, T_A, to act on a vertical straight boundary, AB, of an infinitely large plate. Also considering any element, C, at a distance, r, from the point of application of the load which is subjected to a compression in the radial direction.

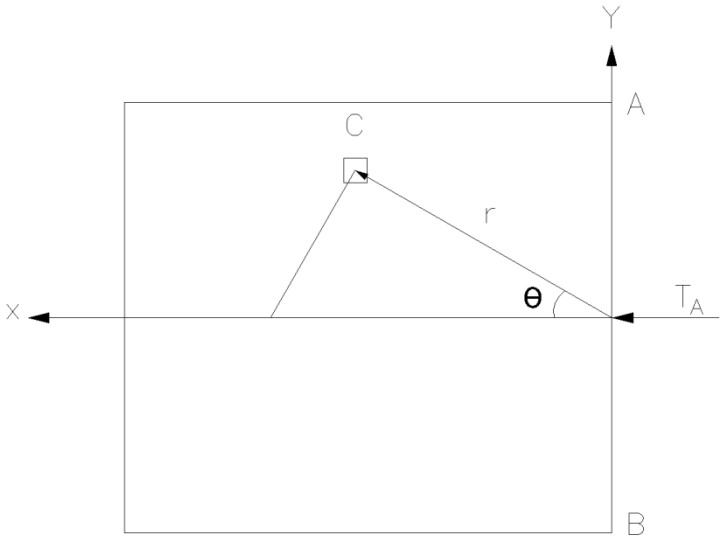

Figure 5-7 Concentrated Thrust Acting at a point of a straight boundary

To determine the stress components acting on element, C, requires the knowledge of the Airy Stress Function (φ) (Timoshenko, Goodier, & Aitf_c-Fer, 1970). Since element, C, is in compression, the stresses are assumed to be negative by elastic convention. So the stress function, in terms of polar coordinates, can be defined as follows: (Diederichs & Kaiser, 1999)

$$\varphi = -\frac{T_A}{\pi} r\theta \sin\theta \qquad \text{Equation 5-76}$$

It is necessary to verify that Equation 5-76 is an acceptable stress function. This requires that the stress function satisfy the equilibrium and compatibility conditions. The equilibrium conditions, in polar coordinates, are defined as follows:

$$\frac{\partial \sigma_r}{\partial r} + \frac{\partial \sigma_{r\theta}}{r\partial\theta} + \frac{\sigma_r - \sigma_\theta}{r\partial\theta} + R = 0 \qquad \text{Equation 5-77}$$

$$\frac{1}{r}\frac{\partial \sigma_\theta}{\partial\theta} + \frac{\partial \sigma_{r\theta}}{\partial r} + \frac{2\sigma_{r\theta}}{r} + S = 0 \qquad \text{Equation 5-78}$$

Where *R* is the body force per unit volume in the radial direction, *S* is the body force per unit volume in the tangential direction.

The compatibility equation in terms of polar coordinates is:

$$\left(\frac{\partial^2}{\partial r^2} + \frac{\partial}{r\partial r} + \frac{\partial^2}{r^2\partial\theta^2}\right)\left(\frac{\partial^2 \varphi}{\partial r^2} + \frac{\partial \varphi}{r\partial r} + \frac{\partial^2 \varphi}{r^2\partial\theta^2}\right) = 0 \qquad \text{Equation 5-79}$$

The stress components are defined as follows:

$$\sigma_r = \frac{\partial \varphi}{r\partial r} + \frac{\partial^2 \varphi}{r^2\partial\theta^2} \qquad \text{Equation 5-80}$$

$$\sigma_\theta = \frac{\partial^2 \varphi}{\partial r^2} \qquad \text{Equation 5-81}$$

$$\sigma_{r\theta} = -\frac{\partial}{\partial r}\left(\frac{\partial \varphi}{r\partial\theta}\right) \qquad \text{Equation 5-82}$$

Substituting Equation 5-76 into Equation 5-80, Equation 5-81 and Equation 5-82 yields the stress component in the radial and tangential directions.

$$\sigma_r = -\frac{2T_A \cos\theta}{\pi r} \qquad \text{Equation 5-83}$$

$$\sigma_\theta = 0 \qquad \text{Equation 5-84}$$

$$\sigma_{r\theta} = 0 \qquad \text{Equation 5-85}$$

This stress field automatically satisfies the equilibrium conditions given by Equation 5-77 and Equation 5-78 provided the body forces are zero.

The compatibility equation is satisfied by substituting Equation 5-76 into Equation 5-79

$$-\frac{4T_A\cos\theta}{\pi r^3}+\frac{2T_A\cos\theta}{\pi r^3}+\frac{2T_A\cos\theta}{\pi r^3}=0 \qquad \text{Equation 5-86}$$

Hence, the stress function, as given by Equation 5-76, satisfies both the equilibrium and compatibility equations respectively.

The strain components in polar coordinate are defined as follows.

$$\epsilon_r=\frac{\partial u_r}{\partial r} \qquad \text{Equation 5-87}$$

$$\epsilon_\theta=\frac{\partial u_\theta}{r\partial\theta}+\frac{u_r}{r} \qquad \text{Equation 5-88}$$

$$\epsilon_{r\theta}=\frac{\partial u_r}{r\partial\theta}+\frac{\partial u_\theta}{\partial r}-\frac{u_\theta}{r} \qquad \text{Equation 5-89}$$

According Hooke's law for plane stress,

$$\epsilon_r=\frac{\sigma_r-\nu\sigma_\theta}{E} \qquad \text{Equation 5-90}$$

$$\epsilon_\theta=\frac{\sigma_\theta-\nu\sigma_r}{E} \qquad \text{Equation 5-91}$$

$$\epsilon_{r\theta}=\frac{2(1+\nu)}{E}\sigma_{r\theta} \qquad \text{Equation 5-92}$$

Substituting equations 5-83, 5-84, 5-85, 5-87, 5-88 and 5-89 into equations 5-90, 5-91 and 5-92 yields the following:

$$\frac{\partial u_r}{\partial r}=-\frac{2T_A\cos\theta}{E\pi r} \qquad \text{Equation 5-93}$$

$$\frac{\partial u_\theta}{r\partial\theta}+\frac{u_r}{r}=\frac{2\nu T_A\cos\theta}{E\pi r} \qquad \text{Equation 5-94}$$

$$\frac{\partial u_r}{r\partial\theta}+\frac{\partial u_\theta}{\partial r}-\frac{u_\theta}{r}=0 \qquad \text{Equation 5-95}$$

Integrating Equation 5-93 yields the following:

$$u_r=-\frac{2T_A\cos\theta\ln r}{E\pi}+f(\theta) \qquad \text{Equation 5-96}$$

Where *f(ϴ)* is a function of *ϴ* only.

Substituting Equation 5-96 into the Equation 5-94 and integrating yields:

$$u_\theta = \frac{2\nu T_A \sin\theta}{E\pi} + \frac{2T_A \sin\theta \ln r}{E\pi} - \int f(\theta)d\theta + g(r) \qquad \text{Equation 5-97}$$

Where *g(r)* is a function of *r* only

Substituting Equation 5-96 and 5-97 into Equation 5-95 yields:

$$\int f(\theta)d\theta + f'(\theta) + rg'(r) - g(r) = \frac{-2T_A \sin\theta}{E\pi}(1-\nu) \qquad \text{Equation 5-98}$$

Equation 5-98 is satisfied by putting

$$g(r) = Hr \qquad \text{Equation 5-99}$$

$$f(\theta) = -\frac{(1-\nu)T_A\,\theta\sin\theta}{E\pi} + I\sin\theta + J\cos\theta \qquad \text{Equation 5-100}$$

Where *H*, *I*, and *J* are arbitrary constants to be determined from the conditions of constraint.

So substituting equation 5-99 and 5-100 into equations 5-96 and 5-97, the expressions for the displacements become:

$$u_r = -\frac{2T_A \cos\theta \ln r}{E\pi} - \frac{(1-\nu)T_A\,\theta\sin\theta}{E\pi} + I\sin\theta + J\cos\theta \qquad \text{Equation 5-101}$$

$$u_\theta = \frac{2\nu T_A \sin\theta}{E\pi} + \frac{2T_A \sin\theta \ln r}{E\pi} + \frac{(1-\nu)T_A \sin\theta}{E\pi} - \frac{(1-\nu)T_A\,\theta\cos\theta}{E\pi} + I\cos\theta - J\sin\theta + Hr \qquad \text{Equation 5-102}$$

Assume that the constraint condition of the semi-infinite plate is such that the points on the x-axis have no vertical displacement. i.e.

$$u_{\theta,\theta=0} = 0 \qquad \text{Equation 5-103}$$

$$I + Hr = 0 \qquad \text{Equation 5-104}$$

$$I = H = 0 \qquad \text{Equation 5-105}$$

The radial displacement on the x axis is

$$u_{r,\theta=0} = -\frac{2T_A \ln r}{E\pi} + J \qquad \text{Equation 5-106}$$

Assume that a point of x axis at a distance *d* from the origin does not move laterally, then from Equation 5-106 we find

$$J = \frac{2T_A \ln d}{E\pi} \qquad \text{Equation 5-107}$$

So substituting equations 5-102 and 5-105 into 5-98 and 5-99 yields the following solution for the displacement:

$$u_r = -\frac{2T_A \cos\theta \ln r}{E\pi} - \frac{(1-\nu)T_A\,\theta \sin\theta}{E\pi} + \frac{2T_A \ln d}{E\pi}\cos\theta \qquad \text{Equation 5-108}$$

$$u_\theta = \frac{2\nu T_A \sin\theta}{E\pi} + \frac{2T_A \sin\theta \ln r}{E\pi} + \frac{(1-\nu)T_A \sin\theta}{E\pi} - \frac{(1-\nu)T_A\,\theta\cos\theta}{E\pi} - \frac{2T_A \ln d}{E\pi}\sin\theta \qquad \text{Equation 5-109}$$

The lateral displacement on the straight boundary are obtained from Equation 5-109; Because u_θ is positive if the displacement is in the direction of increasing θ, the displacement is symmetrical with respect to x axis. The lateral displacement is as follow.

$$u_{\theta,\theta=\pi/2} = -u_{\theta,\theta=-\pi/2} = \frac{T_A}{E_{abut}\pi}\left[(1+\nu) - \ln\left(\frac{d}{r}\right)^2\right] \qquad \text{Equation 5-110}$$

Therefore, the deformation for a single abutment is given by:

$$\Delta L_{abut} = \frac{\sigma_A nt}{\pi(k_1+1)E_{abut}}\left[(1+\nu) - \ln\left(\frac{d}{r}\right)^2\right] \qquad \text{Equation 5-111}$$

And the deformation for two abutments is given by:

$$\Delta L_{abut} = \frac{2\sigma_A nt}{\pi(k_1+1)E_{abut}}\left[(1+\nu) - \ln\left(\frac{d}{r}\right)^2\right] \qquad \text{Equation 5-112}$$

It is reasonable to use the displacement at the lowest corner of the abutment as the displacement at this location has the most significant impact to the stability of voussoir beam, where

$$r = \overline{x_A} \qquad \text{Equation 5-113}$$

It is reasonable to assume the distance (d) is equal to nt, the width of the stress distribution at the abutment.

The Equation 5-112 is rewrite as

$$\Delta L_{abut} = \frac{2\sigma_A nt}{\pi(k_1 + 1)E_{abut}}[(1 + \nu) - \ln(k_1 + 2)^2]$$ Equation 5-114

5.6 Derivation of Beam Deflection Equation

Prior to any deflection of the voussoir beam, the centroid of the stress distribution (i.e. position of the initial thrust line) at the ends and center is located at points A and M respectively, as shown in Figure 5-8. As the beam begins to deflect it is assumed that:

i each half of the beam remains elastic and rotates about an end with no crushing of the beam material;

ii the compression arch is shortened by the deformation along the arch line and by the outward displacement of the abutments

iii the compression arch becomes flatter (i.e. the arch height decreases), and

iv the contact areas at the ends and center of the beam decrease causing the arch line to shift its position (i.e. the position of the new thrust line at the ends and center is located at points A_i and M_i respectively)

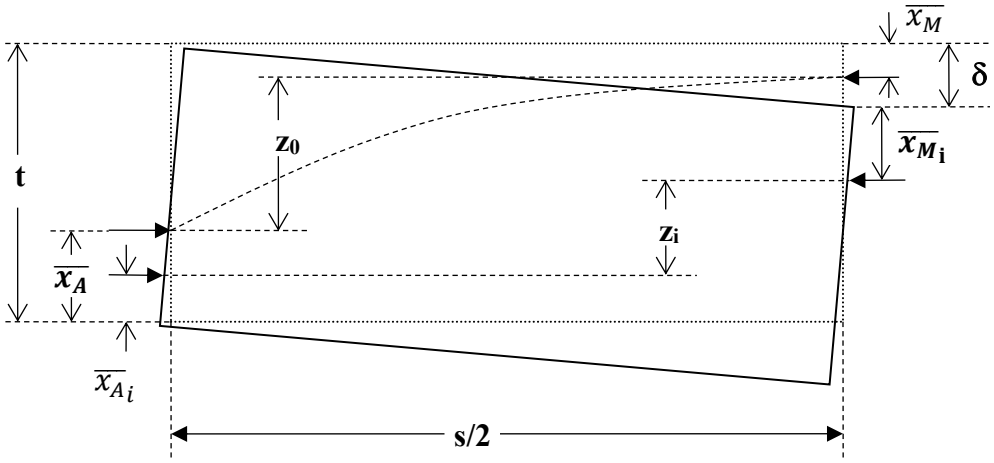

Figure 5-8 Deflection of Half Voussoir Beam

The relationship between the induced lateral thrusts and beam deflection is the assumption that the shape of the arch, which operates longitudinally throughout the beam, is parabolic in shape. As shown in Section 5.3, the approximate length of the parabolic arch is given by:

$$\mathbf{L = s + \frac{8}{3s} z^2} \qquad \textbf{Equation 5-115}$$

Let L_i and z_i be the arch length and the arch height at some deflected position of the voussoir beam respectively. Then the length of the arch line is given by:

$$\mathbf{L_i = s + \frac{8}{3s} z_i^2} \qquad \textbf{Equation 5-116}$$

Similarly, let L_{i+1} and z_{i+1} be the arch length and arch height at some incremental deflected position of the voussoir beam respectively. Then the length of the arch line, due to the incremental deflection, is given by:

$$\mathbf{L_{i+1} = s + \frac{8}{3s} z_{i+1}^2} \qquad \textbf{Equation 5-117}$$

Now, the incremental shortening of the arch, ΔL_i, results from the elastic compression of the roof beam as well as the elastic deformation of the abutments.

$$\mathbf{\Delta L_i = L_i - L_{i+1} = \Delta L_{arch} + 2\Delta L_{abut}} \qquad \textbf{Equation 5-118}$$

As stated in equation 4-30 and 6-37

$$\mathbf{\Delta L_{arch} = \left(\frac{\sigma_{arch}}{E_{beam}}\right) L} \qquad \textbf{Equation 5-119}$$

$$\mathbf{2\Delta L_{abut} = \frac{2\sigma_A nt}{\pi(k_1+1)E_{abut}}[(1+\nu) - \ln(k_1+2)^2]} \qquad \textbf{Equation 5-120}$$

$$\mathbf{\Delta L_i = \left(\frac{\sigma_{arch}}{E_{beam}}\right) L + \frac{2\sigma_A nt}{\pi(k_1+1)E_{abut}}[(1+\nu) - \ln(k_1+2)^2]} \qquad \textbf{Equation 5-121}$$

Thus, if the arch is shortened in compression by an incremental amount, ΔL_i, the new incrementally shortened arch height, z_{i+1}, is determined from the following expression:

$$\mathbf{z_{i+1} = \left[\frac{3s}{8}\left(\frac{8}{3s} z_i^2 - \Delta L_i\right)\right]^{1/2}} \qquad \textbf{Equation 5-122}$$

However, it should be noted that if the expression $\left(\frac{8}{3s}z_i^2 - \Delta L_i\right) = 0$ then $z_{i+1} = 0$ which implies that any further deflection of the voussoir beam will cause the moment arm to become negative thus making the resisting moment a moment assisting failure; consequently, failure will be an instantaneous buckling of the beam.

Assuming that the expression, $\left(\frac{8}{3s}z_i^2 - \Delta L_i\right) > 0$, then the deflection of the beam at its center is given by the following expression:

$$\delta_{i+1} = t - (\overline{x_A} + \overline{x_M})_{i+1} - z_{i+1} \qquad \text{Equation 5-123}$$

Where $\overline{x_A}$ and $\overline{x_M}$ are the centroids of the stress distributions at the abutments and center respectively. Therefore, Equation 5-123 becomes

$$\delta_{i+1} = t - \left(\frac{nt}{k_1+2} + \frac{Nt}{k_2+2}\right)_{i+1} - \left[\frac{3s}{8}\left(\frac{8}{3s}z_i^2 - \Delta L_i\right)\right]^{1/2} \qquad \text{Equation 5-124}$$

Since $N = \lambda n$, Equation 5-124 can be simplified to the following:

$$\delta_{i+1} = t\left[\frac{(k_1+2)(k_2+2) - n_{i+1}(k_2+2) - \lambda n_{i+1}(k_1+2)}{(k_1+2)(k_2+2)}\right] - \left[\frac{3s}{8}\left(\frac{8}{3s}z_i^2 - \Delta L_i\right)\right]^{1/2} \qquad \text{Equation 5-125}$$

Consequently, a complete explicit solution for the final deflection of the voussoir beam is not possible. An iterative procedure must therefore be used to evaluate the equilibrium states.

5.7 Estimation of Power Stress Distribution Parameters at the Abutment and Midspan

The following Table 5-2 was prepared according to the numerical modeling results in Chapter 4. The centroid distance ($\overline{x_A}$) was calculated according to Equation 5-8. The moment arm (z) was calculated according to Equation 5-20. Midspan deflection (δ) was from the numerical modeling result as shown in Chapter 4. All the parameters have been treated as dimensionless.

Table 5-2 Results of numerical modeling

No.	Span/Depth (s/t)	Transverse Load (Q/tE)	Deflection (δ/t)	Moment Arm (z/t)	Centroid distance at the abutment ($\overline{x_A}/t$)
1	3	3.58E-06	n/a	n/a	n/a
2	3	7.01E-06	n/a	n/a	n/a
3	6	3.58E-06	2.60E-03	0.788	0.085
4	6	7.01E-06	4.90E-03	0.791	0.0825
5	8	4.78E-06	7.20E-03	0.805	0.075
6	8	9.35E-06	1.40E-02	0.805	0.075
7	10	5.97E-06	8.50E-03	0.764	0.0925
8	10	1.17E-05	1.62E-02	0.789	0.0675
9	12	7.17E-06	1.68E-02	0.83	0.06
10	12	1.40E-05	3.56E-02	0.798	0.0925
11	15	8.96E-06	3.90E-02	0.547	0.12
12	15	1.75E-05	7.93E-02	0.539	0.1257
13	18	8.96E-06	6.53E-02	0.594	0.0725
14	18	1.75E-05	1.59E-01	0.584	0.0825
15	20	8.96E-06	n/a	n/a	n/a
16	20	1.75E-05	n/a	n/a	n/a

From Equation 5-19 and Equation 5-11,

$$\frac{\overline{x_M}}{\overline{x_A}} = \lambda \frac{k_1 + 2}{k_2 + 2} \qquad \text{Equation 5-126}$$

From the beam configuration shown in Figure 5-4,

$$\frac{\overline{x_M}}{\overline{x_A}} = \frac{t - (z + \overline{x_A})}{\overline{x_A}} \qquad \text{Equation 5-127}$$

Equation 5-127 can be written in

$$\frac{\overline{x_M}}{\overline{x_A}} = \frac{1 - (\frac{z}{t} + \frac{\overline{x_A}}{t})}{\frac{\overline{x_A}}{t}} \quad \text{Equation 5-128}$$

From the Table 5-2, the mean value of Equation 5-128 is 2.2, i.e.

$$\frac{\overline{x_M}}{\overline{x_A}} = 2.2 \quad \text{Equation 5-129}$$

Combining Equation 5-126 and Equation 5-129,

$$\lambda = 2.2\left(\frac{k_2 + 2}{k_1 + 2}\right) \quad \text{Equation 5-130}$$

As per both the physical and numerical investigation results in Chapter 3 and Chapter 4, the stress induced at the midspan is linear, and the stress induced at the abutment is nonlinear, can be represented by a quadratic function, i.e.

$$k_1 = 2 \quad \text{Equation 5-131}$$

$$k_2 = 1 \quad \text{Equation 5-132}$$

So,

$$\lambda = 1.7 \quad \text{Equation 5-133}$$

i.e.

$$\frac{N}{n} = 1.7 \quad \text{Equation 5-134}$$

Or

$$N = 1.7n \quad \text{Equation 5-135}$$

As

$$N \leq 1$$ Equation 5-136

$$n \leq 0.58$$ Equation 5-137

5.8 Voussoir Beam Analysis Procedure

From Equation 5-15, the following equation can be obtained.

$$\omega = \frac{\sigma_A}{\sigma_M} = 2.6 \qquad \text{Equation 5-138}$$

i.e.

$$\frac{\sigma_A}{\sigma_M} = 2.6 \qquad \text{Equation 5-139}$$

This is close to the numerical modeling result as in Chapter 5. So, the maximum stress in a voussoir beam (σ_{max}) is the maximum stress induced at abutment, σ_A. i.e.

$$\sigma_{max} = \sigma_A \qquad \text{Equation 5-140}$$

From Equation 5-25, the maximum stress induced in a voussoir beam is:

$$\sigma_A = \frac{3\gamma s^2}{8zn} \qquad \text{Equation 5-141}$$

i.e.

$$\sigma_{max} = \frac{3\gamma s^2}{8zn} \qquad \text{Equation 5-142}$$

And

$$\eta = 0.8 \qquad \text{Equation 5-143}$$

According to Equation 5-24,

$$z = t(1 - 0.8n) \qquad \text{Equation 5-144}$$

The Equation 5-67 can be rewritten as

$$\rho_1 = [3s^2(3 - 3.4n) + 2t^2(1 - 0.8n)(3 - 3.4n)^2]^{1/2} \quad \text{Equation 5-145}$$

The Equation 5-71 can be rewritten as

$$\rho_2 = \{3s^2[9 - 8.2n - 2(6 - 4.8n)^{1/2}(3 - 3.4n)^{1/2}] + 2t^2(1 - 0.8n)(3 - 1.4n)^2\}^{1/2} \quad \text{Equation 5-146}$$

The Equation 5-64 can be rewritten as

$$\sigma_{arch} = \frac{\sigma_A}{2}\left[\frac{\rho_1(124.8n+96)+\rho_2(124.8n+210.6)}{210.6\left[\left(s/2\right)^2+t^2(1-0.8n)^2\right][72(1-0.8n)]^{1/2}}\right] \quad \text{Equation 5-147}$$

The Equation 5-114 can be rewritten as

$$\Delta L_{abut} = \frac{2\sigma_A nt}{3\pi E_{abut}}[(1 + \nu) - 2.8] \quad \text{Equation 5-148}$$

The Equation 5-121 can be rewritten as

$$\Delta \mathbf{L} = \left(\frac{\sigma_{arch}}{E_{beam}}\right) L + \frac{2\sigma_A nt}{3\pi E_{abut}}[(1 + \nu) - 2.8] \quad \text{Equation 5-149}$$

In order to find the equilibrium position of the beam, the minimization of the σ_{max}, the maximum induced stress of a voussoir beam is taken as the equilibrium solution. Base on the theoretical analysis in the previous sections, and reference to the voussoir beam analysis procedure proposed by Diederichs and Kaiser (Diederichs & Kaiser, 1999), the following voussoir beam analysis procedure is proposed.

The iteration procedure is shown in Figure 5-9 Flow chart for determination of stability and deflection of a voussoir beam. The flow chart was separated into two parts as shown in Figure 5-10 and Figure 5-11.

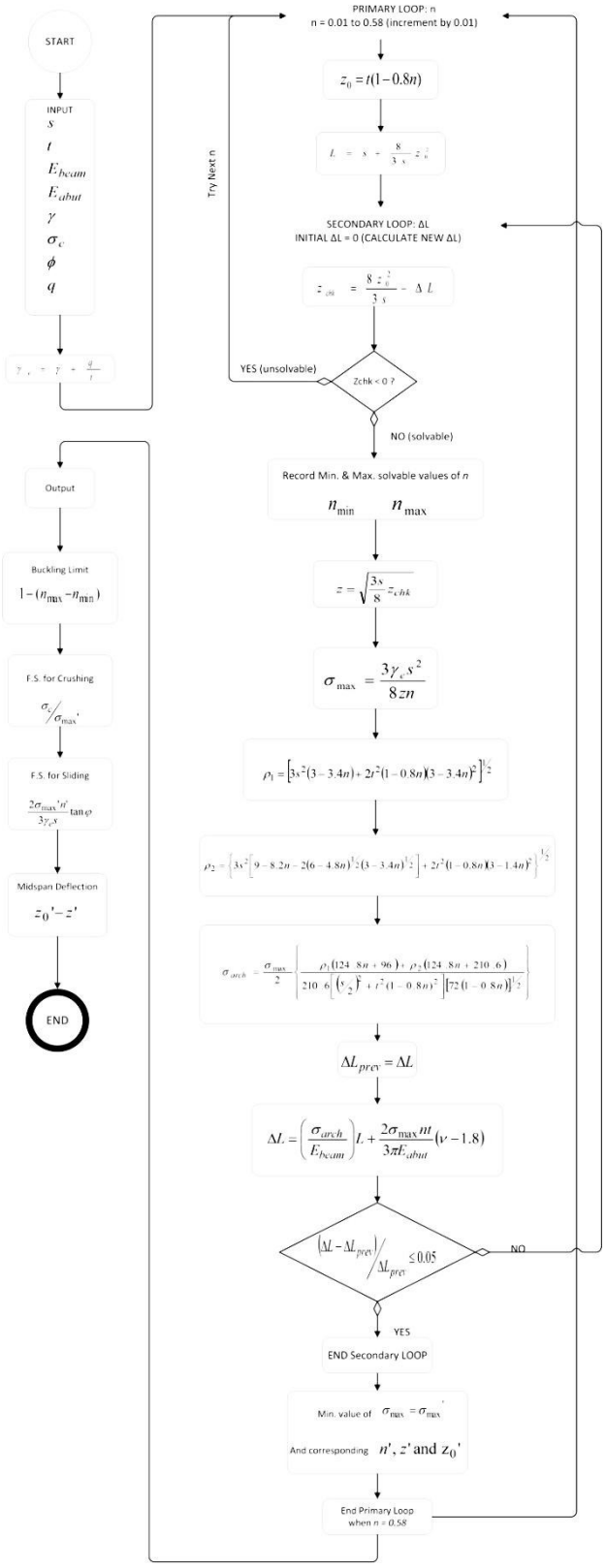

Figure 5-9 Flow chart for determination of stability and deflection of a voussoir beam

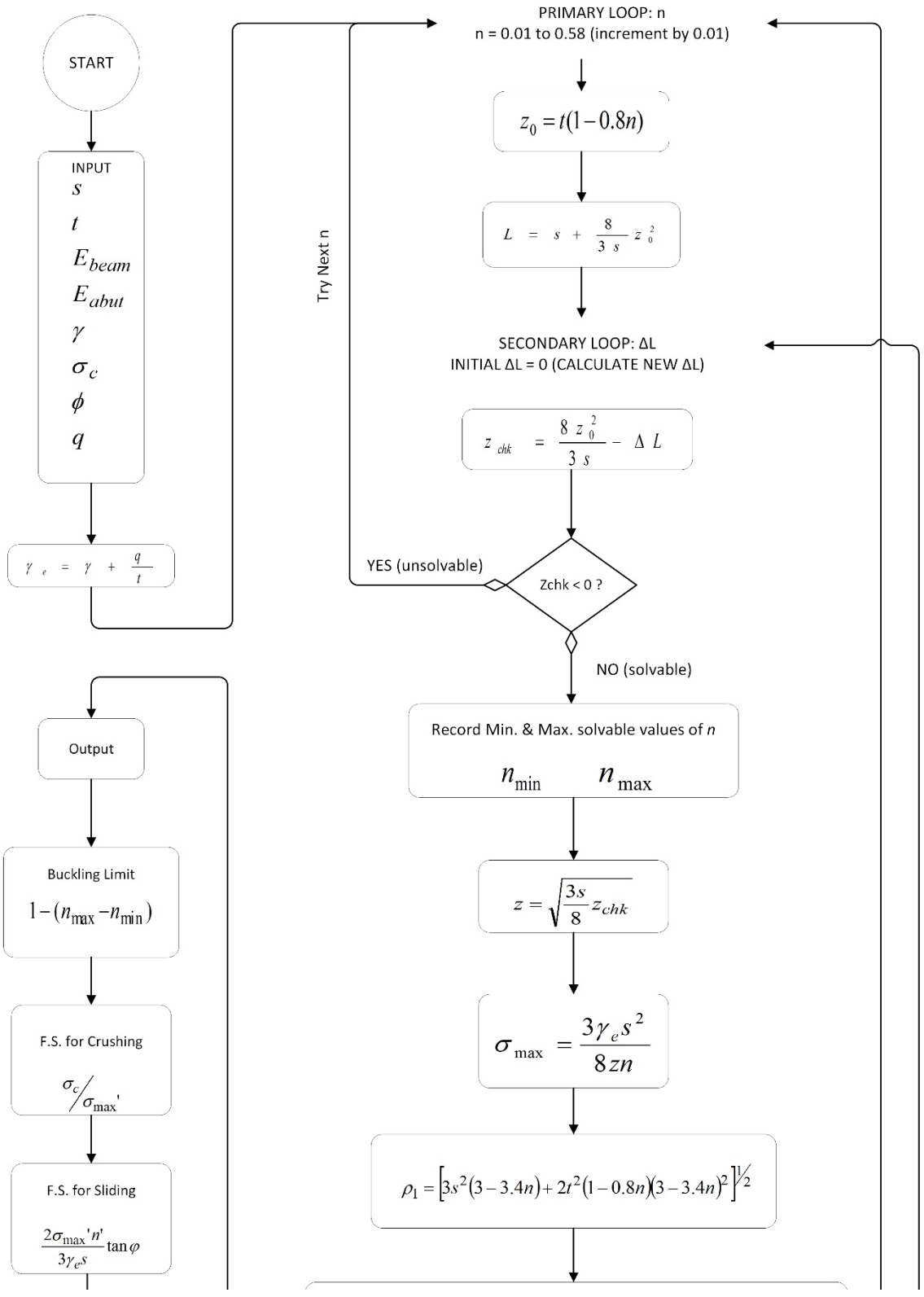

Figure 5-10 Flow chart for determination of stability and deflection of a voussoir beam - Part A

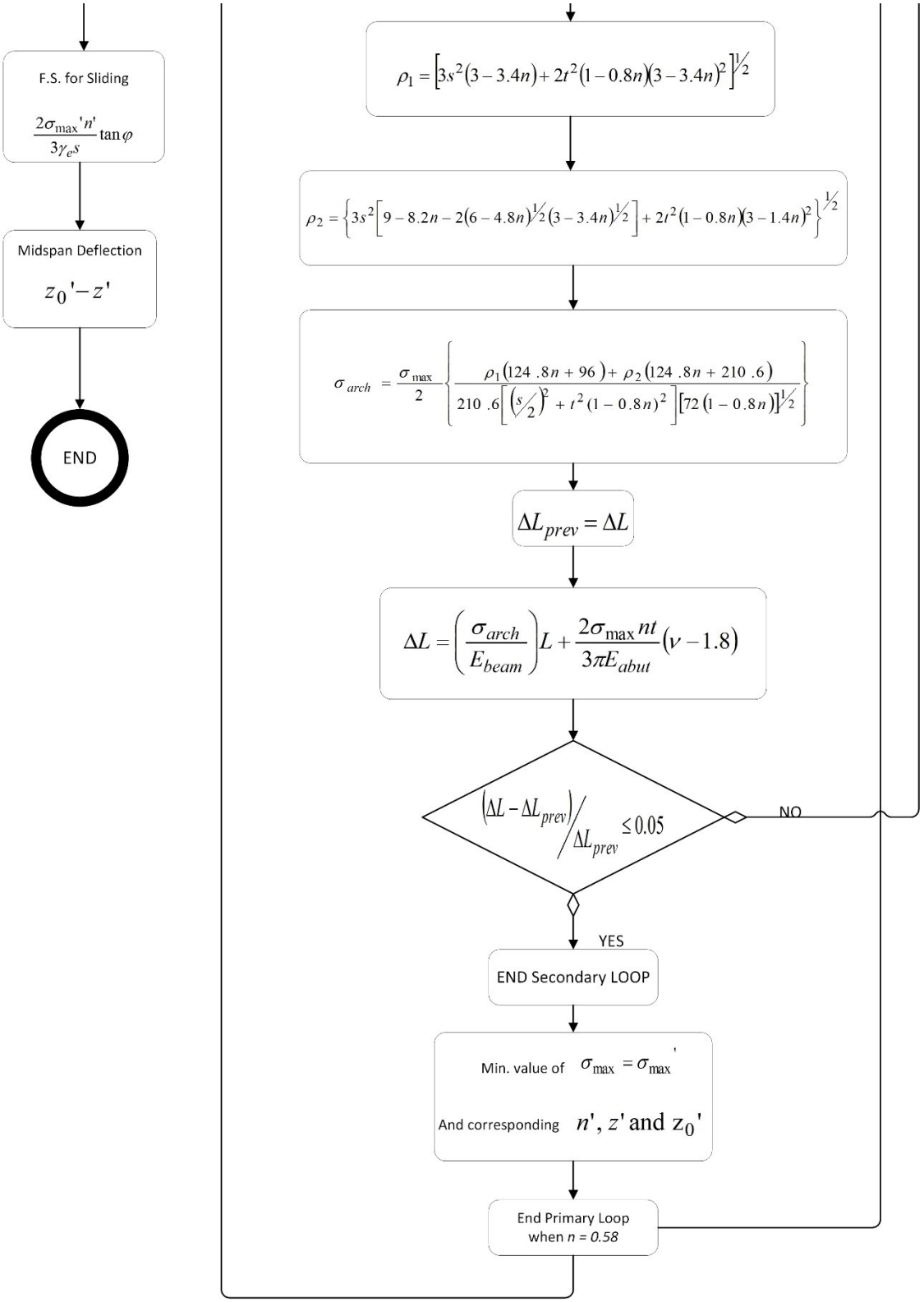

Figure 5-11 Flow chart for determination of stability and deflection of a voussoir beam - Part B

5.9 Summary

Starting from a generalized form of stress distribution at both midspan and abutment, the equations for centroids and thrust, moment arm, arch length, beam shortening, abutment displacement were derived. It was found, and iteration procedure is needed to solve the voussoir beam structure. Based on the findings in physical and numerical investigations, and referenced to previous research, an iteration procedure was provided to determine the stability of voussoir beam and midspan deflection.

References

Ambrose, J. E., & Tripeny, P. (2012). Building structures / james ambrose, patrick tripeny Hoboken, N.J.: Wiley, 2012; 3rd ed.

Diederichs, M., & Kaiser, P. (1999). Stability of large excavations in laminated hard rock masses: The voussoir analogue revisited. International Journal of Rock Mechanics and Mining Sciences, 36(1), 97-117. doi:10.1016/S0148-9062(98)00180-6

Timoshenko, S., Goodier, J. N., & Aitf_c-Fer. (1970). Theory of elasticity (3dth ed.). New York: McGraw-Hill.

6 Application of Voussoir Beam Theory on Prediction of the Mechanical Behavior of Segmental Precast Concrete Liner Stress Riser

6.1 Introduction

The segmental precast concrete liners (SPCL) are widely used in soft ground tunneling by Tunnel Boring Machine (TBM). The segmental liners were continuously installed during tunneling. Most of time, this is the only liner to be installed, i.e. one pass lining. There is a long history of application of segmental liners in the construction of storm and sanitary tunnels by City of Edmonton. A storm tunnel under construction by City of Edmonton is shown in Figure 6-1.

Figure 6-1 A Strom Tunnel under Construction Using Segmental Concrete Liner in Edmonton

6.1.1 Structure of the Segmental Concrete Liner used in Edmonton

The internal diameter of the segmental liners used by City of Edmonton ranges from 2340mm to 4040mm. And the wall thickness varies from 110mm to 216mm. A pre-banded segment liner is shown in Figure 6-2. The segmental liner used in the case project has an internal diameter of 2940mm. The structural drawing of the liner was shown in Figure 6-3 and Figure 6-4. To be concise, the drawing for Type A segment was included as the only difference to Type B segments is the ends.

A minimal amount of reinforcing steel is placed in precast concrete segment liners to assist in resisting the forces and moments that develop during shipping, handling and erection. The reinforcing quantities placed normally are less than the minimums required by CSA for reinforced concrete. The liner segments are designed for the factored axial forces and moments between the longitudinal joints or stress risers using the provisions of CSA (CSA, 2014).

Figure 6-2 Pre-banded Segmental Liner

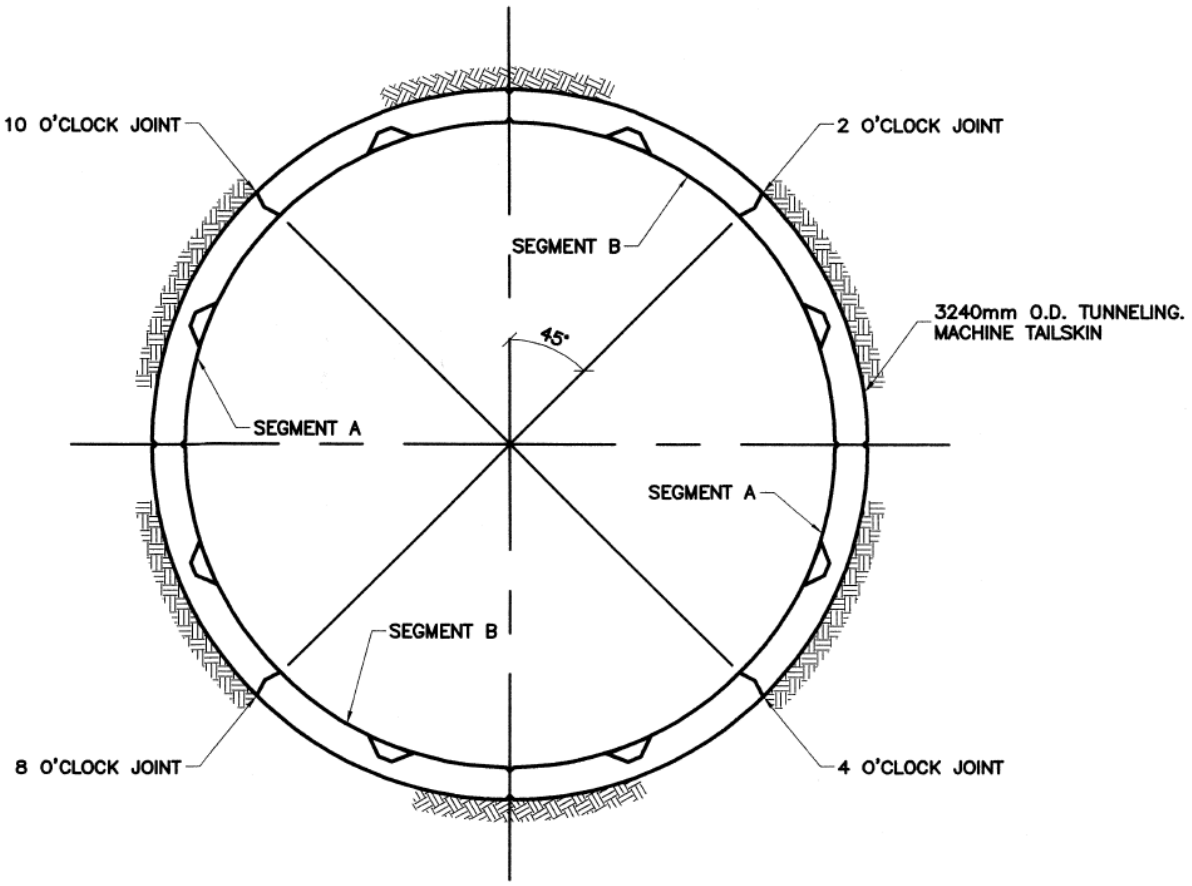

Figure 6-3 A full ring Segment Concrete Liner

As shown in Figure 6-3, for the segment at the crown of tunnel, the longitudinal joints between segments locate at angular positions of 45° and 135°. The stress riser of the segment at the tunnel crown locates at angular position of 90°. The stress riser is shown as 'F' in Figure 6-4.

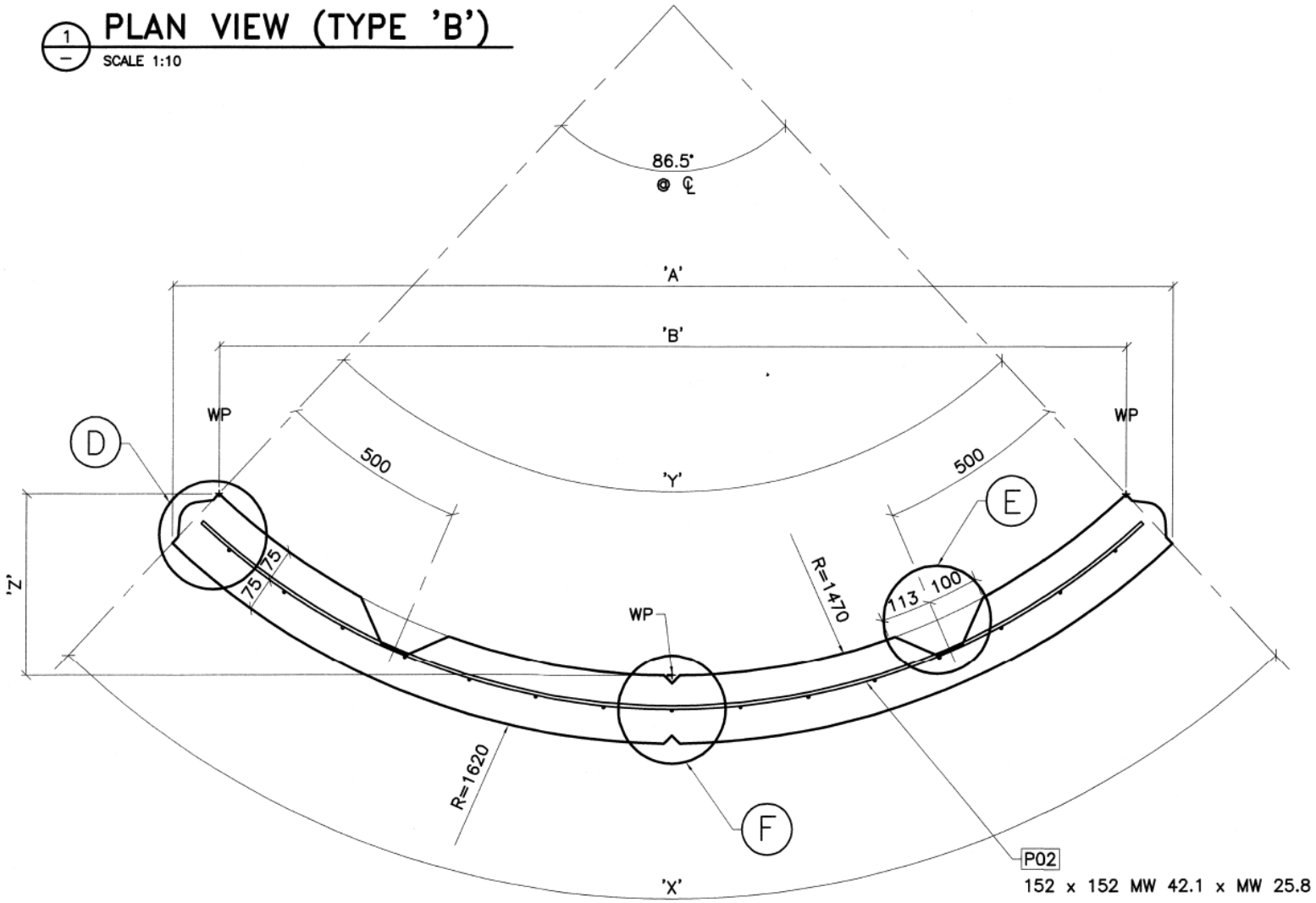

Figure 6-4 Plan View of Segment Type 'B'

6.1.2 Mechanical Behavior of Stress Riser

The tunnel liner should be strong in its capacity to resist normal forces and flexible in bending. For segmental concrete liner, the flexibility in circumferential bending is provided by knuckle joints between segments and enhanced by stress risers. During the interaction of soil and segment liner, there is elliptical deformation in the circular segment liners installed. The stress risers will have hair cracks after installation which will increase the liner flexibility. As a result, there is no bending moment in the liner after equilibrium state reached.

When hair cracks happened at the stress riser in the tunnel, there is always a safety concern in the field. The existing segmental design method couldn't provide the stress distribution at the stress riser. The risk of compressive failure at the stress riser cannot be evaluated. If there is compressive failure at the stress riser, tunnel reinforcement measures should be taken. Because of the uncertainty of the compressive stress distribution at stress riser at the crown of tunnel, reinforcement measures were taken when there are hair cracks if field worker required. For the case project completed by City of Edmonton, tunnel reinforcement measures including circular steel ribs and steel straps were installed to "reinforce" the segment liner after hair crack was found in stress riser, as shown Figure 6-5. In the following, both the existing segmental design method and voussoir beam theory will be applied to analyze the segment liner under short term loading for the case project. The radial displacement at stress riser derived from existing solution and voussoir beam theory was used to compare the two solutions.

Figure 6-5 Hair Crack at Stress Riser and Reinforcements (Circular Steel Ribs and Straps) Installed

6.2 Determine Mechanical Behavior of Stress Riser

6.2.1 Short Term Ground Loading

In this analysis, only the mechanical behavior of stress riser under short term loading is considered. As stated in Section 6.1.1, there is no bending moment in the segmental liner during long term loading as the liner is relatively flexible. The loading condition will be different from short term loading.

The case project shown in Figure 6-5 is a storm tunnel with an inside diameter of 2940mm and outside diameter of 3240mm. The geotechnical parameters and the tunnel parameters were presented in Table 6-1 and Table 6-2 respectively. The tunnel is located in clay till.

Table 6-1 Geotechnical Parameters

Depth Below Ground (m)	Soil Type	Bulk Unit Weight γ, kN/m^3	Effective Friction Angle (degrees) ϕ'	Coefficient of Earth Pressure at rest, k_o	Young's Modulus E_s, MPa	Poisson's Ratio, v_s
0-8	Fill/Clay/ Clay Till	20	20	0.65	50	0.45
8-14	Sand	20	26	0.56	100	0.35
14-17	Clay Till	20	22	0.62	70	0.40
Below 17	Bedrock	21	25	0.58	200	0.40

Table 6-2 Tunnel Parameters

Outside Diameter of Tunnel, D, m	Radius of the tunnel, R, m	Thickness of Liner, t, m	Depth of Ground at Tunnel Crown, m	Depth of Ground at Tunnel Spring line, H_o, m	Depth of Ground at Tunnel Invert, m	Young's Modulus of the Liner E_l, MPa	Poisson's Ratio of the Liner, v_l
3.24	1.62	0.15	14.5	16.12	17.59	30,000	0.15

As suggested in the geotechnical report, the vertical pressure, P_v, and horizontal pressure, P_h, can be determined from the equations below.

$$P_v = 2.5\gamma D \quad \text{Equation 6-1}$$

$$P_h = k_o P_v \quad \text{Equation 6-2}$$

According to the parameters in Table 6-1 and Table 6-2,

$$P_v = 162kPa \quad \text{Equation 6-3}$$

$$P_h = 100.4kPa \quad \text{Equation 6-4}$$

6.2.2 Analysis the mechanical behavior of stress riser using existing method

For deep tunnels with depth to diameter ratios greater than 4 or 5, a method to determine moments, axial forces and displacement is presented by Ranken (Ranken et al., 1978). For the tunnel to be analyzed, the depth to diameter ratio is:

$$\frac{H_0}{D} = 5 \quad \text{Equation 6-5}$$

So, the method is applicable. The solution assumes that the loads develop on the liner as the excavation proceeds and there is full slip between the surrounding soil and the liner. The solution is as follows:

A flexibility ratio is defined to measure of the stiffness of the surrounding soil to the flexural stiffness of the tunnel liner. The flexibility ratio, *F*, is calculated from

$$F = \left(\frac{E_s}{E_l}\right)\left(\frac{R}{t}\right)^3\left[\frac{2\left(1-\vartheta_l{}^2\right)}{1+\vartheta_s}\right] \quad \text{Equation 6-6}$$

From the parameters in Table 6-1 and Table 6-2,

$$F = 4.10 \quad \text{Equation 6-7}$$

A compressibility ratio is also defined to measure of the extensional stiffness of the surrounding soil to the extensional stiffness of the tunnel liner. The compressibility ratio, C, is calculated from

$$C = \left(\frac{E_s}{E_l}\right)\left(\frac{R}{t}\right)\left[\frac{1-\vartheta_l{}^2}{(1+\vartheta_s)(1-2\vartheta_s)}\right] \quad \text{Equation 6-8}$$

From the parameter in Table 6-1 and Table 6-2,

$$C = 0.09 \quad \text{Equation 6-9}$$

To simplify the analysis, two parameters, L_f *and* J_f, were defined as follow:

$$L_f = \frac{(1-2\vartheta_s)C}{1+(1-2\vartheta_s)C} \quad \text{Equation 6-10}$$

$$J_f = \frac{F+(1-\vartheta_s)}{2F+(5-6\vartheta_s)} \quad \text{Equation 6-11}$$

From the parameter in Table 6-1 and Table 6-2,

$$L_f = 0.02 \quad \text{Equation 6-12}$$

$$J_f = 0.44 \quad \text{Equation 6-13}$$

The radial soil pressure on the tunnel liner, σ_r, is

$$\sigma_r = \frac{P_v}{2}[(1+K_o)(1-L_f) - 3(1-K_o)(1-2L_f)\cos 2\theta] \quad \text{Equation 6-14}$$

From the parameters in Table 6-1 and Table 6-2,

$$\sigma_r = 128.60 - 88.65\cos 2\theta \quad \text{Equation 6-15}$$

The radial and tangential displacement of the tunnel liner, u_r and v_θ, respectively, are

$$u_r = \frac{P_v R}{2}\left(\frac{1+\vartheta_s}{E_s}\right)\left[\left((1+k_o)L_f - (1-k_o)(2F)(1-2J_f)\cos 2\theta\right)\right] \quad \text{Equation 6-16}$$

$$\vartheta_\theta = \frac{P_v R}{2}\left(\frac{1+\vartheta_s}{E_s}\right)\left[\left((1-k_o)(F)(1-2J_f)\,sin\,2\theta\right)\right] \quad \text{Equation 6-17}$$

From the parameters in Table 6-1 and Table 6-2,

$$u_r = 0.00009 - 0.00098\,cos\,2\theta \quad \text{Equation 6-18}$$

$$\vartheta_\theta = 0.00049 sin\,2\theta \quad \text{Equation 6-19}$$

The symbols and sign conventions for axial force P_θ, shear force V_θ and moment M_θ in the tunnel liner are shown in Figure 6-6.

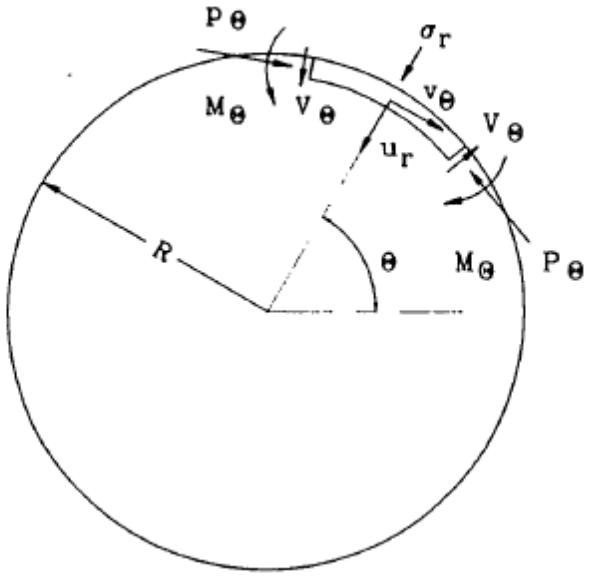

Figure 6-6 Symbols and sign convention for existing analyze solution (Montgomery & Eisenstein, 1995)

The equations for axial forceP_θ, shear force V_θ and moment M_θ in the tunnel liner are:

$$P_\theta = \frac{\gamma H_o R}{2}\left[\left((1+k_o)(1-L_f) + (1-k_o)(1-2J_f)\,cos\,2\theta\right)\right] \quad \text{Equation 6-20}$$

$$V_\theta = \frac{\gamma H_o R}{2}\left[\left((1-k_o)(1-2J_f)\,sin\,2\theta\right)\right] \quad \text{Equation 6-21}$$

$$M_\theta = \frac{\gamma H_o R^2}{2}\left[\left((1+k_o)\frac{L_f}{6F} + (1-k_o)(1-2J_f)\cos 2\theta\right)\right] \quad \text{Equation 6-22}$$

From the parameters in Table 6-1 and Table 6-2,

$$P_\theta = 208.33 + 5.98\cos 2\theta \quad \text{Equation 6-23}$$

$$V_\theta = 5.98\sin 2\theta \quad \text{Equation 6-24}$$

$$M_\theta = 0.28 + 9.69\cos 2\theta \quad \text{Equation 6-25}$$

The results from existing method are presented in Table 6-3 . The angular positions at 45°, 90° and 135° are marked as in red. The angular positions 45° and 135° are the locations for longitudinal joints. And the angular position 90° is the location of stress riser at the crown. The distribution of axial force in the liner and the radial displacement of the liner are presented in Figure 6-7 and Figure 6-8 respectively.

Table 6-3 Calculation Results from existing method

Angular Position /degree	Sigma-r /kPa	u-r /m	Niu-theta /m	P-theta /kN/m	V-theta /kN/m	M-theta /kN.m/m
0	39.95	-0.0009	0	214.31	0	9.97
15	51.826828	-0.0008	0.000245	213.51	2.99	8.671788
30	84.274932	-0.0004	0.000424	211.32	5.1788	5.125007
45	128.59988	9E-05	0.00049	208.33	5.98	0.280013
60	172.92486	0.00058	0.000424	205.34	5.1788	4.564985
75	205.37305	0.00094	0.000245	203.15	2.99	8.111775
90	217.25	0.00107	1.3E-09	202.35	2E-05	-9.41
105	205.37329	0.00094	-0.00024	203.15	-2.99	8.111801
120	172.92527	0.00058	-0.00042	205.34	5.1788	-4.56503
135	128.60035	9E-05	-0.00049	208.33	-5.98	0.279961
150	84.27534	-0.0004	-0.00042	211.32	5.1788	5.124963
165	51.827064	-0.0008	-0.00025	213.51	-2.99	8.671763
180	39.95	-0.0009	-2.6E-09	214.31	-3E-05	9.97
195	51.826593	-0.0008	0.000245	213.51	2.99	8.671814
210	84.274525	-0.0004	0.000424	211.32	5.1788	5.125052
225	128.59941	9E-05	0.00049	208.33	5.98	0.280064
240	172.92446	0.00058	0.000424	205.34	5.1789	4.564941
255	205.37282	0.00094	0.000245	203.15	2.99	-8.11175
270	217.25	0.00107	3.9E-09	202.35	5E-05	-9.41
285	205.37352	0.00094	-0.00024	203.15	-2.99	8.111827
300	172.92568	0.00058	-0.00042	205.34	5.1788	4.565074
315	128.60082	9E-05	-0.00049	208.33	-5.98	0.27991
330	84.275747	-0.0004	-0.00042	211.32	5.1789	5.124918
345	51.827299	-0.0008	-0.00025	213.51	2.9901	8.671737
360	39.95	-0.0009	-5.2E-09	214.31	-6E-05	9.97

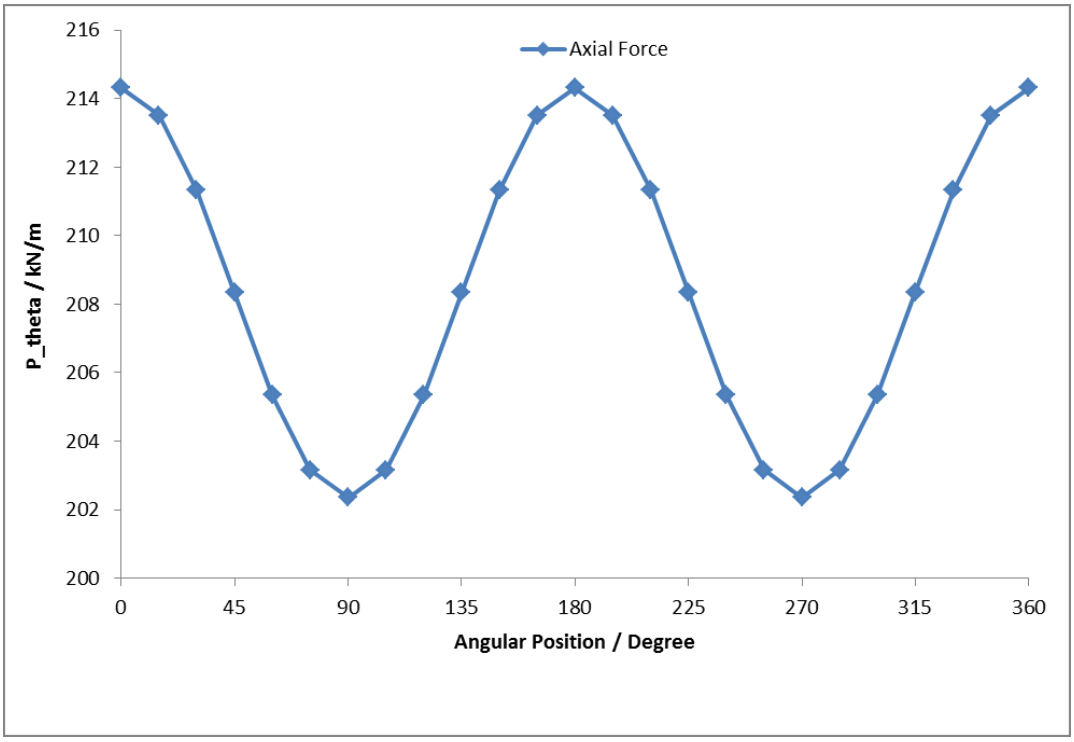

Figure 6-7 Axial Force in Segmental Liner

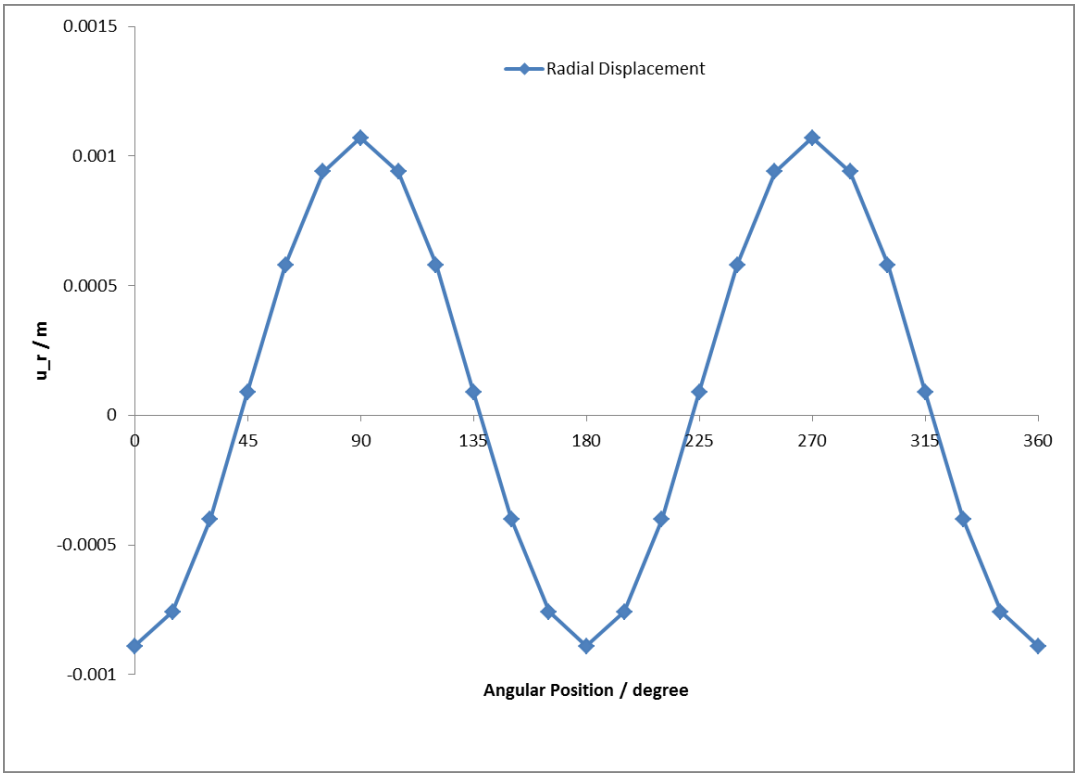

Figure 6-8 Radial Displacement in Segmental Liner

However, the stress distribution at the stress riser cannot be derived from this closed form solution. Voussoir beam theory developed in previous chapters will be applied in following section.

6.2.3 Application of Voussoir Beam Theory

Voussoir beam theory developed through investigation in previous chapter was applied to analyze the mechanical behavior of stress riser at the tunnel crown. The segment at tunnel was analyzed as a voussoir beam, as shown in Figure 6-9. Several approximations/assumptions were made for the analysis.

1) The span of the voussoir beam, s, was taken as the chord length of the segment. The chord of the segment is shown as "A" in Figure 6-4.
2) The thickness of the voussoir beam, t, was taken as the distance from the chord to crown of tunnel. The thickness of voussoir model is shown as "Z" in Figure 6-4.
3) As the present of horizontal pressure and from analyzed result on the radial displacement in previous section, there is very minimum displacement at the two longitudinal joints which is the abutment joint in voussoir beam model. The abutment was assumed to be rigid, i.e., the Young's modulus of the abutment is infinite.
4) As the tunnel liners have relatively small radii of curvature and are convex outward into the surrounding soil, and there are no voids behind the liner, there will be no bucking failure and slide failure at the joints for the voussoir model.
5) The short term loading on the liner is uniformly distributed. If the loading is not uniformly distributed, as the segmental liner is a flexible structure. The rotation/deflection happened at the joint/stress riser with higher stress magnitude will

redistribute the stress to be close to be evenly distributed. So this assumption can be applied as well.

The input parameters required for voussoir beam analysis as shown Figure 5-9 are presented in the Table 6-4.

Table 6-4 Parameters for Voussoir beam analysis

Span of Voussoir Beam S /m	Thickness of Voussoir Beam t /m	Modulus of Voussoir Beam E_{beam}/Mpa	Modulus of the Abument E_{abut}/MPa	Unit Weight of voussoir beam γ / kN/m^3	External loading q / kPa	Compressive strength of voussoir beam σ_c /MPa
2.22	0.399	30,000	Infinite	23.5	162	40

According the analysis procedure shown in Figure 5-9, the analyze result was obtained using an Excel sheet. The results are shown in Table 6-5.

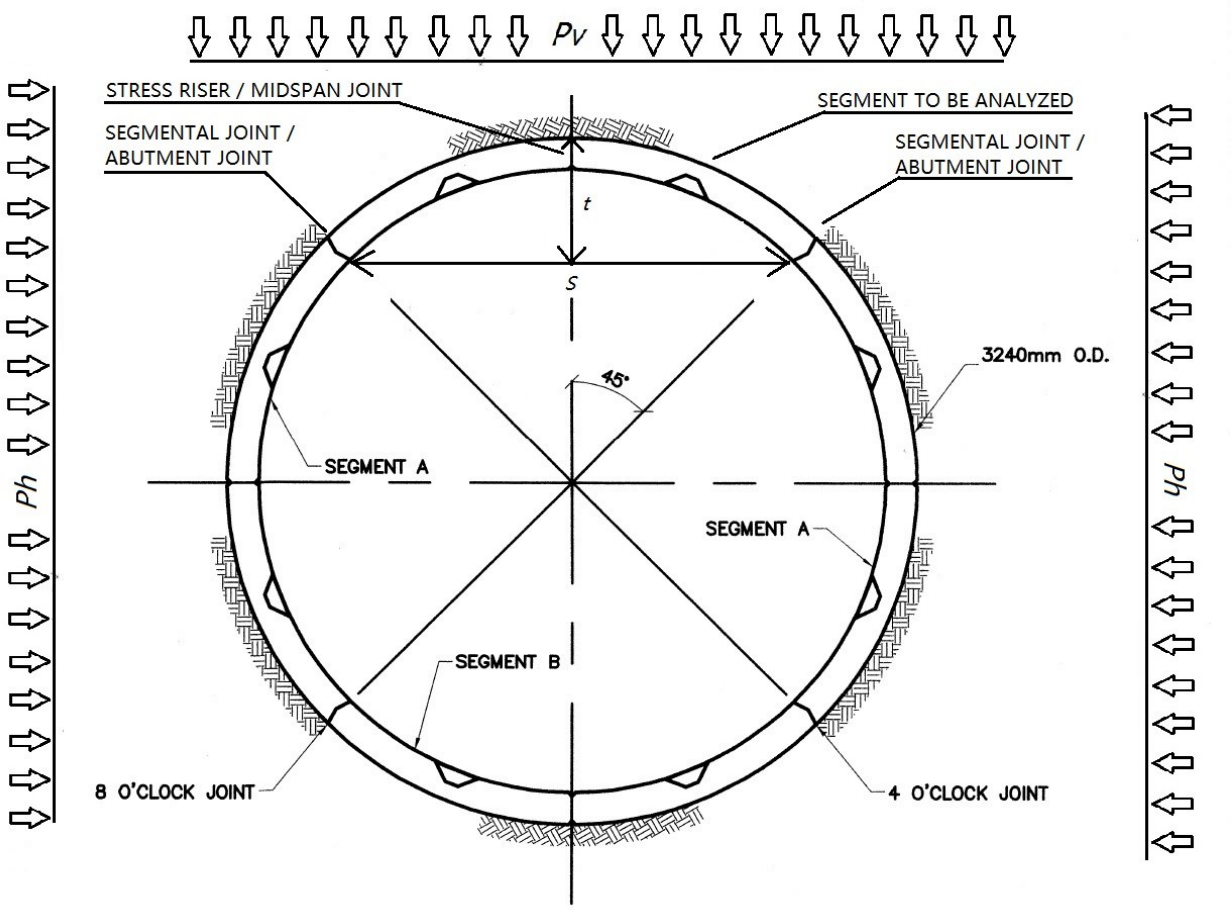

Figure 6-9 Voussoir beam analysis for the segment at crown of tunnel

According to the analysis procedure in in Figure 5-8, the equilibrium state is highlighted in Table 6-5, where *n=0.58*. The midspan displacement at the stress riser is 1.5mm which is larger than the result from analysis using existing close form solution which is 1.07mm. This is may be because the segmental liner was modeled without joint in close form solution, this will be smaller displacement. The maximum compressive stress at midspan is 8.6MPa. The factor of safety of compressive failure is

$$F.S._{\cdot compressive\ failure} = \frac{\sigma_c}{\sigma_{max}} \qquad \text{Equation 6-26}$$

From the analyzed result, the Factor of Safety is,

$$F.S. = 5.3$$ Equation 6-27

If using the limit state design method, the allowable compressive stress is:

$$\alpha \emptyset_c \sigma_c > \sigma_{max}$$ Equation 6-28

Where

α is stress release parameter, 0.85 was selected as per Montgomery and Eisenstein's report. (Montgomery & Eisenstein, 1995);

$\emptyset_c$ is the concrete performance factor, 0.6 was selected as per CSA Standard on Design of Concrete Structures (CSA, 2014).

From the analyzed result, the allowable compressive stress is:

$$20.4\ MPa > 8.6\ MPa$$ Equation 6-29

According to the both criteria, the Factor of Safety and Limit Sate of Design, the stress riser as the crown of tunnel is free from compressive failure, even with the appearance of hair crack.

Table 6-5 Analysis results according to Voussoir Beam Theory

n	Z_0/m	L/m	Δ L/m	Z_{chk}	Z/m	σ_{max}/kPa	ρ_1	ρ_2	σ_{arch} / kPa	ΔL_new / m	$\sigma_{midspan}$ / kPa	Midspan deflection δ / m
0.01	0.396	2.408	0.000	0.188	0.396	698622.07	6.83	3.23	190521.16	0.0153	268700.79	0.0000
0.02	0.393	2.405	0.015	0.170	0.376	367661.88	6.79	3.22	101356.87	0.0081	141408.42	0.0166
0.03	0.389	2.402	0.008	0.174	0.381	242154.28	6.74	3.21	67478.08	0.0054	93136.26	0.0088
0.04	0.386	2.399	0.005	0.174	0.380	181746.91	6.70	3.21	51187.83	0.0041	69902.66	0.0059
0.05	0.383	2.396	0.004	0.172	0.379	146088.51	6.66	3.20	41582.32	0.0033	56187.89	0.0045
0.06	0.380	2.393	0.003	0.170	0.376	122508.87	6.61	3.19	35238.55	0.0028	47118.80	0.0037
0.07	0.377	2.390	0.003	0.168	0.374	105753.80	6.57	3.19	30737.58	0.0024	40674.54	0.0031
0.08	0.373	2.388	0.002	0.165	0.371	93236.50	6.52	3.18	27380.99	0.0022	35860.19	0.0027
0.09	0.370	2.385	0.002	0.163	0.368	83532.59	6.48	3.17	24784.24	0.0020	32127.92	0.0025
0.10	0.367	2.382	0.002	0.160	0.365	75792.35	6.43	3.17	22717.96	0.0018	29150.91	0.0022
0.11	0.364	2.379	0.002	0.157	0.362	69477.31	6.39	3.16	21036.80	0.0017	26722.04	0.0021
0.12	0.361	2.376	0.002	0.155	0.359	64229.54	6.34	3.15	19644.16	0.0016	24703.67	0.0019
0.13	0.358	2.374	0.002	0.152	0.356	59801.86	6.30	3.15	18473.33	0.0015	23000.71	0.0018
0.14	0.354	2.371	0.001	0.149	0.353	56018.04	6.25	3.14	17476.76	0.0014	21545.40	0.0017
0.15	0.351	2.368	0.001	0.147	0.349	52749.06	6.21	3.14	16619.64	0.0013	20288.10	0.0016
0.16	0.348	2.365	0.001	0.144	0.346	49898.27	6.16	3.13	15875.89	0.0013	19191.64	0.0016
0.17	0.345	2.363	0.001	0.142	0.343	47391.87	6.12	3.13	15225.62	0.0012	18227.64	0.0015
0.18	0.342	2.360	0.001	0.139	0.340	45172.49	6.07	3.12	14653.35	0.0012	17374.03	0.0015
0.19	0.338	2.358	0.001	0.136	0.337	43194.91	6.02	3.12	14146.90	0.0011	16613.43	0.0014
0.20	0.335	2.355	0.001	0.134	0.334	41422.96	5.98	3.11	13696.52	0.0011	15931.91	0.0014
0.21	0.332	2.352	0.001	0.131	0.331	39827.42	5.93	3.11	13294.35	0.0010	15318.24	0.0014
0.22	0.329	2.350	0.001	0.129	0.327	38384.38	5.88	3.10	12933.95	0.0010	14763.22	0.0013
0.23	0.326	2.347	0.001	0.126	0.324	37074.09	5.84	3.10	12610.02	0.0010	14259.27	0.0013
0.24	0.322	2.345	0.001	0.124	0.321	35880.15	5.79	3.09	12318.14	0.0010	13800.06	0.0013
0.25	0.319	2.342	0.001	0.121	0.318	34788.76	5.74	3.09	12054.62	0.0009	13380.29	0.0013
0.26	0.316	2.340	0.001	0.119	0.315	33788.28	5.69	3.09	11816.34	0.0009	12995.49	0.0012
0.27	0.313	2.338	0.001	0.117	0.312	32868.78	5.64	3.08	11600.64	0.0009	12641.84	0.0012
0.28	0.310	2.335	0.001	0.114	0.308	32021.78	5.60	3.08	11405.27	0.0009	12316.07	0.0012
0.29	0.306	2.333	0.001	0.112	0.305	31239.97	5.55	3.08	11228.27	0.0009	12015.37	0.0012
0.30	0.303	2.330	0.001	0.110	0.302	30517.04	5.50	3.07	11067.97	0.0009	11737.32	0.0012
0.31	0.300	2.328	0.001	0.107	0.299	29847.49	5.45	3.07	10922.93	0.0008	11479.80	0.0012
0.32	0.297	2.326	0.001	0.105	0.296	29226.51	5.40	3.07	10791.86	0.0008	11240.97	0.0012
0.33	0.294	2.324	0.001	0.103	0.292	28649.91	5.35	3.07	10673.68	0.0008	11019.19	0.0012
0.34	0.290	2.321	0.001	0.101	0.289	28113.97	5.30	3.07	10567.41	0.0008	10813.07	0.0012
0.35	0.287	2.319	0.001	0.098	0.286	27615.44	5.25	3.06	10472.22	0.0008	10621.32	0.0012
0.36	0.284	2.317	0.001	0.096	0.283	27151.41	5.19	3.06	10387.36	0.0008	10442.85	0.0012
0.37	0.281	2.315	0.001	0.094	0.280	26719.32	5.14	3.06	10312.18	0.0008	10276.66	0.0012
0.38	0.278	2.313	0.001	0.092	0.277	26316.88	5.09	3.06	10246.11	0.0008	10121.88	0.0012

n	Z_0/m	L/m	Δ L/m	Z_{chk}	Z/m	σ_{max}/kPa	ρ_1	ρ_2	σ_{arch} / kPa	ΔL_new / m	$\sigma_{midspan}$ / kPa	Midspan deflection δ / m
0.39	0.275	2.311	0.001	0.090	0.273	25942.03	5.04	3.06	10188.63	0.0008	9977.71	0.0012
0.40	0.271	2.308	0.001	0.088	0.270	25592.97	4.98	3.06	10139.31	0.0008	9843.45	0.0012
0.41	0.268	2.306	0.001	0.086	0.267	25268.04	4.93	3.06	10097.75	0.0008	9718.48	0.0012
0.42	0.265	2.304	0.001	0.084	0.264	24965.78	4.87	3.06	10063.62	0.0008	9602.22	0.0012
0.43	0.262	2.302	0.001	0.082	0.261	24684.88	4.82	3.06	10036.60	0.0008	9494.18	0.0012
0.44	0.259	2.300	0.001	0.080	0.257	24424.14	4.76	3.06	10016.46	0.0008	9393.90	0.0012
0.45	0.255	2.298	0.001	0.078	0.254	24182.50	4.71	3.07	10002.96	0.0008	9300.96	0.0013
0.46	0.252	2.296	0.001	0.076	0.251	23959.00	4.65	3.07	9995.91	0.0008	9215.00	0.0013
0.47	0.249	2.294	0.001	0.074	0.248	23752.78	4.60	3.07	9995.16	0.0008	9135.68	0.0013
0.48	0.246	2.293	0.001	0.072	0.244	23563.06	4.54	3.07	10000.57	0.0008	9062.72	0.0013
0.49	0.243	2.291	0.001	0.070	0.241	23389.16	4.48	3.08	10012.05	0.0008	8995.83	0.0013
0.50	0.239	2.289	0.001	0.068	0.238	23230.45	4.42	3.08	10029.51	0.0008	8934.79	0.0013
0.51	0.236	2.287	0.001	0.066	0.235	23086.37	4.36	3.08	10052.90	0.0008	8879.37	0.0014
0.52	0.233	2.285	0.001	0.064	0.232	22956.44	4.30	3.09	10082.19	0.0008	8829.40	0.0014
0.53	0.230	2.283	0.001	0.063	0.228	22840.21	4.24	3.09	10117.37	0.0008	8784.70	0.0014
0.54	0.227	2.282	0.001	0.061	0.225	22737.32	4.18	3.10	10158.47	0.0008	8745.12	0.0014
0.55	0.223	2.280	0.001	0.059	0.222	22647.43	4.12	3.11	10205.51	0.0008	8710.55	0.0014
0.56	0.220	2.278	0.001	0.057	0.219	22570.27	4.05	3.11	10258.56	0.0008	8680.87	0.0015
0.57	0.217	2.277	0.001	0.056	0.216	22505.58	3.99	3.12	10317.70	0.0008	8655.99	0.0015
0.58	0.214	2.275	0.001	0.054	0.212	22453.19	3.92	3.13	10383.05	0.0008	8635.84	0.0015

6.3 Conclusion

As the stress distribution at the stress riser cannot be derived from the existing analytical method (closed-form solution), there is always the uncertainty of compressive failure at stress riser during the application of segment concrete liner. This safety concern will be more outstanding when visible hair cracks happened at the stress risers.

One of the storm tunnels with internal diameter of 2940mm and 14.5 m ground cover was analyzed using both the existing method and voussoir method. The radial displacements at the stress riser derived from both methods are very close. The compressive stress obtained from voussoir beam method demonstrated the stress riser is safe on compressive failure.

This investigation has contributed to the final rehabilitation plan for this section of tunnel shown in Figure 6-5. All the steel ribs and straps had been removed from the tunnel as the tunnel is structurally safe. The “reinforcement” is proved to be not required. The Figure 6-10 shows the tunnel after removed the “reinforcement”.

Figure 6-10 Tunnel after “Reinforcement” Removed

References

CSA, C. G. (2014). A23.3-14 design of concrete structures CSA Group.

Montgomery, J., & Eisenstein, Z. (1995). Soft ground tunnel design in edmonton.

Ranken, R. E., Ghaboussi, J., Hendron, A. J., University of Illinois, United States, & United States. (1978). Analysis of ground-liner interaction for tunnels. Washington: U.S. Dept. of Transportation, Office of the Secretary; Springfield, Va.

7 Conclusion and Future Research

7.1 Research Summary

Voussoir beam theory, also named as arching action, has been widely accepted and applied in design and construction of both surface and underground structure. However, there are discrepancies between the voussoir beam models, for example, the shape and depth of the induced stress at abutment and midspan, the beam shortening equation, and etc.

In this investigation, the behavior of voussoir beam under transverse loading was investigated through both physical and numerical modeling method. Then, an analytical model was built based on a general form of stress distribution at the abutment and midspan with different depths of stress distributions. Based on the results from physical and numerical investigations, an iteration procedure was proposed to determine the stability and deflection of voussoir beam. The voussoir beam model developed has been applied to analyze the mechanical behavior of stress riser, one type of joints of the segmental precast concrete liner used by City of Edmonton. The stress distribution at stress riser was first derived for the liner under short-term loading.

7.1.1 Current Knowledge of Voussoir Beam Theory

The research on voussoir beam theory was reviewed based on the three investigation methods, analytical, experimental and numerical investigation. The discrepancies between the results obtained by different researchers were discussed.

7.1.2 Selection and Characterization the physical modeling material

Concrete and plaster were selected to model the natural hard rock or artificial hard material based on its brittleness, heterogeneity, local availability and capacity requirements on laboratory

facilities. The uniaxial compression test, splitting tensile strength test and sliding friction test were performed to characterize the material. The results obtained were used both in physical investigation and numerical investigations followed.

7.1.3 Physical Investigation

Voussoir beam models with abutments of concrete and plaster were tested under transverse loading. Vic-3D Correlation System, one photogrammetric analysis method, was applied to measure and analyze the displacement and deformation on the voussoir beam surface during transverse loading. It was found that the stress distributions at the midspan and abutment are different both in shape and depth. And the stress distribution is changing as the loading changes as well. These findings are different from the assumptions made in previous analysis. The findings are summarized as following:

1) The stress distribution at the midspan is best fitted by a linear function, and the extent of the distribution is much smaller than it is at the abutment. The depth of the distribution is changing with the loading increase.
2) The stress distribution at the abutment is best fitted by a polynomial function, and the extent of the distribution is more than one half of the beam's thickness. The distribution decreases rapidly with an increasing load.
3) The maximum stress at the abutment is larger than it is at the midspan. The first stress is nearly three times that of the last one.
4) The shear sliding failure at the abutments is likely to happen with the voussoir beams of high strength and low span/thickness ratio. For stable voussoir beams, sliding also happened at the beginning of the test, until it ceased at a certain stage. The load-bearing

ability of the beam kept increasing at this time. This indicates the onset of stable arching after initial shear.

5) Except for the area near the top of the abutment, the whole beam is under axial compression. This means that the thickness of the arch developed is equal to the beam's thickness.

7.1.4 Numerical Investigation

Numerical modeling was used to further the investigation. The Finite Element Code, *Phase*^{2} *8.0*, was selected to numerically model the behavior of voussoir beams under transverse loading due to its capacity for modeling joints, providing multiple material models for rock, and providing flexibility for the staging of loading.

The cohesion-softening friction hardening model was used in the material model. The maximum shear strain was the indication of failure for voussoir beams. The Voronor tessellation was applied to simulate the heterogeneity in voussoir beams. Then the numerical model was calibrated by the uniaxial compression test and direct splitting test. From the calibration test, the numerical model can capture the key characteristics of concrete samples through the uniaxial compression test and direct splitting test. The same numerical model will be applied to model voussoir beams.

The stress distribution and deflection of voussoir beam were compared between the results obtained by physical investigation and numerical investigation. Both of them are very close. The findings from the numerical modeling are as follows:

1) The stress induced at the abutment is nonlinear, and, at the midspan, it is linear;

2) The stress induced at the abutment is approximately three times the stress at the midspan under the same transverse load;
3) The ratio of the depth of stress induced at the abutment to beam thickness (n) is close to 0.3 before crushing. After the crushing occurred, the ratio increased to close to 0.5. The ratio decreased to 0.3 until it fully crushed the beam;
4) The ratio of the depth of stress induced at the midspan to beam thickness (n) is close to 0.4 before crushing the beam. After the crushing occurred, the ratio increased to close to 1 until it fully crushed the beam.

7.1.5 Theoretical Modeling

The analysis was based on a general form of stress distribution at the abutment and midspan with different depths of stress distributions. Under elastic buckling (i.e. no crushing), with the beam being free of any lateral stress, the incompatibilities were resolved by carrying out a more generalized non-linear analytical analysis. With the inputs from physical and numerical investigation results, an iteration procedure was provided based on Diederichs's iteration procedure.

7.1.6 Application of Voussoir Beam Theory on Segment Liner

The stress distribution at the stress riser of segmental precast concrete liner cannot be derived from existing closed form solution. There is always the uncertainty about the compressive failure of the segment liner when hair crack happened at stress risers. To model one piece of segment liner as a voussoir beam, the two longitudinal joint as rigid abutment joints and stress riser as midspan joints, the stress distribution and deflection at stress riser were obtained. It shows the stress riser is free from compressive failure for the target project. This is verified in the field by

after the safely removing of temporary “reinforcing” measures. The deflection at stress riser is close to the results obtained from close form solution.

7.2 Major Contributions

1) The stress distribution along midspan and abutment of voussoir beam was firstly obtained from physical tests with the application of image correlation technique.
2) With calibration and validation to physical testing, voussoir beam behaviour has been investigated systematically using finite element code *Phase*^{2}.
3) An analytical model was derived starting from a general form of stress distribution at midspan and abutment for voussoir beam. Based on the findings from physical and numerical investigations, an iteration procedure was developed to determine the stability of voussoir beams and deflection at the midspan.
4) The voussoir beam theory was applied to determine the mechanical behavior of segmental concrete liner. As far as the author's knowledge, this is the only analytical method that is capable to analyze the interaction between segments of segmental liner to resist ground loading.

7.3 Recommendations for Future Research

5) To evaluate the stability of the voussoir beam under crushing conditions, the same general procedure in analytical modeling can be used. The crushing conditions can be categorized as crushing of the voussoir beam at the ends only, the center only and at both the ends and center.
6) To determine whether or not the stress intensity factors are in such a critical combination as to induce additional crack growth and propagation, the linear elastic fracture mechanics (L.E.F.M.) can be applied.
7) To systematically investigate the impact of constraining force on the behavior voussoir beams.
8) To apply voussoir beam theory on the failure of bedded footwall slopes.